

# The Effects of Grain Boundary Character and Energy on Complexion Transitions in Ceramics

Submitted in partial fulfillment of the requirements for the degree of  
Doctor of Philosophy  
in  
Materials Science and Engineering

Stephanie A. Bojarski

B.S. Materials Science and Engineering, Lehigh University  
M.S. Materials Science and Engineering, Carnegie Mellon University

Carnegie Mellon University  
Pittsburgh, PA  
May, 2014

## Acknowledgements

I would like to start off by thanking my advisor, Dr. Gregory Rohrer, for his support and guidance throughout the course of my graduate research. In particular, I would like to thank Dr. Rohrer for all of the research-based opportunities that he has given me, and for the diligent work and patience that he has put forth into editing my various documents and publications. Along the same lines, I would like to thank my thesis committee members, Drs. Martin Harmer, Anthony Rollett, and Elizabeth Holm, for their support throughout my graduate career, whether it be helping me properly analyze data, offering a research group for collaborations, or suggesting a new way of thinking about my results – I wholeheartedly appreciate your support and feedback.

A successful research project is never completed alone, and with that I must acknowledge my collaborators. I would like to show particular appreciation to the Harmer group at Lehigh University, for providing me with research projects, helping me make samples, and conducting TEM analysis on my experiments. Researchers that deserve special recognition include: Dr. Shuailei Ma, Abigail Lawrence, Michael Krackum, Dr. Zhiyang Yu, Qian (Ken) Wu, and Animesh Kindu. I would also like to thank Dr. Michael Stuer formally of the École polytechnique fédérale de Lausanne (EPFL, Lausanne, Switzerland). Additionally, I would like to acknowledge Dr. Wayne Kaplan and his research group at the Technion (Haifa, Israel) for being so hospitable during my stay in Israel – with a special acknowledgement for Hadas Sternlicht for working tirelessly using STEM to conduct chemical analysis of my grain boundaries. I would also like to thank Dr. Dominique Chatan and Dr. Paul Wynblatt for the insightful conversations and support that they have given me throughout my time at CMU.

I would like to express my gratefulness to my colleagues and friends at Carnegie Mellon University, without whom I would have surely gone insane. First off, Jason Wolf, Tom Nuhfer, and Adam Wise deserve a special thank you for their endless support, advice, pep talks, and help with characterizing my experiments and troubleshooting lab equipment. I would also like to acknowledge Jeanna Pekarcik, Susan Smith, Neetha Kahn, Marygrace Antkowsky, and all of the CMU staff for being there to help with both administrative purposes and for their support, advice, and friendship. My department collaborators, colleagues, and undergraduate researchers

who have helped me with various aspects of my research, including: Madeleine Kelly, William Frazer, Brian Lin, Dr. Sean Donnegan, Dr. Jingxi Wu, Dr. Sutatch Ratanaphan, Dr. Andrew Schultz, Dr. Yiling Zhang, Ratiporn Munprom, André Assis, William Lenthe, and Jocelyn Knighting.

Finally, I need to acknowledge my family and friends. I would like to especially thank my fiancée Benjamin Eyer for his love, support, chemistry advice, and ability to talk me down from almost any situation. Along the same lines, my parents Paul and Patty Bojarski need recognition for being excellent role models who have been there for me throughout the highs and lows of research. Finally, I want to thank my friends from CMU, particularly Erica Sampson, Aditya Balasubramanian, Ellen Reifler, Clare Mahoney, Rachel Ferebee, Clayton Stein, June Bott, Carolyn Norwood, and many others, for their friendship and support.

Most importantly, I must gratefully acknowledge my funding agencies, without which none of the research in this document would be possible. These include Navy-ONR-MURI grant number N00014-11-1-0678, NSF-MRSEC grant number DMR-0520425, Sandia National Laboratories Excellence in Engineering Research graduate fellowship under grant number 1263802, and the Clare and John Bertucci fellowship for Ph.D. candidates in the Carnegie Institute of Technology.

Stephanie A. Bojarski

May, 2014

## Abstract

A grain boundary complexion is a distinct equilibrium structure and composition of a grain boundary. A complexion transformation is then a transition from a metastable to an equilibrium complexion at a specific temperature, pressure, chemical potential, and grain boundary character. Previous work indicates that, in the case of doped alumina, a complexion transition that increased the mobility of transformed boundaries and resulted in abnormal grain growth also caused a decrease in the mean relative grain boundary energy as well as an increase in the anisotropy of the grain boundary character distribution (GBCD). The current work will investigate the hypothesis that the rates of complexion transitions that result in abnormal grain growth (AGG) depend on grain boundary character and energy. Furthermore, the current work expands upon this understanding and tests the hypothesis that it is possible to control when and where a complexion transition occurs by controlling the local grain boundary energy distribution.

The first experiment expands upon the previous results and investigates the mesoscale grain boundary character and energy distributions before and after the initiation of AGG in Ca-doped yttria. The GBCD of samples exhibiting normal grain growth favored  $\{111\}$  planes while those exhibiting AGG favored  $\{001\}$  planes. Additionally, the relative grain boundary to surface energy ratios around and adjacent to abnormally large grains were 33% lower than boundaries around normally sized grains far from the large grains and in the sample without AGG.

The effect of Y and La doping on the grain morphology and grain boundary character distributions of alumina are then analyzed. Grain boundary character distributions were determined for spark plasma sintered Y and La-doped aluminas prepared at temperatures between 1450 °C and 1600 °C. La-doping leads to grain boundaries that adopt (0001) orientations at all observed temperatures, while the Y-doped microstructures are more equiaxed. At 1500 °C, some of the boundaries in the Y-doped samples transform to a higher mobility complexion resulting in AGG. In this microstructure, the  $\{01\bar{1}2\}$  grain boundary plane is more likely to occur. However, after the fast growing grains impinge, the dominant plane is  $\{11\bar{2}0\}$ . The grain boundary planes in the Y and La-co-doped samples preferred (0001) and  $\{01\bar{1}2\}$  orientations, combining the characteristics of the singly doped samples. Grain boundaries with a 60° misorientation about [0001] were up to six times more common than random in the Y-doped samples.

By combining the findings from the first two experiments we then aim to control the occurrence of complexion transitions by controlling the character and thus the energy of specific interfaces in the Y-doped alumina system. Single crystal sapphire substrates with (0001) and (11 $\bar{2}$ 0) orientations were embedded in Y-doped alumina powder and spark plasma sintered to form a dense, pre-transformed sample. This sample was then heated to 1500°C for 8 hours, where abnormal grain growth occurred. The mean relative grain boundary energies of the pre-transformed interfaces between the single crystals and the powder were 1.15 for the (0001) oriented crystal and 0.55 for the (11 $\bar{2}$ 0) oriented crystal. After the transition occurred, the average energy of the (0001) interface decreased by 19% to 0.93 and the average energy of the (11 $\bar{2}$ 0) interface decreased by 27% to 0.40. More abnormal grains grew along the higher energy (0001) interface than the lower energy (11 $\bar{2}$ 0) interface.

The temperature and grain boundary energy dependence of the rate of the complexion transition in Y-doped alumina was further investigated. In this experiment the samples with embedded (0001) and (11 $\bar{2}$ 0) planes were heated for various times and at temperatures. The extent of the complexion transformation was tracked over time to determine if a single critical nucleation temperature or a range of critical nucleation temperatures were needed to overcome the nucleation barrier for a grain boundary complexion transition. It was found that the number of metastable boundaries was dependent on temperature. At most annealing temperatures and times, the higher energy (0001) interface exhibited more abnormal grains along the interface than the (11 $\bar{2}$ 0) interface. The rate of a complexion nucleation along each interface was greater for the higher energy (0001) interface at 1500 °C (0.69%/μm-hr) compared to the lower energy (11 $\bar{2}$ 0) interfaces (0.16%/μm-hr). At 1600 °C the nucleation rate was approximately the same (0.3%/μm-hr) however the higher energy (0001) interface exhibited a much higher initial percent of the interface that was transformed.

Finally, the relative energies of grain boundaries in Y-doped alumina were analyzed as a function of doping concentration and temperature. 100 and 500 ppm Y-doped alumina samples were thermally grooved at 50 °C increments between 1350 °C and 1650 °C. In the 100 ppm sample, it was found that the mean relative grain boundary energy increased with increasing temperature until 1500 °C, at which point the mean energy decreased by 20%. This decrease in energy also corresponds to the presence of high mobility grain boundaries, indicating the occurrence of a complexion transition along some of the grain boundaries. The energy

continued to increase with increasing temperature after 1550°C. In the 500 ppm sample, a maximum energy was reached as a second phase precipitated at 1450 °C. Between 1450 and 1550 °C the energy decreased by 25%. The energy increases after 1550 °C. These results show that the grain boundary energy increases with the precipitation of a second phase and decreases with the occurrence of a complexion transition. It also indicated that the increase in grain boundary energy associated with solute desorption with temperature could aid in overcoming the nucleation barrier for a grain boundary complexion transition in the Y-doped alumina system.

The culmination of the results presented in this document indicates that there is a decrease in boundary energy when a metastable to equilibrium complexion transition occurs resulting in AGG. This causes an increase in the relative area of low energy boundaries, typically leading to an increase in the width of the grain boundary character distribution. By controlling the processing temperature and energy of interfaces in a system that displays a grain boundary complexion transition, it is possible to control the rate of which a grain boundary complexion transformation occurs.

# Table of Contents

<b>Acknowledgements .....</b>	<b>ii</b>
<b>Abstract.....</b>	<b>iv</b>
<b>Table of Contents .....</b>	<b>vii</b>
<b>List of Figures.....</b>	<b>x</b>
<b>List of Tables .....</b>	<b>xvi</b>
<b>List of Symbols and Abbreviations .....</b>	<b>xvii</b>
<b>1. Introduction.....</b>	<b>1</b>
<b>1.1 Motivation .....</b>	<b>1</b>
<b>1.2 Hypothesis .....</b>	<b>2</b>
<b>1.3 Objectives .....</b>	<b>4</b>
<b>2. Background .....</b>	<b>5</b>
<b>2.1 Complexions .....</b>	<b>5</b>
2.1.1. Classification .....	5
2.1.2. Characterization.....	9
2.1.3 Grain Boundary Properties .....	11
2.1.4 Grain Boundary Complexion Diagrams.....	12
2.1.5 Mechanisms for abnormal grain growth .....	14
<b>2.2 Interfacial and Grain Boundary Energy .....</b>	<b>16</b>
2.2.1 Wulff shape .....	17
2.2.3 Historical Derivation .....	19
2.2.4 Experimentally Determining Relative Grain Boundary Energy .....	20
2.2.5 Temperature dependence of grain boundary energy in impure systems .....	21
<b>2.3 Grain Boundary Characteristics .....</b>	<b>22</b>
2.3.1 Misorientation .....	22
2.3.2 Representations of the grain boundary character distribution .....	24
<b>2.4 Texture analysis .....</b>	<b>30</b>
2.4.1 Pole Figures .....	31
2.4.2 Inverse Pole Figures .....	31
2.4.3 Inverse Pole Figure Maps.....	31
<b>2.5 Materials Overview .....</b>	<b>31</b>

2.5.1 Yttria Structure .....	31
2.5.2 Alumina Structure .....	33
<b>3. Methodology .....</b>	<b>36</b>
<b>3.1 Characterization Methods .....</b>	<b>36</b>
3.1.1 Electron Backscatter Diffraction .....	36
3.1.2 Atomic Force Microscopy .....	37
<b>3.2 Powder Processing .....</b>	<b>38</b>
<b>3.3 Forming Processes .....</b>	<b>40</b>
3.3.1 Hot Press .....	41
3.3.2 Spark Plasma Sintering <sup>67-69</sup> .....	41
<b>3.4 Sample Preparation .....</b>	<b>42</b>
<b>3.5 Heat Treatments .....</b>	<b>43</b>
3.5.1 Annealing .....	43
3.5.2 Thermal Grooving .....	43
<b>3.5 Grain Boundary Character Measurements .....</b>	<b>44</b>
3.5.1 EBSD Parameters .....	45
3.5.2 Analysis Parameters .....	45
<b>3.6 Grain Boundary Energy Measurements .....</b>	<b>46</b>
3.6.1 AFM Parameters .....	46
3.6.3 Groove measurements and Energy Calculations .....	46
<b>4. Experiment I: Changes in grain boundary character and energy distributions resulting from a complexion transition in Ca-doped Yttria .....</b>	<b>48</b>
4.1 Motivation and Overview .....	48
4.2 Experimental Procedures .....	49
4.3. Results .....	53
4.4 Discussion .....	59
4.4.1 Grain Boundary Character .....	59
4.4.2 Grain Boundary Energy .....	61
4.4.3 Texture analysis .....	63
4.5 Conclusions .....	63
<b>5. Experiment II: Influence of Y and La Additions on Grain Growth and the Grain Boundary Character Distribution of Alumina .....</b>	<b>65</b>
5.1 Introduction .....	65
5.2 Experimental Procedure .....	68
5.2.1 Sample preparation .....	68
5.4 Discussion .....	78
5.5 Conclusions .....	85

<b>6. Experiment III: Experimental test of the effect of grain boundary energy on the nucleation of complexion transitions.....</b>	<b>87</b>
<b>6.1 Introduction.....</b>	<b>87</b>
<b>6.2 Experimental Procedures.....</b>	<b>89</b>
<b>6.3 Results.....</b>	<b>90</b>
<b>6.4 Discussion.....</b>	<b>93</b>
<b>6.5 Conclusions.....</b>	<b>97</b>
<b>7. Experiment IV: Investigating the Kinetics of Grain Boundary Complexion Transitions.....</b>	<b>99</b>
<b>7.1 Background.....</b>	<b>100</b>
<b>7.2 Methodology.....</b>	<b>103</b>
<b>7.3 Results.....</b>	<b>108</b>
<b>7.5 Conclusions.....</b>	<b>122</b>
<b>8. Experiment V: Temperature dependence of relative grain boundary energy in Y-doped alumina.....</b>	<b>123</b>
<b>8.1 Background.....</b>	<b>123</b>
<b>8.2 Methodology.....</b>	<b>126</b>
<b>8.3 Results.....</b>	<b>129</b>
8.3.1 100 ppm Y-doped alumina.....	129
8.3.2 500 ppm Y-doped alumina.....	132
<b>8.4 Discussion.....</b>	<b>134</b>
8.4.1 Why is the slope positive?.....	134
8.4.2 Why does the GBE decrease after increasing?.....	136
8.4.3 100 ppm Y-doped alumina.....	137
8.4.4 500 ppm Y-doped alumina – Energy and Y excess.....	140
8.4.5 Second phase precipitation.....	143
<b>8.5 Conclusions.....</b>	<b>146</b>
<b>9. Summary of Conclusions.....</b>	<b>148</b>
<b>10. References:.....</b>	<b>152</b>

## List of Figures

<b>Figure 2.1.</b> Summary schematics of various categories of complexions (a), and means of transitioning between two different complexion types (b). This figure was reproduced from reference <sup>7</sup> . .....	<b>9</b>
<b>Figure 2.2:</b> Reproduced from Reference <sup>7</sup> . Experimental complexion diagram for $Y_2O_3-Al_2O_3$ showing regions in which a low temperature complexion with low grain boundary mobility (blue) and a high temperature complexion with high mobility (red) are stable. Normal grain growth occurs in both regions. There is a region of overlap where it is believed that both complexions may coexist (purple). It is believed that abnormal grain growth occurs in this region because the high T complexion has a significantly larger grain boundary mobility than the low T complexion. ....	<b>13</b>
<b>Figure 2.3.</b> Simplified example of a $\gamma$ -plot where the X and Y-axis represent crystallographic directions and the surface energy is a function of $\theta$ , which determines a point in the crystallographic space (a). The Wulff shape is the inner cusp of lines drawn perpendicular to the $\gamma$ vectors (b). Image reproduced from reference <sup>31</sup> . ....	<b>18</b>
<b>Figure 2.4.</b> Examples of grain boundary thermal groove line profiles, where: the interfacial energy and torque terms are labeled in (a). The parameters for the Mullins' analysis of the complete dihedral angle (b), and modified Mullins analysis using the half angle (c). ....	<b>19</b>
<b>Figure 2.5.</b> Bunge Euler angles showing $\phi_1$ rotation around the crystallographic [001] axis, which is parallel to the reference frame Z-axis (a), $\Phi$ rotation about the crystallographic [100] axis (b), and a $\phi_2$ rotation about the crystallographic [001] axis. The black arrows show the sample/laboratory reference axis, while the red arrows represent the before (solid line) and after rotation (dashed) crystallographic axis. ....	<b>23</b>
<b>Figure 2.6.</b> One-parameter misorientation angle distribution for a Y+La-doped alumina showing the normal distribution as calculated from random number generation in red and an .....	<b>25</b>
experimentally measured grain boundary line length weighted misorientation angle distribution exhibiting a higher than average populations of $60^\circ$ misorientation angles. ....	<b>26</b>
<b>Figure 2.7.</b> A two dimensional section of three-parameter Rodrigues-Frank space where $R_3=0.32$ and $R_1, R_2$ span the entire fundamental zone of alumina. The arrow indicates the area of Rodrigues-Frank space where the highest population of grain boundary misorientations occurs in the $R_3=0.320$ section– this corresponds to a $51.3^\circ/[001]$ misorientation (a). A two dimensional section of the three-parameter misorientation distribution in axis-angle pair format showing a large number of boundaries at $60^\circ/[0001]$ misorientation (b). ....	<b>27</b>
<b>Figure 2.8.</b> Progression of the two parameter grain boundary character distribution where we see one grain boundary and the corresponding 32 crystal symmetry (noted) for the alumina system, and how it is clear that this boundary is near an (0001) plane (a), 88 grain boundary line segments showing a clear trend to facet near (0001) planes (b), and 370,046 boundaries showing that most of the grain boundaries are faceted on or near the (0001) plane (c). ....	<b>29</b>
<b>Figure 2.9.</b> Distribution of grain boundary planes at a $60^\circ/[111]$ misorientation ( $\Sigma 3$ ) for nickel. The results show a very strong preference for the (111) coherent twin boundary. ....	<b>30</b>

<b>Figure 2.10.</b> The yttria unit cell replicated from reference <sup>45</sup> (a) and a cubic [001] stereographic projection showing possible low index poles (b). The highlighted region represents the fundamental zone in both GBCD and TSL output.....	<b>32</b>
<b>Figure 2.11.</b> The alumina unit cell in a hexagonal reference frame (a) and the alumina (001) stereographic projection showing low index planes in Miller-Bravais notation (b) In the stereogram, the GBCD fundamental zone is highlighted in blue and the TSL fundamental zone is highlighted in red – they are symmetrically equivalent.....	<b>35</b>
<b>3. Methodology</b> .....	<b>36</b>
<b>Figure 3.1.</b> Schematic of the SPS graphite die holding the C/A-plane alumina sample, showing the current flowing from the moving ram/ positive electrode through the graphite die and to the stationary ram/negative electrode. ....	<b>40</b>
<b>Figure 3.2.</b> Full dihedral angle cumulative distribution of thermal groove temperature sensitivity measurements for grooves at 1400 °C (blue) and 1350 °C (red).....	<b>44</b>
<b>Figure 4.1.</b> (a) Topographic AFM image of the thermally grooved AGG sample, where the solid line indicates the location from which the topographic data in (b) was extracted across a boundary surrounding an abnormal grain and the dashed line indicates the source of the data from the adjacent boundary that between normal grains. (b) The corresponding grain boundary topographs, the height of the boundary is on vertical-axis and width on horizontal-axis. The solid line corresponds to the solid line across the abnormal boundary scan line in (a). Similarly, the dashed line corresponds to the topographic data across a boundary between two smaller grains. ....	<b>52</b>
<b>Figure 4.2.</b> Cumulative distribution of a portion of dihedral angles for AGG and adjacent NGG boundaries, solid shapes are angles calculated using the automated method while the empty shapes are calculated by manually recording the width and depth of each groove. There is no distinguishable difference between the methods, verifying the accuracy of the automated process. ....	<b>53</b>
<b>Figure 4.3.</b> Inverse pole figure maps from EBSD data with superimposed reconstructed grain boundaries for (a) NGG sample, which exhibits a homogeneous grain size distribution, and (b) AGG sample, displaying a bimodal grain size distribution and an apparent change in texture. ..	<b>54</b>
<b>Figure 4.4.</b> Inverse pole figures for the [001] sample reference direction. (a) The NGG sample lacks significant texture. (b) The AGG sample shows a preference for {111} orientations. ....	<b>54</b>
<b>Figure 4.5.</b> The grain boundary plane distributions, independent of misorientation, for the (a) NGG sample and (b) the AGG sample plotted in the standard stereographic triangle.....	<b>55</b>
<b>Figure 4.6.</b> Grain boundary plane distributions for the misorientation of 45 ° around [100], plotted in stereographic projection, with the [100] direction orientated horizontally to the right and the [001] direction is normal to the figure. Subsequent figures are plotted in the same way. (a) NGG sample. (b) AGG sample. ....	<b>56</b>
<b>Figure 4.7.</b> Grain boundary plane distributions for the misorientation of 30 ° around [110]. (a) NGG sample. (b) AGG sample. ....	<b>56</b>
<b>Figure 4.8.</b> Grain boundary plane distributions for the misorientation of 60 ° around [111]. (a) NGG sample. (b) AGG sample. ....	<b>57</b>

<b>Figure 4.9.</b> Topographic AFM images of the (a) NGG sample, (b) AGG sample far from abnormal grains, and (c) AGG sample with a section of a very large grain in the lower part of the field of view. ....	<b>58</b>
<b>Figure 4.10.</b> Cumulative distribution function comparing relative grain boundary energies for boundaries surrounding abnormally large grains (triangle), boundaries surrounding smaller grains that are adjacent to large grains in the AGG sample (square), boundaries surrounding smaller grains far from the large grains in the AGG sample (circle), and mean boundary energy for all boundaries in NGG sample (star). ....	<b>59</b>
<b>Figure 5.1.</b> Effect of pseudo-symmetry on grain boundary distributions in La-doped alumina sintered at 1500°C. Reconstructed line segments before clean up where red/blue/green lines show pseudo-symmetry orientations (a), the corresponding one-dimensional misorientation distribution where the red bars are binned by grain boundary line count, the blue bars represent line length weighted distributions, and the black line represents a simulated random distribution (b) and grain boundary plane distribution in the crystal reference frame (c). Post clean-up line segment reconstruction showing removed pseudo-symmetry (d), the corresponding misorientation distribution (e), and plane distributions (f). ....	<b>71</b>
<b>Figure 5.2.</b> Orientation maps of 450 ppm La-doped alumina (a) SPS temperature 1500 °C and (b) SPS temperature of 1600 °C. Images from before pseudo-symmetry clean up. ....	<b>73</b>
Figure 5.3. Orientation maps of 450 ppm Y-doped alumina with an SPS temperature of (a) 1450 °C, (b) 1500 °C, and (c) 1600 °C. The scale bar for (a) is 25 μm while in (b) and (c) the scale bars are 50 μm. Images from before pseudo-symmetry clean up. ....	<b>73</b>
<b>Figure 5.4.</b> Orientation maps of 450 ppm Y and La co-doped alumina at (a) 1500 °C and (b) 1600 °C. Images from before pseudo-symmetry clean up. ....	<b>74</b>
<b>Figure 5.5.</b> Grain boundary plane distributions, independent of misorientation, plotted in stereographic projection with the (2110) plane orientated horizontally to the right and the (0001) plane normal to the figure. Subsequent figures are plotted the same way. La-doped alumina sintered at (a) 1500 °C, and (b) 1600 °C. ....	<b>74</b>
<b>Figure 5.6.</b> The distribution of grain boundary planes, independent of misorientation, in Y-doped alumina after heating at (a) 1450 °C, (b) 1500 °C, and (c) 1600 °C. ....	<b>75</b>
<b>Figure 5.7.</b> Distribution of grain boundary planes, independent of misorientation, for Y+La co-doped samples sintered at (a) 1500 °C and (b) 1600 °C. ....	<b>76</b>
<b>Figure 5.8.</b> Misorientation distributions and corresponding reconstructed grain boundary line segments for Y-doped alumina sintered at 1450°C (a), 1500°C (b), and 1600°C – exhibiting a large increase in 60° boundaries (c). Based on the configuration of the 60 ° boundaries, it is concluded that they do not result from incorrect indexing because of pseudo-symmetry. Misorientation angle distribution bin sizes are 1° and range from 0 to 104 °. ....	<b>77</b>
<b>Figure 5.9.</b> The grain boundary plane distribution in Y-doped alumina sintered at 1500°C at a 60°/[0001] misorientation (a) and in La-doped alumina sintered at 1500°C at a 60°/[0001] (b). <b>78</b>	
<b>Figure 5.10.</b> Grain boundary plane distributions for La-doped alumina sintered at 1600°C. (a) $\Sigma_7^aG$ (85.9°/[0221]), (b) $\Sigma_7^2V$ (85.9°/[2461]), (c) $\Sigma_{31}^bG$ (63.15°/[1123]). ....	<b>83</b>

**Figure 5.11.** The grain boundary plane distribution for boundaries with a misorientation of  $144.2^\circ/[1\bar{2}10]$  (near  $\Sigma_{11}$ ) of Y-doped alumina, showing  $(\bar{1}0\bar{1}\bar{1})$ ,  $(0001)$ , and  $(10\bar{1}0)$  planes oriented along the tilt zone (a). The misorientation axis and tilt zone are defined by black circle and dotted line, respectively. The grain boundary plane distribution for boundaries with a misorientation of  $95.2^\circ/[01\bar{1}0]$  ( $\Sigma_{11b}$ ) of La-doped alumina showing a symmetric boundary with high populations at  $(0001)$  and  $(\bar{2}110)$  planes – both of which are oriented along the  $[01\bar{1}0]$  tilt axis (b). ..... 84

**Figure 5.12.** Distribution of grain boundary planes for the misorientation of  $38.2^\circ/[0001]$  ( $\Sigma_7$ ) for (a) Y-doped alumina and (b) La-doped alumina. .... 85

**Figure 6.1.** Inverse Pole Figure +Image Quality Maps looking down the  $[010]$  direction for Y-doped alumina as SPS  $(1\bar{1}\bar{2}0)$ - plane (a) and  $(0001)$ -plane (b), and sintered at  $1500^\circ\text{C}$  for 8 hours  $(1\bar{1}\bar{2}0)$ -plane (c) and  $(0001)$ -plane (d). The square in (d) indicates the faceting that occurs along the  $(0001)$  interface. The lengths of the scale bars are (a) 5 mm, (b) 5 mm, (c) 50 mm, and (d) 45 mm. .... 91

**Figure 6.2** Representative AFM images of the partially transformed  $(1\bar{1}\bar{2}0)$  interface (a), almost completely transformed  $(0001)$  plane (b), and example boundary line profiles from each scan (c). The red line profile corresponds to the red line in (a), and the blue corresponds to the blue line in (b). The lengths of scale bars in (a) and (b) are  $3\ \mu\text{m}$  ..... 92

**Figure 6.3.** Cumulative distributions of relative grain boundary energy for (a) the sample that was thermally grooved immediately after SPS, and (b) the sample annealed for 8-hours at  $1500^\circ\text{C}$  inducing AGG. (c) A-plane before (blue) and after (red) the 8 hour anneal and (d) the C-plane before (blue) and after (red) the 8 hour anneal..... 93

**Figure 6.4.** Grain boundary energy schematic showing the difference in initial interfacial energy of the C/ $(0001)$  and A/ planes ( $d_p$ ) exhibiting complexion A, and the corresponding activation energies ( $\Delta E_C$  and  $\Delta E_A$  respectively) needed to nucleate the equilibrium complexion B. .... 94

**Figure 7.1.** Schematic of time temperature transformation diagram where the lower portion of the graph represents transformation kinetics upon cooling, and the top portion represents transformation kinetics upon heating, adapted from reference (<sup>103</sup>). ..... 101

**Figure 7.2.** Representative orientation maps from EBSD data for a unimodal microstructure ( $1500 - 0$  hr) a bimodal microstructure ( $1600 - 0$  hr), and a microstructure displaying significant abnormal grain growth ( $1500 - 2$  hr). Each of the following rows represents a cutoff parameter that is multiplied by the average grain size of the microstructure (G). Scale bars are  $10\ \mu\text{m}$  ( $1500 - 0$  hr),  $15\ \mu\text{m}$  ( $1600 - 0$  hr), and  $50\ \mu\text{m}$  ( $1500 - 2$  hr). ..... 106

**Figure 7.3.** Method of quantifying abnormal grain growth using an EBSD image along a single crystal interface (a). First, a partition is set to filter out grains that are greater than 2.7 times the normal grain size (b). The first partition is removed, and a second is set such that all grains that are greater than 3 times the normal grain size are shown (c). Finally, the total length of the single crystal interface and the length of the single crystal interface that is in contact with abnormal grains were measured..... 108

**Figure 7.4.** EBSD images showing the crystal orientation perpendicular to the single crystal interface ( $[010]$  sample direction) for the samples heated at  $1500^\circ\text{C}$  for 2 hours (a),  $1600^\circ\text{C}$  for 0 hours (b), and  $1600^\circ\text{C}$  for 4 hours (c). The red single crystal represents the  $(0001)$  interface

and the blue/green single crystal represents the  $(1\bar{1}\bar{2}0)$  interface. In each set, the pair of interfaces to the left is the complete, un-partitioned EBSD image and the pair of interfaces to the right is the EBSD map that is partitioned such that grains only three times the average grain diameter are shown. .... 109

**Figure 7.5.** The grain size as a function of time for the samples annealed at 1500 °C (a) and samples annealed at 1600 °C (b). The red squares represent the average abnormal grain size, the blue diamonds represent the average normal grain size, the purple triangles represent the average total grain size, and the dashed green line represents the cutoff parameter that stipulated an abnormal grain. .... 110

**Figure 7.6.** The average normalized grain area versus log of grain diameter for samples sintered at 1500 °C for 0 hours (a), 2 hours (b), 4 hours (c), and 8 hours (d), 1450 °C for 15 hours (e) and at 1600 °C for 0 hours (f), 0.5 hours (g), 2 hours (h), 4 hours (i), and 8 hours (j). The graphs were normalized such that the total area under each plot is one. .... 112

**Figure 7.7.** The percent of the  $(0001)$ /C-plane (red) and  $(1\bar{1}\bar{2}0)$ /A-plane (blue) single crystal interfaces that are in contact with abnormal grains 3 times the average normal grain size. Each group of bars is a single anneal time and temperature combination. The numbers above the bars indicate the percent difference of the percent of the C-plane transformed to the percent of the A-plane transformed. .... 114

**Figure 7.8.** The percent of the C/ $(0001)$  plane single crystal interface that is adjacent to an abnormal grain when sintered at 1500 °C (blue diamond), A/ $(1\bar{1}\bar{2}0)$  plane when sintered at 1500 °C (red square), C-plane when sintered at 1600 °C (green triangle), and A-plane sintered at 1600 °C (purple circle). Graph (a) represents the directly measured percent transformed against time while graph (b) represents the percent transformed normalized by the average abnormal grain size at the given time and temperature against time. .... 116

**Figure 7.9.** Representative grain boundary energy distribution showing a normal (solid black line), high (dashed red line), and low (unevenly dashed blue line) energy distributions (a) which correspond to the degree of transformation curve in the TTT diagram (b). Where the number of boundaries that are metastable and thus able to transform at a given temperature are dependent on the grain boundary energy needed at the given temperature to overcome the nucleation barrier for a complexion transformation and the rate of the transformation is dependent on the grain boundary energy anisotropy. .... 120

**Figure 7.10.** Orientation maps down the  $[010]$  sample direction of the A-plane (a) and C-plane (b) interfaces of the sample used to test the effect of the electric field on the grain morphology. .... 122

**Figure 8.1.** Representative topographic AFM images for Y-doped alumina (a) and corresponding thermal groove profile (b) where the groove half width (w), height (d), groove angle ( $\beta$ ) and surface dihedral angle ( $\Psi$ ) are labeled and correspond to equation 1 below. .... 128

**Figure 8.2.** AFM tip convolution as a function of thermal groove widths at different groove angles ( $\beta$ ). Small widths have a significant tip-induced error, while larger widths exhibit realistic  $\beta$  measurements. Reproduced from Reference (<sup>37</sup>). .... 129

**Figure 8.3.** Representative AFM topographs from each grooving temperature increment in the 100 ppm Y-doped alumina that was thermally grooved at: 1350 °C (a), 1400 °C (b), 1450 °C (c),

1500 °C (d), 1525 °C (e), 1550 °C (f), 1600 °C (g), 1650 °C (h). Where the yellow arrow indicates the presence of an abnormally large grain with ghost boundaries. The scale bar in all cases is 5  $\mu\text{m}$ . ..... 130

**Figure 8.4.** Cumulative distribution of relative grain boundary energies for the 100 ppm samples grooved at 1350 °C (purple diamond), 1450 °C (green square), 1550 °C (red circle), and 1650 °C (blue square). ..... 131

**Figure 8.5.** The relative grain boundary energy as a function of temperature for the 100 ppm Y-doped alumina sample can be seen in (a). The original measurements are in blue (diamond), the corrected measurements are in red (square), and the decreasing temperature measurements are in green (triangle). (b) Shows the groove width as a function of temperature for the increasing temperature experiment in blue (diamond) and the decreasing experiment red (square). ..... 132

**Figure 8.6.** Representative topographic AFM images of 500 ppm Y-doped alumina grooved at: 1350 °C (a), 1400 °C – showing exaggerated grooving (b), 1450 °C – showing exaggerated grooving (c) and second phase precipitation (d), 1500 °C – showing ghost boundaries and the arrows indicate a wetting second phase (e), 1550 °C – where the arrows show small second phase particles (f), 1600 °C (g), and 1650 °C (h). In these images, the yellow arrows indicate different second phase morphologies including wetting along the boundaries and smoothly curved particles. All scale bars are 5  $\mu\text{m}$ . ..... 133

**Figure 8.7.** (a) The relative grain boundary energy as a function of temperature for the 500 ppm Y-doped alumina sample where the blue (diamond) represents the original data and the red (square) represents the groove width corrected data. (b) Shows the average grain boundary groove width as a function of temperature. ..... 134

**Figure 8.8.** Approximate amount of Yttrium needed to sustain a certain grain boundary coverage at a given grain size, assuming vanishing bulk solubility. ..... 141

**Figure 8.9.** Representative topographic AFM image for the 500 ppm Y-doped alumina sample sintered at 1450 °C for five hours. In this image we see an area of exaggerated thermal grooving (right) and an area of second phase precipitation (left) around which the grains are not as rounded. ..... 145

**Figure 8.10.** (a) EBSD map where points indexed as cubic YAG are in green and points indexed as alumina are in red, there is also an image quality overlay so that the grain and phase boundaries are evident. Some points that are indexed as YAG are clearly not correct. (b) EDS map where the blue represents yttrium atoms, green represents silicon, and red represents aluminum. (c) EDS map showing only Si signal – the combination of the EBSD and EDS results makes it clear that the second phase precipitates are a Si-rich YAG phase. ..... 146

## List of Tables

<b>Table 2.1.</b> Common plane facets in alumina.....	35
<b>Table 3.1.</b> Polishing procedure for dense alumina samples .....	42
<b>Table 5.1.</b> Summary of processing parameters used in the sample preparation. ....	69
<b>Table 5.2.</b> EBSD clean-up parameters and results .....	69
<b>Table 6.1.</b> Statistical results of Grain Boundary Energy Distribution .....	93
<b>Table 7.1.</b> Grain size and transformation statistics at different times and temperatures.....	104
<b>Table 8.1.</b> Range of values for thermodynamic segregation calculations in Y-doped alumina	136

## List of Symbols and Abbreviations

### *In Alphabetical Order*

AFM	Atomic Force Microscope
AGG	Abnormal Grain Growth
BSE	Back Scatter Electrons
CalPhaD	Calculation of Phase Diagrams (program)
CI	Confidence Index
CSL	Coincident Site Lattice
EBSD	Electron Backscatter Diffraction
EDS	Energy Dispersive x-ray Spectroscopy
EELS	Electron Energy Loss Spectroscopy
EPFL	École polytechnique fédérale de Lausanne
FEI	FEI Company, makes electron microscopes
G or GS	Refers to the average grain size of a population
GBCD	Grain Boundary Character Distribution
GBPD	Grain Boundary Plane Distribution
GBE	Grain Boundary Energy
HDPE	High Density Polyethylene
HRTEM	Hi-Resolution Transmission Electron Microscopy
HAADF-STEM	Hi Angle Annular Dark Field – Scanning Transmission Electron Microscopy
IPF	Inverse Pole Figure
MDF	Misorientation Distribution Function

MRD	Multiples of a Random Distribution
MURI	Multi University Research Initiative
NGG	Normal Grain Growth
OIM	Orientation Imaging Microscopy (TM by EDAX-TSL)
ONR	Office of the Naval Research Lab
PTFE	Polytetraflouroethylene, also known as Teflon
SEM	Scanning Electron Microscope
SPM	Scanning Probe Microscopy
SPS	Spark Plasma Sintering
STEM	Scanning Transmission Electron Microscopy
TEAM	EDS and EBSD dual acquisition software by EDAX-TSL
TEM	Transmission Electron Microscope
TSL	EBSM manipulation program by EDAX (Mahwah, NJ)
TTT	Time Temperature Transformation
YAG	$Y_3Al_5O_{12}$
YAP	$YAlO_3$
YAM	Yttrium aluminum monoclinic

# 1. Introduction

## 1.1 Motivation

A grain boundary complexion is a distinct structure and/or composition found at the interface between two grains. A discontinuous change in this structure with a change in temperature, pressure, or composition - analogous to a two-dimensional phase transition- is known as a complexion transition. When a complexion transition occurs, there can be an abrupt change in the grain boundary properties, which can result in a significant difference in microstructure development. For instance, the co-existence of two complexions with different mobilities in the same bulk polycrystal can lead to abnormal grain growth<sup>1-3</sup>. Also, the co-existence of two complexions with different mobilities, which form on specific boundary orientations, can lead to high aspect ratio grain morphologies<sup>4</sup>.

The current work is motivated by the need to control grain size distributions in ceramic microstructures. This thesis asserts that it is possible to manipulate the microstructure of doped ceramics through the understanding and control of complexion transitions. It has been shown that AGG causes a decrease in the energy of the boundaries surrounding abnormally large grains and increases the population of preferred grain boundary planes<sup>5, 6</sup>. This work re-examines these findings while taking the idea one step further in an attempt to control when and where complexion transitions will occur. Kinetic measurements of complexion transitions along high and low energy interfaces will be recorded as a function of time and temperature, with the goal of making a time-temperature transformation (TTT) diagram that includes the effect of different grain boundary types.

The current work was done in collaboration with Lehigh University and École Polytechnique Fédérale de Lausanne (EPFL) with the intention of sharing processing

technologies, analytical skill sets, and general knowledge to gain a better understanding of ceramic grain boundaries. Together we were able to explore multiple length scales to gain a complete understanding of the conditions that promote the transformation of a grain boundary from one complexion to another. This research will allow for improved control and advanced engineering of grain boundaries in ceramics and ultimately tailoring of specific properties.

## **1.2 Hypothesis**

There is evidence that the grain boundary energy is one of the factors that determines the probability that a complexion transition will occur. Because the character of the grain boundary determines the grain boundary energy, it should be possible to predict the locations of complexion transitions based on knowledge of the grain boundary character. If so, it is also possible to control the grain size and morphology. The following are specific hypotheses that will be tested by this research.

1. There will be an increase in the width of the grain boundary character distribution when a complexion transition that results in AGG occurs. This will indicate that an equilibrium complexion has nucleated along specific grain boundary planes or at specific misorientations.
2. The mean relative energies of grain boundaries surrounding abnormally large grains will be less than the mean relative energies of boundaries surrounding normal sized grains adjacent to and far away from the abnormal grains. Because AGG is an indicator of a transition from a metastable to equilibrium grain boundary complexion, it is possible to determine that the metastable complexion is higher in energy than the transformed equilibrium complexion.

3. A complexion transition is most likely to occur on the highest energy grain boundaries first. By controlling the character and thus energy of single crystals embedded in a doped-polycrystalline matrix, it is possible to measure the pre and post-transformation boundary energies and to track the degree of transformation along the controlled interfaces using AGG as an indicator for a complexion transition.
4. It will be possible to control the rate of a complexion transition by controlling the processing temperature and character of the grain boundaries. Previous results have shown that complexion transformations are thermally activated, as are bulk phase transformations. Therefore, changes in driving force for transformation and the kinetics of transport with temperature should affect complexion transformations the same way that they affect normal bulk phase transformations. It should be possible to depict the rate of complexion transitions on a time temperature transformation diagram.
5. It will be possible to measure the mesoscale grain boundary energy as a function of thermal grooving temperature and dopant concentration through a temperature range displaying a complexion transition. Grain boundary complexion transitions are dependent on both grain boundary energy and temperature. Therefore a maximum mean grain boundary energy is expected in Y-doped alumina at 1450 °C - before the complexion transition occurs on most boundaries. A complexion transition will cause a decrease in mean grain boundary energy at 1500 °C – the temperature at which a significant abnormal grain growth is typically observed. When a fully transformed sample (heated to 1650 °C) is re grooved at lower temperatures, the grain boundary

energy will remain constant, implying that a reverse complexion transition has not occurred.

### **1.3 Objectives**

In this work, the previously stated hypotheses will be experimentally tested in multiple ceramic systems. Automated Electron Backscatter Diffraction (EBSD) and Atomic Force Microscopy (AFM) will be used in concurrence with various analytical tools to determine the effect of grain boundary character and energy on complexion transitions. Proper characterization of these mesoscale grain boundary properties will lead to a greater understanding of grain boundary properties and how they effect microstructure development.

## **2. Background**

### **2.1 Complexions**

A fairly new idea in interfacial engineering and materials science is the concept of complexions. Because of the developing nature of the research, and the fact that interfaces themselves have been thoroughly studied for many years prior to the coinage of the word “complexions”, the terminology used to explain these interfacial phenomena is not always consistent. A recent review focused on clearly defining what a complexion is can be found in reference <sup>7</sup>. In that review, lead researchers in the field have developed a standard definition for, and further elaborated on what specifically qualifies a complexion:

*A complexion, concisely defined, is interfacial material or strata that is in thermodynamic equilibrium with the abutting phase(s) and has a stable, finite thickness that is typically on the order of 0.2-2 nm. A complexion cannot exist independently of the abutting phase and it's composition and structure need not be the same as the abutting phase<sup>7</sup>.*

While the current work presented in this thesis focuses solely on discrete grain boundary complexions that exist in ceramics, the following sub-sections provide a brief introduction to the entire field of complexions. This will focus on various classifications of complexion types, followed by methods to characterize complexions and their transitions, and finally discussion of practical applications of this research.

#### **2.1.1. Classification**

Grain boundary complexions have been theoretically and computationally predicted for decades. In the 1960's, Hart postulated that atoms adsorbed on interfaces would undergo a two-dimensional phase transformation, analogous to a bulk phase transformation. This was presented

as a means to explain temper embrittlement in steels<sup>8</sup>. Cahn further addressed the subject of equilibrium grain boundary “phase” transitions, introducing the concept of grain boundary phase diagrams and boundary phase change mechanisms<sup>9</sup>. However, according to Gibb’s strict definition of a phase, two-dimensional phases are not truly phases because they cannot exist in thermodynamic equilibrium independent of the abutting grains. While the standard thermodynamic state variables (temperature, pressure, and chemical potential) are used to define both a bulk and a boundary phase, the boundary state also depends on geometric variables defining the misorientation and boundary plane normal. Therefore, the use of the term “phase” to describe the structure and chemistry of a grain boundary was not ideal. To address this problem, in 2006, Tang et al. introduced the term “complexion” to describe these equilibrium interfacial states<sup>10</sup>. Since then, the term complexion has been used to define any sort of interface- from a solid-vapor interface, to phase boundaries, and also grain boundaries, which are the subject of this thesis.

Interfacial complexions can be categorized in many ways. The most basic classification of a complexion is whether it is intrinsic - which can be found in single-component systems where the interface is free of any adsorbed solute, or extrinsic – where solute is adsorbed to the interface. Extrinsic complexions can further be divided based on the structural and chemical order of the atoms at the boundary.

The most thoroughly researched and documented work on complexions was completed by Dillon et. al. on doped aluminas<sup>1, 11</sup>. These are now known as Dillon/Harmer discrete complexions, and are classified by the thickness of the grain boundary core which is then simplified to be represented by an integer number of adsorbed atomic layers such as: monolayers, bilayers, and intergranular films. These complexions are distinguished by

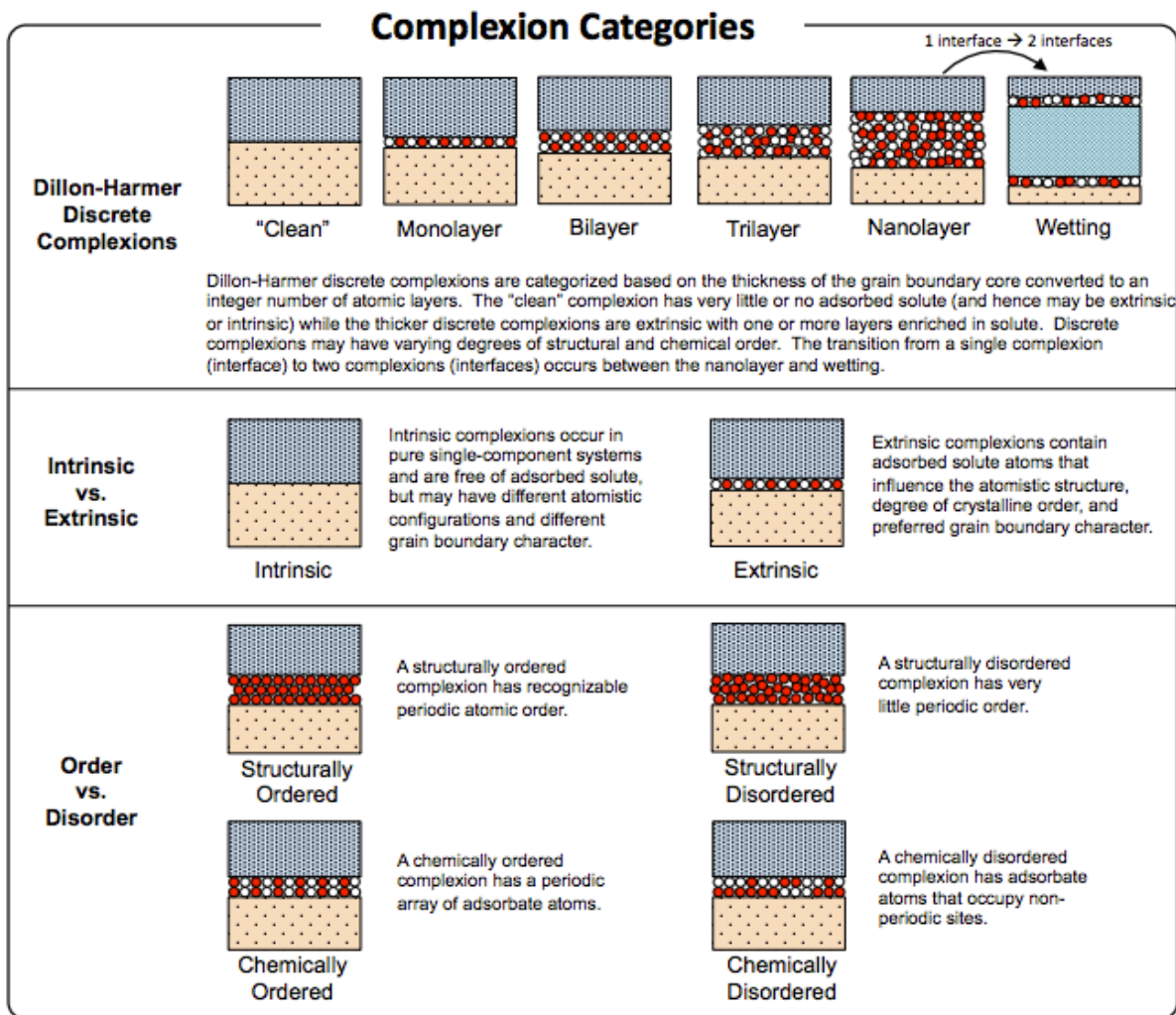
simplifying the boundary to an equivalent thickness, and are not classified solely based on the local structure of solute at the boundary. So, for instance, a monolayer of a solute on the (111) boundary plane of an FCC material would not have the same coordination and/or local chemistry as a monolayer on the (100) plane – this becomes more complicated when interfacial steps occur leaving more potential adsorption sites. Additionally the term “wetting” complexion is also known as dissociation and refers to the dissociation of a single interface to two separate interfaces. There has been much discussion regarding the proper use of the term wetting to explain such a dissociation, so it should be stated that the distinguishing feature of a wetting layer is its arbitrary thickness<sup>12</sup>. However, regardless of the specific terminology, discrete complexions allow for a convenient way to represent the segregation, structure, and degree of disorder of the boundary plane.

Finally, a complexion can be characterized by the degree of order of the boundary. For example, the addition of  $\text{Bi}_2\text{O}_3$  added to ZnO results in a disordered intergranular film at the boundaries. The formation of this film results in activated sintering as well as enhanced varistor properties<sup>13</sup>. Both the chemical and the structural order can be used to classify the grain boundary complexion type. Figure 2.1 a presents a more detailed schematic of the common complexion classifications.

A complexion transition occurs when an interface transforms from one complexion type to another. These transitions can be classified in terms of the change in character of the adjacent phases, regardless of the change in structure/chemistry of the complexion itself. A congruent complexion transition has occurred if the misorientation and boundary plane normal do not change with the transformation. Recent work, which will be discussed in further chapters of this document, has shown that complexion transitions resulting in abnormal grain growth result in

anisotropic grain boundary character distributions – or preferred boundary plane orientations<sup>5, 14</sup>.

In these cases, a faceting or non-congruent transition occurs. This type of faceting transition implies that the complexion type affects the interfacial free energy of certain crystal orientations, resulting in a driving force for low energy interfaces to grow at the expense of higher energy interfaces. Finally, the dissociation transition of a wetting film can also be considered a complexion transition type. Figure 2.1 b summarizes the basic complexion transition classifications.



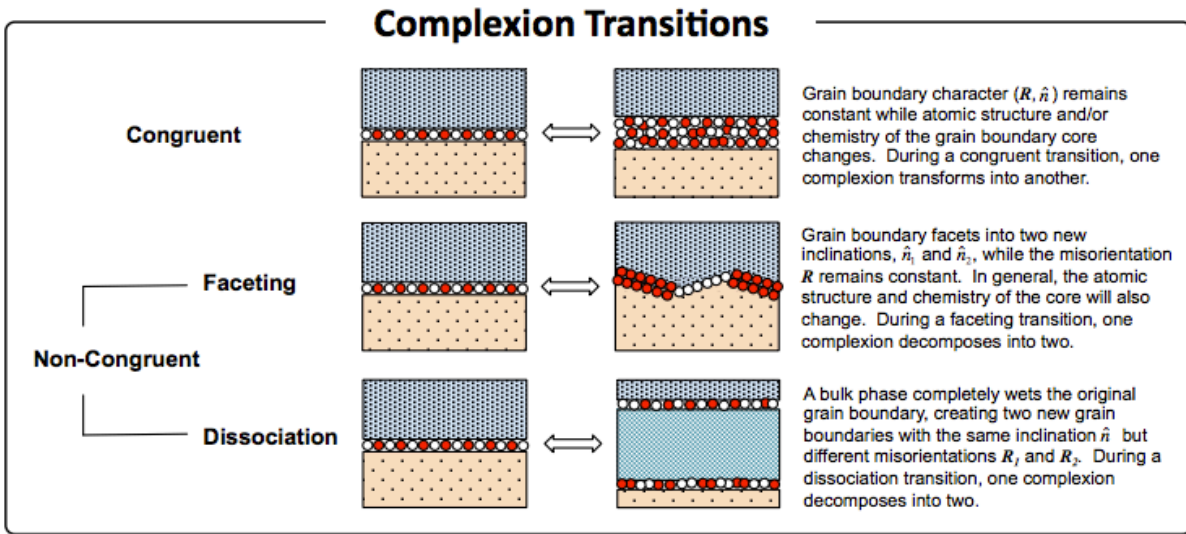


**Figure 2.1.** Summary schematics of various categories of complexions (a), and means of transitioning between two different complexion types (b). This figure was reproduced from reference<sup>7</sup>.

## 2.1.2. Characterization

### 2.1.2.1 Atomic-resolution analysis

Many detailed studies have investigated the degree of solute segregation to grain boundaries using high-resolution imaging techniques such as aberration corrected high-resolution transmission electron microscopy (HR-TEM), high angle annular dark field scanning transmission electron microscopy (HAADF-STEM), electron energy loss spectroscopy (EELS), TEM energy dispersive x-ray spectroscopy (EDS), and atom probe tomography<sup>1, 11, 15–20</sup>. These methods allow for precise and accurate measurements of the chemistry and structure of grain boundaries at sub-nanometer resolution. The results obtained from these experiments have led to a better understanding of the changes in morphology and properties of grain boundaries that have experienced a complexion transition. However, the characterization methods listed above are time intensive and extremely selective. This makes it difficult or impossible to analyze a representative fraction of the many different types of grain boundaries in a bulk material.

### ***2.1.2.2 Mesoscale analysis***

An understanding of the mesoscale – a scale capable of representing the bulk material – is essential in linking the sub-nanometer structure of a few grain boundaries to the bulk or macroscale. The measurement of grain growth as a function of time and temperature allows for the determination of grain boundary mobility. It has been found that an abrupt change in grain boundary mobility is often an indicator of a complexion transition in that boundary<sup>3,4,11</sup>. Experimentally measured grain boundary properties such as the grain boundary character and energy distributions also offer a better understanding of how complexion-forming dopants affect the majority of the grain boundaries in the microstructure. It has also been found that complexion transitions increase the width of the grain boundary character distribution and decrease the grain boundary energy<sup>5,6,14,21</sup>.

The first paper to introduce the term “complexion”, by Tang et al.<sup>10,22</sup>, used a diffuse interface model to determine that the tendency for increasing disorder of a grain boundary was dependent on increasing temperature and increasing misorientation of the specific boundary. It was also stated that these ordered-disordered transitions often occur at the higher end of the grain boundary energy spectrum. From this it can be hypothesized that complexion transitions that increase disorder of a boundary will occur on higher energy boundaries first. In Tang’s investigation, only the misorientation of the boundary was thoroughly investigated, leaving out the grain boundary plane. However, a subsequent experimental investigation linking the diffuse interface model to experimentally determined grain boundary structures and kinetic properties stated that there is a definitive effect of grain boundary plane and misorientation on the stability of complexions, at least for the alumina system. This stability changed with dopants, where

calcium doping caused decreased segregation to the basal plane and neodymium doping increased the degree of segregation to the rhombahedral plane<sup>1</sup>.

The assumption that high energy metastable grain boundaries are more likely to transform to a more disordered equilibrium structure led to direct mesoscale experimental measurements of relative grain boundary energy distributions comparing boundaries surrounding abnormally large grains (which already transformed to a more disordered complexion) and boundaries around grains with the typical size<sup>6</sup>. These results showed that in some cases, the transformed boundaries that surround large grains exhibit significantly lower mean relative grain boundary energy than the adjacent untransformed boundaries. A similar study was conducted investigating the distributions of grain boundary planes before and after abnormal grain growth resulting from a complexion transition<sup>5</sup>. It was found that the apparent complexion transitions increased the population of specific grain boundary planes— implying that the higher mobility complexion favored specific grain boundary planes.

The following document will continue to focus on understanding the mesoscale grain boundary character and energy dependence of complexion transitions resulting in abnormal grain growth in ceramic materials. In this work, the main analytical tools used were automated electron backscatter diffraction, atomic force microscopy, and scanning electron microscopy (SEM).

### **2.1.3 Grain Boundary Properties**

Grain boundary complexion transitions affect both the macro scale grain boundary properties such as grain boundary character and energy distributions, as well as the bulk properties of a material such as thermal conductivity, strength, creep resistance, and electrical conductivity. As mentioned previously, the addition of Bi<sub>2</sub>O<sub>3</sub> to ZnO results in a disordered

intergranular film that enhances the varistor, or non-linear current voltage properties of the material<sup>13</sup>. Additionally, the addition of a small amount of Y to Al<sub>2</sub>O<sub>3</sub> decreases the grain boundary mobility and significantly increases the creep resistance compared to pure alumina<sup>23-25</sup>. These effects, however, are not always positive. For example, the formation of a Bi bilayer in Ni causes grain boundary embrittlement<sup>15</sup>. There are other examples of an apparent grain boundary complexion leading to a distinct shift in bulk properties of a material<sup>2, 7</sup>.

#### **2.1.4 Grain Boundary Complexion Diagrams**

The continued investigation of what complexion is stable as a function of temperature and composition has led to the tabulation of experimentally determined complexion diagrams<sup>7</sup>. Theoretical diagrams have also been calculated using Calculation of Phase Diagrams (CalPhaD), and other methods<sup>26,7, 10</sup>. A complexion can be defined by standard thermodynamic variables such as temperature, chemical composition, and pressure, however the character of the grain boundary must also be considered. Understanding that there are 6+C degrees of freedom in a single complexion system makes drawing bulk phase equivalencies for complexion transitions a daunting task. For example, a grain boundary character distribution describes the relative areas of the grain boundaries as a function of the five crystallographic variables, under the condition that the thermodynamic variables are held constant.

Other, more traditional phase-like diagrams have also been proposed for complexion transformations. Reference (7) summarizes much of the research that has been conducted on the compilation of interface complexion diagrams. The majority of these diagrams vary the composition, temperature, or pressure to determine what bulk phases and grain boundary complexions will exist at various processing conditions. A diagram of particular interest to the current work can be seen in Figure 2.2, where the composition of yttria in alumina is analyzed as

a function of temperature. This represents a binary complexation diagram that shows an equilibrium occurrence of a bimodal grain size distribution both in the presence of a bulk second phase and without a noticeable second phase. A major question regarding these and similar results, however, was if the complexion coexistence region is an equilibrium state or a function of transition kinetics? And if it is an equilibrium state, what are the criteria for the nucleation of a complexion transition?

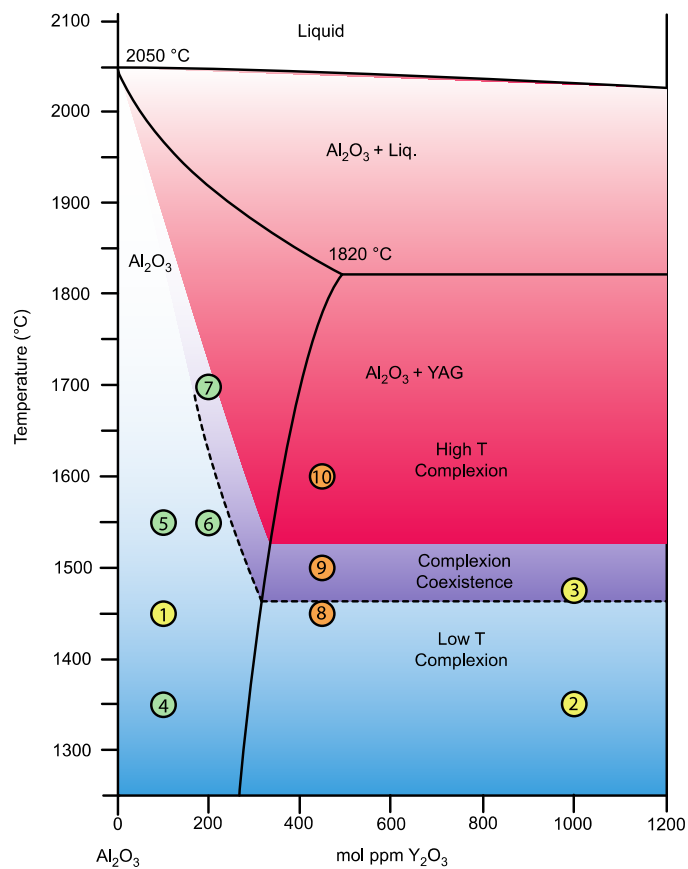


**Figure 2.2:** Reproduced from Reference <sup>7</sup>. Experimental complexation diagram for  $Y_2O_3$ - $Al_2O_3$  showing regions in which a low temperature complexion with low grain boundary mobility (blue) and a high temperature complexion with high mobility (red) are stable. Normal grain growth occurs in both regions. There is a region of overlap where it is believed that both complexions may coexist (purple). It is believed that abnormal grain growth occurs in this region because the high T complexion has a significantly larger grain boundary mobility than the low T complexion.

### **2.1.5 Mechanisms for abnormal grain growth**

Abnormal grain growth is characterized by a bimodal grain size distribution, where some grains in the microstructure grow much faster at the expense of surrounding smaller grains.

While the majority of this document refers to the cause of such abnormal grain growth as a result of the coexistence of multiple grain boundary complexions that exhibit different grain boundary mobilities, previous work has also shown that coarsening can also result in a bimodal grains size distribution<sup>27</sup>. The following paragraphs briefly summarize the different microstructure characteristics for these two theories of abnormal grain growth in doped ceramic materials. Throughout this section, grain growth will be referred to as atomic motion across grain boundaries while coarsening will be referred to as dissolution and precipitation of a material through an intervening phase<sup>28</sup>. The following paragraphs summarize coarsening from references (<sup>27,28</sup>) and abnormal grain growth from references (<sup>1,3</sup>).

#### **2.1.5.1 Coarsening**

In the classical coarsening theory, a crystal is in contact with a second phase with a fixed chemical potential. The driving force for coarsening is given by the free energy difference between the crystal and the second phase. In most coarsening models, a bimodal grain size distribution cannot be established. However, the nucleation-limited coarsening theory presents a coarsening mechanism that has been shown to result in a transient bimodal grain size distribution. In nucleation-limited coarsening, two-dimensional nucleation of atomic planes on a faceted interface can be thermally activated, and in cases where nucleation can not occur, growth can only occur through persistent step defects at that interface<sup>28</sup>.

There are four experimentally testable criteria for nucleation-limited coarsening. First, coarsening would result in a transient bimodal distribution, where an initially unimodal grain size

distribution would eventually become bimodal. The presence of step producing defects at some, but not all of the crystal interfaces would allow for the defected surfaces to advance, which would allow for grain coarsening. Other grains that do not exhibit the critical number of step producing defects would not be able to overcome the nucleation energy barrier and would not coarsen. Because step-producing defects are required for the initiation of abnormal grain coarsening, the number density of the large grains should be constant over time. Conversely, the number density of the small grains would decrease because the large grains are coarsening by using the material in the small grains. Finally, since the small grains cannot coarsen they would ideally remain the same size over the same time frame – this is not typically the case because grain growth would also occur in the sample. Because the onset of coarsening is dependent on the presence of step producing defects, the number density of abnormal grains should not change with increasing temperature<sup>27</sup>.

#### **2.1.5.2 Grain Growth**

Grain growth is considered to be the movement of atoms from one side of a grain boundary to another. As with coarsening, the driving force for grain growth is the minimization of interfacial free energy of the system by minimizing the interface area. It has also been shown that the structure, chemistry, and thickness of the grain boundary can have a significant influence on the grain boundary mobility<sup>1,3,4</sup>. The theory of grain boundary complexions, in particular, shows that the boundary mobility can vary over several orders of magnitude with the occurrence of multiple complexions in the same system at the same time and temperature. This increase in mobility is due to the increased disorder of the interface with increasing amounts of solute adsorbed to the boundaries. The increased disorder allows for faster transport of atoms from one grain to another. The mobility may be further amplified because the energy of the high

temperature equilibrium boundary is typically less than that of the metastable untransformed boundaries surrounding the small grains<sup>1</sup>. It is assumed that the solute structure of an ordered complexion is preserved with grain growth, and excess solute beyond the grain boundary saturation limit would be either propagated into the surrounding grains or expelled to a second phase.

While investigating abnormal grain growth caused by a change in grain boundary complexions, the number density of abnormal grains has been shown to increase linearly with grain size<sup>29</sup>. Since grain size increases with time, this would indicate that the number of abnormal grains increases over time until the abnormal grains impinge on each other<sup>29</sup>. The number density of abnormal grains also increases with grain boundary excess, however it should also be noted that there is always a balance between precipitation of a second phase and formation of a more disordered complexion<sup>30</sup>. Additionally, the number density of abnormal grains increases exponentially with temperature giving insight to the nucleation energy requirements for the change in complexion that leads to abnormal growth. It was hypothesized that there will only be a certain number of grains that will undergo the complexion transition and have the significant mobility advantage. Chapter 7 in the current work will further investigate the dependence of temperature and grain boundary character on the rate of a transition that leads to abnormal grain growth.

## **2.2 Interfacial and Grain Boundary Energy**

The surface of a crystalline material has an interfacial free energy because of the broken bonds of that surface. Because the coordination number of atoms on different planes varies in a given crystal structure, each plane surface has a different interfacial energy. Continuing with this reasoning, when two different surfaces come together they form a boundary. The formation of

that boundary will allow for some of those broken bonds to re-form, thus decreasing the net energy of both surfaces. However, there is still an interfacial energy because the energy of the new bonds will not exceed those broken to form the surfaces. The following sections will first explain the origin of interfacial energy anisotropy and its correlation with boundary orientation, and then further examines the components of interfacial energy between grains – or the grain boundary energy of a material.

### 2.2.1 Wulff shape

A common way to represent the anisotropy or change in surface energy as a function of crystal orientation is a  $\gamma$ -plot, which shows the crystallographically determined orientation dependence of surface energy for a single crystal. Figure 2.3 a shows an example of a Wulff construction on a  $\gamma$ -plot where the length of each vector represents the surface energy and the direction represents a crystallographic direction, the corresponding crystallographic plane is perpendicular to the end of the vector. Low energy crystal facets occur at the orientations of the cusps in the  $\gamma$ -plot. To reach an equilibrium shape, the crystal surface minimizes its interfacial free energy by increasing the relative area of the lower energy interfaces. In the  $\gamma$ -plots, such as in Figure 2.3, the inner envelope of all of the tangent planes represents the equilibrium shape of the crystal (Figure 2.3 b).

Regardless of complexity, a crystal's Wulff shape depends on both its crystal structure and its surface chemistry. It has been found that, in some ceramics, small amounts of dopants can preferentially adsorb to specific boundary planes, thus decreasing that plane's interfacial free energy and changing the preferred plane facets for that system. In doped alumina, for example, 10 ppm of yttrium added to alumina will lead to a change in the preferred facets of the crystal's Wulff shape.<sup>31</sup> Overall, understanding the basic idea of surface energy dependence on

crystallographic character and the resulting equilibrium geometries gives the building blocks for understanding grain boundary energy.

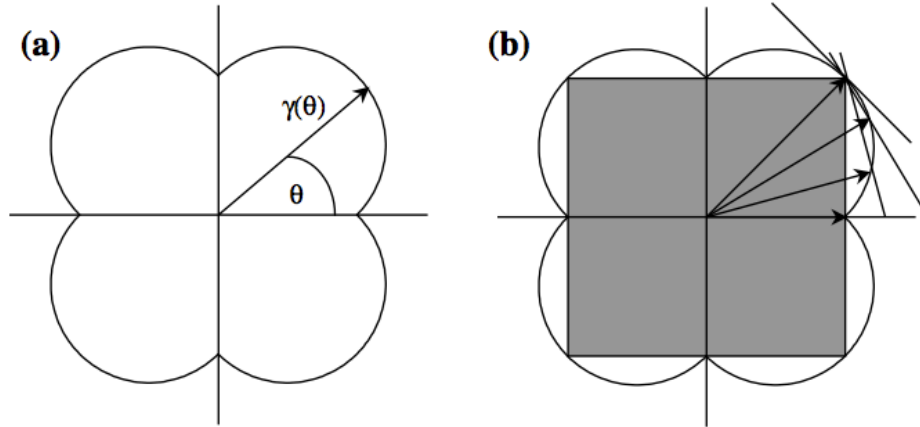


**Figure 2.3.** Simplified example of a  $\gamma$ -plot where the X and Y-axis represent crystallographic directions and the surface energy is a function of  $\theta$ , which determines a point in the crystallographic space (a). The Wulff shape is the inner cusp of lines drawn perpendicular to the  $\gamma$  vectors (b). Image reproduced from reference <sup>32</sup>.

### 2.2.2 Grain Boundary Energy

When two single crystals join together at a boundary, it is assumed that  $\gamma_{b1} + \gamma_{b2} + B = \gamma_{gb}$ .

Where B is the reduction of energy when the two surfaces (with energies  $\gamma_{b1}$  and  $\gamma_{b2}$ ) join together- effectively eliminating some of the broken bonds at the boundary. In this way of thinking, there are two possible ways to create a lower grain boundary energy ( $\gamma_{gb}$ ). First, if there were a high coincidence of the atoms on each side of the boundary – this would increase the number of bonds across the boundary and decrease the boundary energy. It has been shown, however, that this is not the case for all boundaries showing high coincidence<sup>33, 34</sup>. Second, if the planes on each side of the boundary had low energy orientations then the boundary itself would be lower in energy. In general, it has been found that the grain boundary population is inversely proportional to the corresponding grain boundary energy<sup>35</sup>. In the remaining part of section 2.2,

grain boundary energy, and in particular relative grain boundary energy measurements are described in detail.

### 2.2.3 Historical Derivation

A thermal groove, which is shown in Figure 2.4, is formed when a polycrystal is held at an elevated temperature wherever a grain boundary intersects the sample surface. This is a result of the balance of interfacial energies as described by Herring's equation<sup>36</sup>.

$$\gamma_i \mathbf{t}_i + n_i \frac{\partial \gamma_i}{\partial \theta} = 0 \quad (2.1)$$

where  $\gamma_i$  is the excess free energy of the  $i$ th interface,  $\mathbf{t}_i$  is the unit vector that lies in the  $i$ th interface which is normal to the line of intersection (l) of the three interfaces and  $\mathbf{n}_i$  is the unit vector normal to the line of intersection such that  $\mathbf{n}_i = \mathbf{t}_i \times \mathbf{l}$ . These can be seen in the schematic of Figure 2.4 a. It is a common assumption in experimental work, however, that the torque term ( $\frac{\partial \gamma_i}{\partial \theta}$ ) is negligible, and the groove forms by surface diffusion thus giving the grain boundary energy as a function of only the adjacent grains crystallographic orientation and not the tangent plane<sup>37</sup>. The relative grain boundary energy compared to the free surface of the grains is represented in equation 2.2.

$$\frac{\gamma_{gb}}{\gamma_s} = 2 \cos \frac{\psi_s}{2} = 2 \sin \beta \quad (2.2)$$

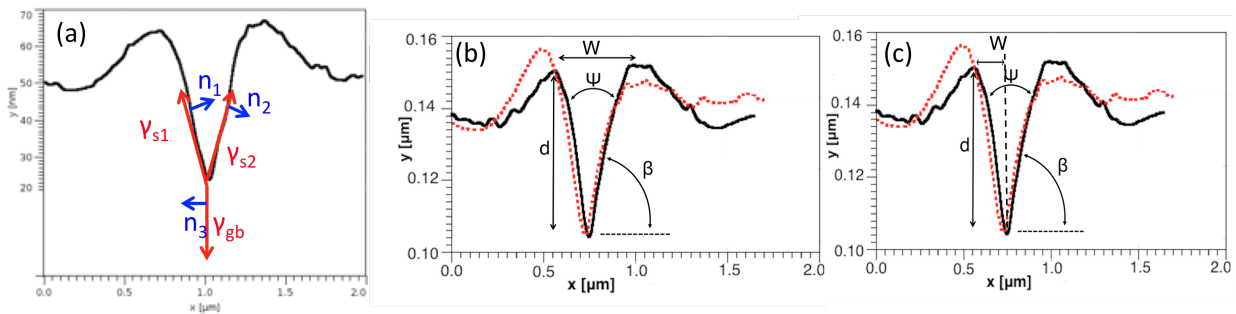


**Figure 2.4.** Examples of grain boundary thermal groove line profiles, where: the interfacial energy and torque terms are labeled in (a). The parameters for the Mullins' analysis of the complete dihedral angle (b), and modified Mullins analysis using the half angle (c).

## 2.2.4 Experimentally Determining Relative Grain Boundary Energy

A thorough overview of the history of grain boundary energy measurements can be found in reference<sup>33</sup>. The method used in this document was derived by Mullins<sup>38</sup>, where by assuming the groove to be symmetric, he determined that by measuring the width and height of the grain boundary thermal groove, as seen in Figure 2.3b, the relative grain boundary energy could be calculated. Under the assumptions that the groove formed from surface diffusion, independent of crystal orientation, and the grain boundary plane was perpendicular to the sectioned surface. Equation 2.3 allows for the calculation of the grain boundary groove angle ( $\beta$ ) from experimentally measured width ( $w$ ) and depth ( $d$ ) of the thermal groove using the parameters in Figure 2.4 b.

$$\beta = \tan^{-1}(4.73 \frac{d}{w}) \quad (2.3)$$

This groove angle can then be used in Equation 2.2 to calculate the relative energy of the grain boundary. While some of the assumptions, such as surface diffusion forming grain boundary grooves, are accurate in polycrystalline systems, the assumption of isotropic surface energy and grain boundary planes perpendicular to the average surface orientation are not expected to be accurate for all cases.

Decades later, Saylor et al. determined that tracking the topography of thermal grooves using an atomic force microscope allowed for the accurate collection of widths and heights of the groove geometry. By measuring over 200 distinct grain boundary grooves, it was possible to effectively sample over both the variation in crystallographic orientation and inclination of the grain boundary with respect to the surface. The mean relative grain boundary energy found by this method is equivalent to other grain boundary energy results. The AFM probe dimension

error was also investigated and found to be negligible under certain experimental conditions,<sup>37</sup> this will be discussed in more detail in Chapter 8.

Saylor's statistical method has been used for multiple studies on isotropic, randomly oriented bulk polycrystalline samples. The method uses measurements of the grain boundary width and height as that illustrated by Figure 2.3 b. In this case, the full width and the heights of the ridges on both sides of the groove were measured and analyzed independently. Dillon later adapted this method to look at a single side of a groove where the width was taken as twice the horizontal distance from the ridge to the minimum point, as illustrated in Figure 2.3 c – this makes it possible to estimate the energy of the interface with a second phase or between a polycrystal and a single crystal<sup>5, 30</sup>. Both Saylor's and Dillon's techniques will be used as part of this thesis.

### **2.2.5 Temperature dependence of grain boundary energy in impure systems**

The grain boundary energy of both pure and impure materials can be analyzed by using the surface excess grand potential found in equation 2.4.

$$\gamma = e^s - T s^s - \sum_i \mu_i \Gamma_i \quad (2.4)$$

Where it can be seen that the energy of the interface is dependent on the internal specific energy ( $e^s$ ), which would remain constant with temperature. The specific entropy of the boundary ( $s^s$ ) is positive - implying that the boundary becomes more disordered at higher temperatures. The negative contribution of the entropy term in equation 2.4 would thus cause the boundary energy of a pure material to decrease with increasing temperature. However, when the specific interfacial excess ( $\Gamma_i$ ) of an adsorption of component  $i$ , and the chemical potential ( $\mu$ ) of component  $i$  are also considered, the energy will increase with increasing temperature. This is

due to a Langmuir-McLean adsorption effect (equation 2.5)<sup>39,40</sup>, where the temperature dependence on adsorption is greater than the entropy contribution to the interfacial energy.

$$\frac{x^s}{1-x^s} = \frac{x}{1-x} \exp\left(-\frac{\Delta H_{seg}}{RT}\right) \quad (2.5)$$

Where the grain boundary atomic fraction of adsorbent at the interface ( $x^s$ ) exhibits an Arrhenius temperature dependence. This fraction can be directly related to the interfacial excess. The temperature dependence of grain boundary energy in undoped systems will be discussed in more detail in Chapter 8.

### 2.3 Grain Boundary Characteristics

A grain boundary can be fully characterized using five macroscopic parameters. These include a representation of grain boundary misorientation, typically given as three Euler angles ( $\phi_1, \Phi, \phi_2$ ), and the grain boundary plane orientation in terms of two spherical angles ( $\phi$  and  $\theta$ ) - which define the orientation of the boundary with a polar and azimuthal angle in the crystal reference frame. The following section will summarize the mathematical calculations used to determine the grain boundary character distribution, and the resulting graphical representations. All of the calculations are done in an orthogonal coordinate system; non-orthogonal (such as hexagonal and rhombohedral) crystallographic axes must be represented in an orthogonal reference frame – the conversion from hexagonal to orthogonal can be found in section 2.5.2.

#### 2.3.1 Misorientation

The crystallographic orientation of a single grain is often represented in the sample, or laboratory, reference frame using Euler angles. In the case of Bunge Euler angles, the first rotation ( $\phi_1$ ) represents a rotation about the sample z-axis/the [001] crystal direction. The second angle ( $\Phi$ ) represents a rotation about the [100] crystal axis. The final rotation ( $\phi_2$ ) is a rotation about the crystal's [001] axis. These rotations can be visualized in Figure 2.5. To represent the

complete orientation of a single grain, a transformation matrix ( $g$ ) can be computed from the measured Euler angle using equation 2.6.

$$g(\phi_1, \Phi, \phi_2) = \begin{bmatrix} \cos \phi_1 \cos \phi_2 - \sin \phi_1 \sin \phi_2 \cos \Phi & \sin \phi_1 \cos \phi_2 + \cos \phi_1 \sin \phi_2 \cos \Phi & \sin \phi_2 \sin \Phi \\ -\cos \phi_1 \sin \phi_2 - \sin \phi_1 \cos \phi_2 \cos \Phi & -\sin \phi_1 \sin \phi_2 + \cos \phi_1 \cos \phi_2 \cos \Phi & \cos \phi_2 \sin \Phi \\ \sin \phi_1 \sin \Phi & -\cos \phi_1 \sin \Phi & \cos \Phi \end{bmatrix} \quad (2.6)$$

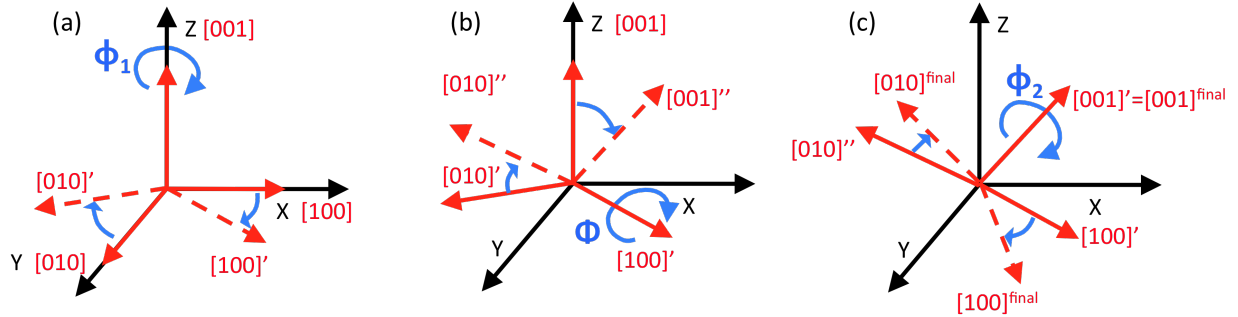


**Figure 2.5.** Bunge Euler angles showing  $\phi_1$  rotation around the crystallographic [001] axis, which is parallel to the reference frame Z-axis (a),  $\Phi$  rotation about the crystallographic [100] axis (b), and a  $\phi_2$  rotation about the crystallographic [001] axis. The black arrows show the sample/laboratory reference axis, while the red arrows represent the before (solid line) and after (dashed) crystallographic axis.

The misorientation ( $\Delta g$ ) between two grains of different orientations can be calculated using equation 2.7. To properly represent all symmetrically equivalent misorientations of a single grain boundary, the rotation matrices for corresponding Rotation groups ( $O_n^x$ ) must be applied to the calculation for each orientation. Additionally, the calculation must be done from both sides of the boundary, where in one case the transpose of grain A would be used and in another the transpose of grain B.

$$\Delta g_{AB} = O_B^x g_B g_A^{-1} O_A^x \quad (2.7)$$

While transformation matrices are convenient for crystallographic calculations, they are not always the most convenient for the meaningful representation of a given misorientation. The following are means of representing misorientations that are used in the current document.

The axis-angle pair representation gives the common axis between the two grains as well as the rotation angle about that axis that reproduces the misorientation. The axis and angle can be calculated from the  $\Delta g$  matrix using equation 2.8 and 2.9. The disorientation of a grain boundary has the minimum rotation angle for all possible representations and a misorientation axis within the standard stereographic triangle – this will be discussed in Section 2.3.2.

$$\vec{R} = \frac{(\Delta g_{23} - \Delta g_{32}), (\Delta g_{31} - \Delta g_{13}), (\Delta g_{12} - \Delta g_{21})}{\sqrt{(\Delta g_{23} - \Delta g_{32})^2 + (\Delta g_{31} - \Delta g_{13})^2 + (\Delta g_{12} - \Delta g_{21})^2}} \quad (2.8)$$

$$\cos \theta = \frac{1}{2}(\text{trace}(\Delta g) - 1) \quad (2.9)$$

A Rodrigues vector is another means of representing the misorientation of a crystal, where the vector direction is along the previously determined axis direction, and the length of the vector is proportional to the tangent of half the rotation angle, as in equation 2.10.

$$\vec{\rho} = \tan\left(\frac{\theta}{2}\right)\vec{R} \quad (2.10)$$

### 2.3.2 Representations of the grain boundary character distribution

The following summarizes various representations or projections of the grain boundary character distributions that are used in this document. In some experimental cases, one or two parameter distributions, such as misorientation angle distributions, will be used to precisely determine mesoscale trends in boundary character. These will be used in conjunction with less precise measurements of more accurately defined distributions – such as distribution of grain boundary planes about specific misorientations. Together the use of multiple grain boundary character representations allows for a well-defined picture of what boundaries are present in a bulk polycrystalline sample.

#### 2.3.2.1 Misorientation Angle Distribution

The misorientation angle distribution is a one-parameter grain boundary character distribution that represents the grain boundary population as a function of the minimum

misorientation angle of each boundary, ignoring the misorientation axis or grain boundary plane orientation. This can be calculated using equation 2.9, in section 2.3.1, and is typically represented in the form of a binned histogram. In the case of the trigonal alumina system, the maximum possible misorientation is  $104.47^\circ$ , thus the domain of the misorientation angle distribution extends from  $0^\circ$  to  $104.47^\circ$ . The red line in Figure 2.6 illustrates the random distribution of misorientation angles. When the plotted misorientation angle's intensity value is greater than that corresponding to a random distribution, then that misorientation is more likely to occur than it would in a random polycrystal. In the same way, if the relative intensity is less than random then the misorientation angle is less likely to occur. Figure 2.5 shows the misorientation angle distribution of Y+La co-doped alumina sintered at  $1600^\circ\text{C}$  and it is clear that there are significantly more boundaries with a  $60^\circ$  misorientation angle than would be expected in a random (showed in red) population of grain boundaries.

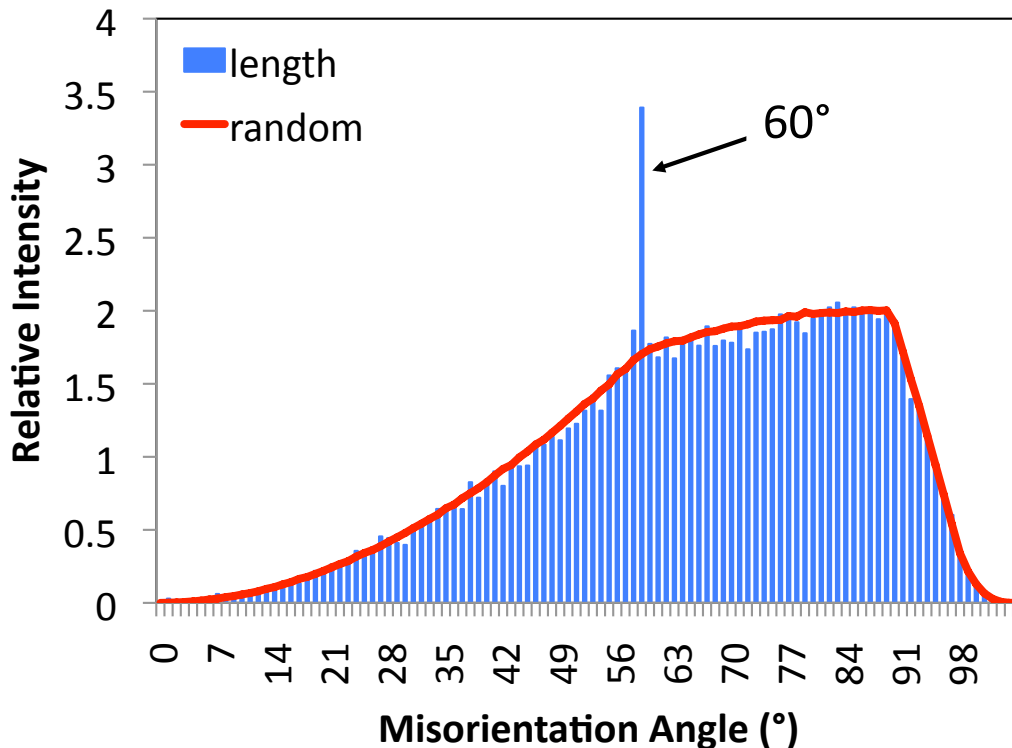


**Figure 2.6.** One-parameter misorientation angle distribution for a Y+La-doped alumina showing the normal distribution as calculated from random number generation in red and an

experimentally measured grain boundary line length weighted misorientation angle distribution exhibiting a higher than average populations of  $60^\circ$  misorientation angles.

The work summarized in this document represents the first set of data for the trigonal alumina system that contains enough grain boundaries to calculate, with statistically relevant results, the misorientation distribution with a  $1^\circ$  bin size. If a coarser discretization is used, narrow features such as the peak in Figure 2.6 are not easily detected.

### **2.3.2.2 Misorientation Distribution Function**

When the misorientation axis is also considered, a three-parameter grain boundary character representation is possible - one parameter for the grain boundary misorientation angle and two for the axis direction. This misorientation distribution function (MDF) can be represented as sections of axis angle space (equation 2.8 and 2.9) or sections of Rodrigues-Frank space (equation 2.10). An example of a section of Rodrigues-Frank space is shown in Figure 2.7 a. The Rodrigues-Frank vector has components R1, R2, and R3 and Figure 2.7a shows the R1-R2 plane for  $R3=0.32$ <sup>41</sup>. Additionally, an example of a distribution in axis-angle space is shown in Figure 2.7 b. In this example, the distribution of all boundaries with a  $60^\circ$  misorientation is shown in the fundamental zone of alumina. In both figure 2.6 a and b there is a peak (in red) at what is the [0001] axis of misorientation, however because of the discrete sections of  $10^\circ$  binning parameters in Figure 2.7, it is not possible to directly determine at what angle the maxima truly lies using the MDF. If used in conjunction with the misorientation angle distribution such as that seen in Figure 2.6, it is possible to narrow down the true misorientation in Figure 2.7 to be  $60^\circ/[0001]$ .

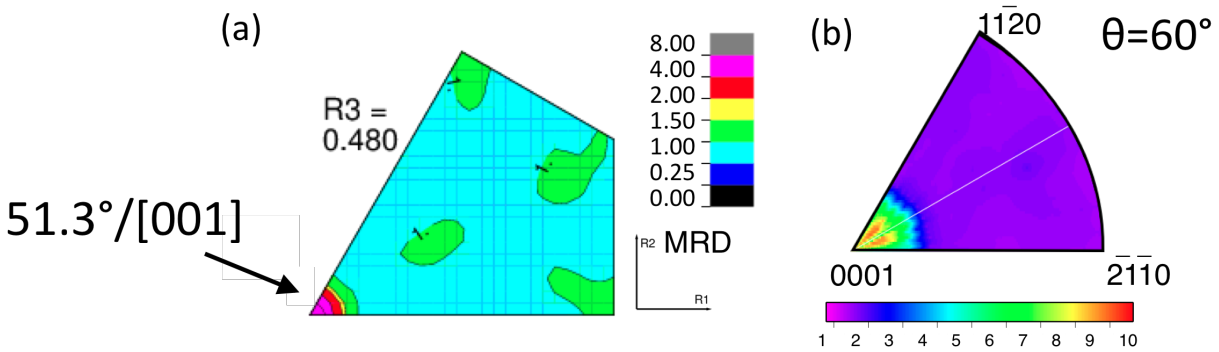


**Figure 2.7.** A two dimensional section of three-parameter Rodrigues-Frank space where  $R_3=0.32$  and  $R_1, R_2$  span the entire fundamental zone of alumina. The arrow indicates the area of Rodrigues-Frank space where the highest population of grain boundary misorientations occurs in the  $R_3=0.320$  section— this corresponds to a  $51.3^\circ/[001]$  misorientation (a). A two dimensional section of the three-parameter misorientation distribution in axis-angle pair format showing a large number of boundaries at  $60^\circ/[0001]$  misorientation (b).

### 2.3.2.3 Two-Parameter GBCD

The distribution of grain boundary planes independent of misorientation is referred to here as a two-parameter GBCD or a grain boundary plane distribution (GBPD). Grain boundary plane distributions are plotted on stereograms looking down the  $[001]$  crystal direction and have the symmetry of the crystal system. Because of this, they are typically plotted in the crystallographic fundamental zone. The fundamental zone in the GBPD reference frame is highlighted for both the cubic and trigonal systems in Figures 2.10 b and 2.11 b respectively.

The in-plane normal of the grain boundary line segment is determined by the orientation map, however the angle of inclination of the grain boundary - or the angle at which the three-dimensional boundary plane intersects the two-dimensional observed section - is not easily determined. Serial sectioning of the microstructure allows for experimental determination of the grain boundary plane normal, however this is neither a fast nor efficient means of accumulating a statistically significant amount of data that is representative of the bulk microstructure. By collecting two-dimensional EBSD maps over various regions of the sample and conducting a stereological analysis of each grain boundary line segment, it is possible to statistically determine

the distribution of grain boundary planes. It should be noted, that due to the statistical nature of a stereologically derived GBPD, conclusions regarding the character of a specific interface observed in a section plane cannot be stated with confidence.

A description of the stereological analysis used to compute a two-parameter GBCD from a two-dimensional EBSD map can be found in reference <sup>42</sup>. To summarize the process, the grain boundary in-plane normal is calculated from the observed trace on the orientation map formed by the intersection of the grain boundary with the surface. This normal is converted to the crystallographic reference frame and can be represented as a pole on the stereogram. Because the orientation of the grain boundary plane with respect to the surface is not known, a great circle can be drawn 90 ° from the pole, representing all possible grain boundary plane normal orientations in the upper hemisphere of the stereogram. This must be calculated from both sides of the grain boundary plane, and in all crystallographic rotations, just as the misorientation is calculated in Equation 2.7. For a given number of proper symmetry operators (P) and GBCD calculation resolution ( $\Delta$ ) it is possible to estimate the total number of distinguishable boundaries (N) in a given crystal system as:

$$N = \frac{8\pi^5}{4P^2\Delta^5} \quad (2.11)$$

The number of observed grain boundaries must be much greater than N for the method to yield meaningful results<sup>43</sup>. Once enough boundaries are observed, any preferred grain boundary plane orientations will appear over represented in the population of total possible boundary plane orientations. For example, the projection of a single grain boundary, where the pole of the boundary is projected on the stereographic projection and the zone of that pole is traced (one arch along the projection). The crystallographic symmetry operators (in this case group 32) are then applied to the grains to calculate all possible boundary plane orientations, as seen in Figure

2.8 a. This results in the stereogram of a single boundary clearly displaying the crystal symmetry of the material (as marked by the symmetry indicators in Figure 2.8a) – however the true preferred boundary plane cannot be determined with confidence. Figure 2.8b shows the distribution of planes when multiple grain boundary line segments are analyzed in the same manner as Figure 2.8a. After additional boundaries are analyzed, a clearer trend in preferred boundary plane becomes apparent. When a very large number of boundaries are analyzed, such as that shown in Figure 2.8c, it is possible to say with certainty that the preferred boundary plane, in this case, is the (0001) plane.

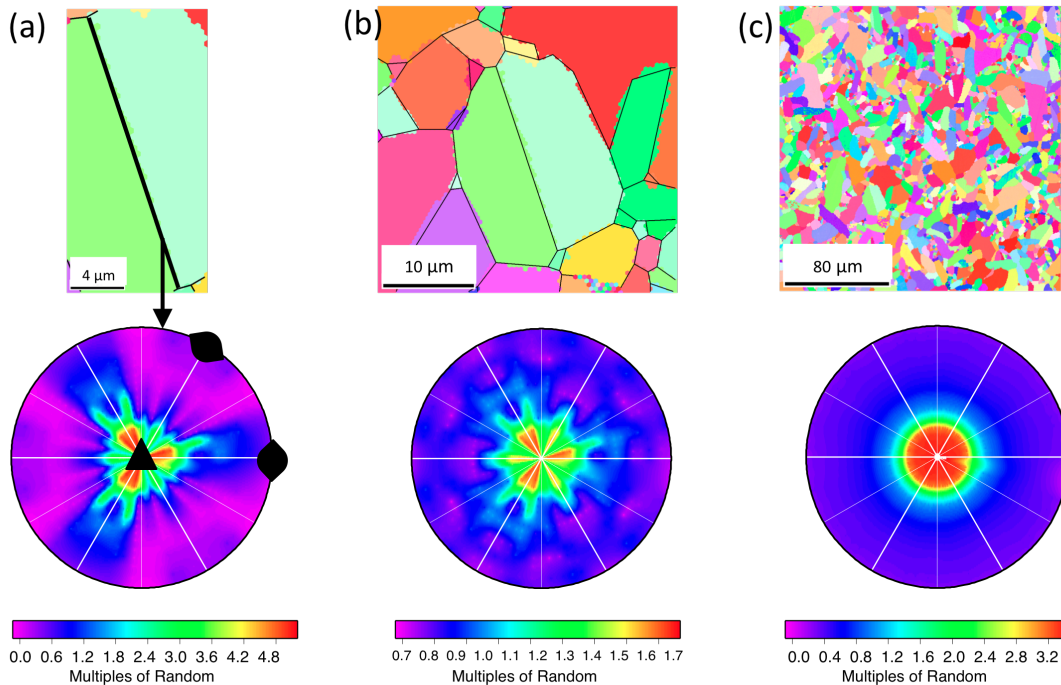


**Figure 2.8.** Progression of the two parameter grain boundary character distribution where we see one grain boundary and the corresponding 32 crystal symmetry (noted) for the alumina system, and how it is clear that this boundary is near an (0001) plane (a), 88 grain boundary line segments showing a clear trend to facet near (0001) planes (b), and 370,046 boundaries showing that most of the grain boundaries are faceted on or near the (0001) plane (c).

The scale for these plots, as well as that of the five-parameter grain boundary character distribution found in the next section, are given in multiples of a random distribution (MRD).

Each distribution is normalized such that a random distribution has the value of one MRD.

When values are less than one MRD there is a lower probability of that boundary plane occurring in the system, and values greater than one MRD indicate that the orientation is more likely to occur.

#### 2.3.2.4 Five-Parameter GBCD

The five-parameter GBCD makes it possible to plot the distribution of grain boundary planes at a fixed grain boundary misorientation. This distribution has the symmetry of the bi-crystal with the fixed misorientation and will thus always be shown in a full stereogram, such as the one in Figure 2.8. As a simple example, Figure 2.9 shows that at  $60^\circ/[111]$  ( $\Sigma 3$ ) boundaries in Ni have a very high population of (111) planes<sup>44</sup> – this corresponds to the extremely large number of coherent twin boundaries seen in the corresponding microstructure. A full description of the calculation of the five-parameter GBCD can be found in reference<sup>34</sup>.

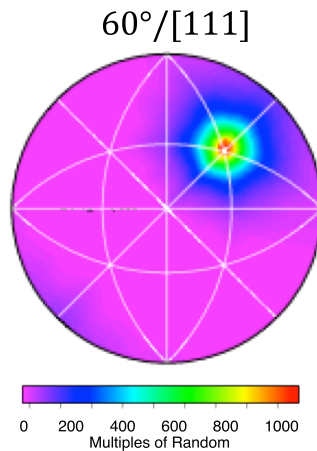


**Figure 2.9.** Distribution of grain boundary planes at a  $60^\circ/[111]$  misorientation ( $\Sigma 3$ ) for nickel. The results show a very strong preference for the (111) coherent twin boundary.

## 2.4 Texture analysis

The texture of a material is the preferred crystallographic orientation of grains in a microstructure. Throughout this document, the texture of materials will be assessed in the forms of pole figures, inverse pole figures, and inverse pole figure maps (IPF maps).

### 2.4.1 Pole Figures

A pole figure represents the distribution of normals to specific crystallographic planes in the sample reference frame. Pole figures are typically plotted on a full stereographic projection looking down the [001] sample reference frame axis. Each plot corresponds to a specific set of atomic planes in the material; the orientations of these planes in relation to the sample can be determined from the shape of the distribution.

### 2.4.2 Inverse Pole Figures

An inverse pole figure represents the distribution of crystallographic orientations with respect to a specific sample direction. Each distribution exhibits the symmetry of the crystal and can therefore be represented in the fundamental zone of the system. Inverse pole figures highlight the distribution of crystal orientations in the laboratory reference frame.

### 2.4.3 Inverse Pole Figure Maps

Because electron backscatter diffraction has the spatial resolution to distinguish the orientations of different grains, it is possible to show the resulting microstructure map in terms of the orientation of each grain. A convenient way to do this is by color-coding each grain, according to a one-to-one unique correlation between crystallographic orientation indicated by a color with respect to a direction in the sample reference frame. The color reference will be noted on all IPF maps in this document, unless otherwise noted, the reference direction is the [001] sample direction.

## 2.5 Materials Overview

### 2.5.1 Yttria Structure

Yttria, or yttrium oxide ( $Y_2O_3$ ), is a cubic ceramic material. Its crystallographic structure has space group  $Ia\bar{3}$  (No. 206 in the International Tables of Crystallography), and has 80 atoms

in each cubic cell, as seen in Figure 2.10 a<sup>45</sup>. This isotropic cubic structure makes yttria an ideal system for grain boundary investigations. The cubic symmetry of this material leads to a fundamental zone of orientations (highlighted in Figure 2.10 b) that will be used for the two-parameter GBCD and inverse pole figures. In plots of the GBCD used in this thesis, the (111) orientation is in the upper right quadrant of the stereogram.

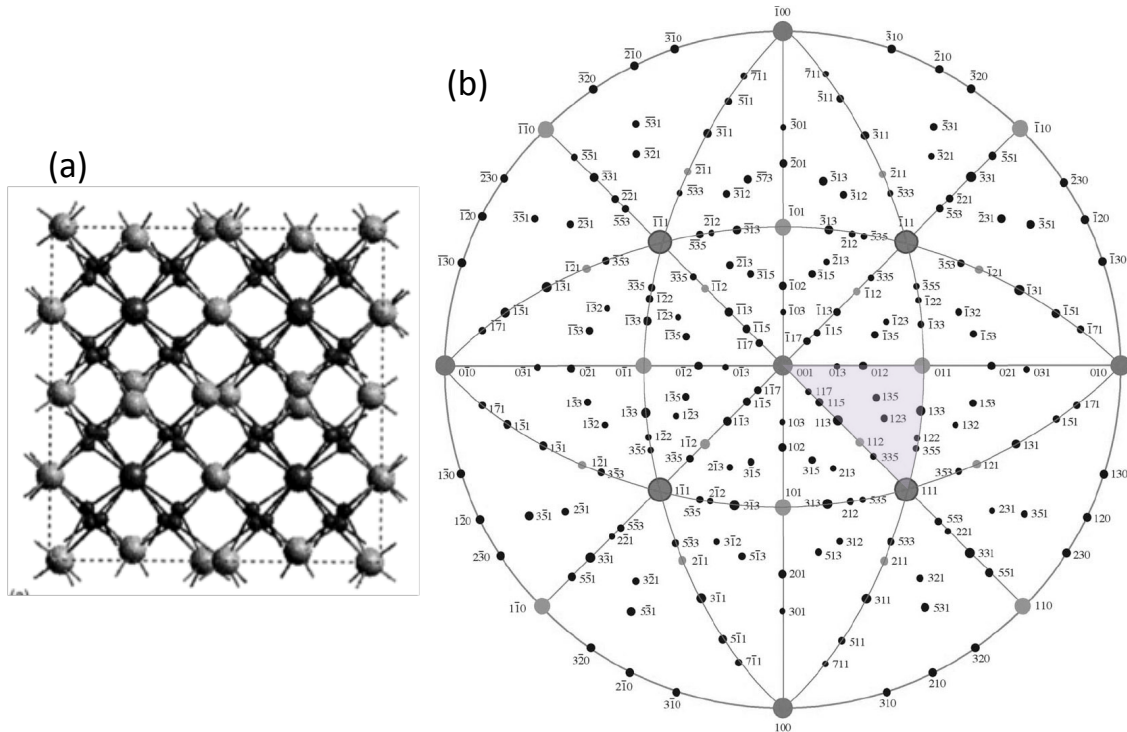


**Figure 2.10.** The yttria unit cell replicated from reference <sup>45</sup>(a) and a cubic [001] stereographic projection showing possible low index poles (b). The highlighted region represents the fundamental zone in both GBCD and TSL output.

Under the proper processing conditions, yttria exhibits a high melting temperature, high thermal conductivity, low thermal expansion, corrosion resistance, and large range of transparency<sup>46–49</sup>. Polycrystalline yttria can be used as a host ceramic for lasers and scintillators and for military applications such as infrared windows in heat seeking rockets<sup>50, 51</sup>. Another interesting property is that yttria is highly resistant to plasma etching, so work has been done to develop methods of fabricating dense, transparent, polycrystalline yttria coatings for the interior of plasma etching machines<sup>52, 53</sup>, there has also been particular interest in (111) textured coatings

for plasma resistance<sup>54</sup>. The desired results require precise microstructure control, which, with the assistance of grain growth inhibiting dopants, leads to complexion transitions and texture development that can significantly improve the properties of yttria coatings.

### 2.5.2 Alumina Structure

$\alpha$ -alumina ( $\text{Al}_2\text{O}_3$ ), which, when presented as a single crystal, is known as sapphire, has the corundum crystal structure. It is a member of the ditrigonal-scalenohedral class of trigonal symmetry  $D_{3d}^6 - R\bar{3}c$  (no. 167 in International Tables of Crystallography). Alumina has a centrosymmetric unit cell consisting of approximately hexagonally close packed  $\text{O}^{2-}$  anions with  $\text{Al}^{3+}$  cations filling two-thirds the octahedral sites, this can be seen in Figure 2.11 a. In all calculations, we assume that the space group simplifies to the symmetry operators of point group 32. Which is the rotation group of alumina's  $\bar{3}m$  Laue group<sup>55-57</sup>.

The trigonal  $\alpha$ -alumina structure can be represented either in a hexagonal or rhombohedral reference frame. Throughout this document, we will use the hexagonal reference frame. Miller-Bravais notation is used when referring to the planes and directions in alumina. When needed, the Miller-Bravais hexagonal reference frame (u v t w) can be converted to a Cartesian reference frame (x y z) using the following equations<sup>41</sup>:

$$\begin{aligned} x &= 1.5u \\ y &= \sqrt{3}\left(\frac{u}{2} + v\right) \\ z &= wc \end{aligned} \tag{2.12}$$

Table 2.1 shows common facets in the alumina system, including the Miller-Bravais indices, letter denotation, and common crystallographic plane name. These planes, as well as others, are also represented on the (0001) stereogram found in Figure 2.11b. To align this stereogram with the GBCD plots, the  $(2\bar{1}\bar{1}0)$  plane is aligned along the x-axis of the GBCD plot and the  $(01\bar{1}0)$

plane is along the y-axis. The fundamental zone for the GBCD plots is highlighted in blue, and the fundamental zone for the TSL software is highlighted in red. While the defined zones are different, the symmetry operators acting on the system assure that they are both accurate. These sample projections and knowledge of the plotting reference frames are extremely useful when attempting to index grain boundary plane orientations that occur in the grain boundary plane distributions.

Alumina is a highly stable, insulating material used for many applications. The applications most relevant to this project are the high temperature creep resistance and transparency. However, the low diffusivity and conductivity, high temperature stability, and corrosion resistant properties also make alumina an attractive material for defense, energy, and various technology sectors. With the majority of these properties, microstructure control is essential for consistent materials performance. For example, to fabricate a transparent alumina window – as a high strength replacement for glass - a dense, unimodal microstructure with a grain size in which the scattering centers are comparable to the wavelength of the incoming light is needed. Yttrium doping is known to slow down the sintering kinetics of alumina as well as increase the creep resistant properties of the bulk sample<sup>18, 58</sup>, this leads to a fine-grained creep resistant material – ideal for transparent ceramic manufacturing. However, the addition of yttrium and small traces of silicon to alumina also causes the nucleation of abnormal grain growth in the fine-grained microstructure when heated above 1500 °C<sup>59</sup>, a decrease in the creep resistance and density coincides with a second phase precipitation and nucleation of abnormal grains. Therefore, the addition of a co-dopant that maintains the same low temperature grain boundary structure and properties while deterring abnormal grain growth at high temperatures would be an ideal advancement in the field of transparent ceramic materials. A more extensive

background regarding the Y-doped alumina system can be found in Section 5.1 of this document. Chapter 5 of this document investigates the effect of various dopants on creep resistant alumina fabricated for transparent applications, while Chapter 6 and 7 focus on controlling the microstructure development.

**Table 2.1.** Common plane facets in alumina

Miller-Bravais	Letter denotation	Plane name
(0001)	c	Basal
$\{1\bar{2}10\}$	a	Prism
$\{10\bar{1}0\}$	m	Prism
$\{10\bar{1}1\}$	r	Rhombohedral
$\{01\bar{1}2\}$	R	Rhombohedral
$\{02\bar{2}1\}$	s	Sphenoidal
$\{11\bar{2}3\}$	p	Pyramidal

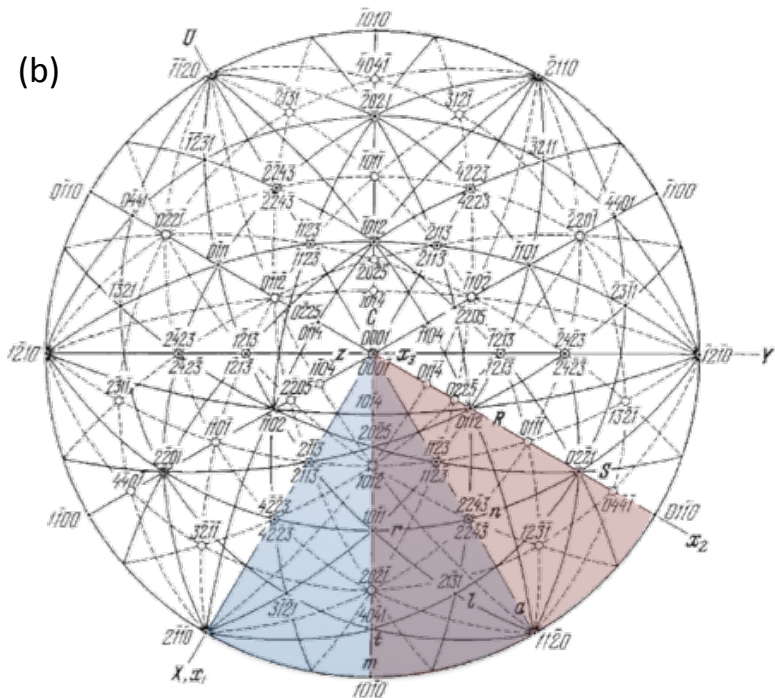
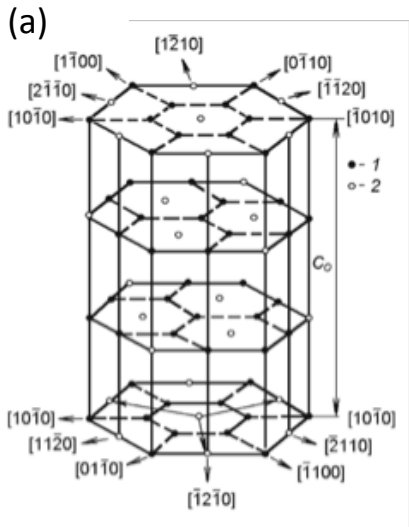


**Figure 2.11.** The alumina unit cell in a hexagonal reference frame (a) and the alumina (001) stereographic projection showing low index planes in Miller-Bravais notation (b) In the stereogram, the GBCD fundamental zone is highlighted in blue and the TSL fundamental zone is highlighted in red – they are symmetrically equivalent.

### 3. Methodology

The following summary attempts to present a clear description of exactly what methods were used for each experiment and analysis. This chapter is presented to give a primary background on what methods were used; specific experimental parameters will be presented in the relevant experiment sections. In some cases, sample preparation was performed by a colleague at another institution, in these cases a brief summary is given and further details can be found in corresponding references.

#### 3.1 Characterization Methods

##### 3.1.1 Electron Backscatter Diffraction

Electron backscatter diffraction is a scanning electron microscopy technique where backscattered electrons are detected by a phosphor screen. Both the microscope and detector are interfaced with a data collection and processing program that indexes the resulting backscatter pattern and determines the orientation of the crystal. In the current work, automated electron backscatter diffraction maps were collected using a TSL OIM data collection system interfaced with an FEI Quanta 200 environmental scanning electron microscope.

To generate an EBSD pattern, a well-polished specimen must be placed at a 60°-70° tilt angle in the SEM chamber. At this optimal tilt, the maximum number of electrons are backscattered, rather than absorbed or emitted as other signals<sup>60</sup>. Backscattered electrons are diffracted from the atomic planes and form a Kikuchi band pattern. The width of the bands is twice the Bragg angle ( $\theta_{hkl}$ ) and can thus be defined according to Bragg's Law:

$$\lambda = 2d_{hkl} \sin \theta_{hkl} \quad (3.1)$$

Where  $\lambda$  is the wavelength of the electrons, which is dependent on the accelerating voltage, and  $d_{hkl}$  is the interplanar spacing. Reflected and consequently reinforced backscattered electrons (BSEs) create the Kikuchi lines, inelastic BSEs generate the background noise.

Computationally, the Hough transform is applied to each pixel in the binned Kikuchi pattern:

$$\rho(\theta) = x \cos \theta + y \sin \theta \quad (3.2)$$

This process transforms each point to a line ( $\rho$ ) as a function of position (x,y) and angular offset ( $\theta$ ) where the intensity of that line corresponds to the intensity of the corresponding pixel. The result is that lines in the Kikuchi pattern appear as high intensity peaks in Hough space, these peaks are then compared to known diffraction data. Because of the lower symmetry of the trigonal alumina system analyzed in this thesis, the Hough parameters in the OIM data collection program were adjusted as such: an 85% fraction of  $\rho$  was analyzed, and a binned pattern size of 120 was used – this gave higher resolution indexing which resulted in higher confidence solutions for the orientation.

### 3.1.2 Atomic Force Microscopy

Contact mode atomic force microscopy, or AFM, is a type of scanning probe microscopy (SPM) in which a sharp tip mounted on a soft cantilever spring measures the topography of the sample. The tip is connected to a piezoelectric element in a feedback loop that precisely controls the deflection of the spring. The cantilever is held at a specific distance from the surface by a balance of attractive (such as Van Der Waals and capillary) forces and repulsive (electron repulsion) forces that act on the tip. Contact mode AFM can be measured in one of three ways: At a constant force, during which feedback piezoelectric motors keep the scanner at a constant force with a constant cantilever deflection. A constant height mode, where the piezoelectric

elements hold the scanner at a constant height and the cantilever deflection alone measures the topography. Or, or through contact error – which is a combination of both constant height and force, in which feedback error automatically adjusts to changes in the surface such as to measure both subtle and steep changes in topography<sup>61</sup>. In all cases, the topography is measured using the reflection of a laser off the back of the cantilever and onto a segmented photo detector, which measures the deviation of the cantilever from its set-point position. A feedback from the detector loops the signal and adjusts the z-height of the scanner using the piezoelectric element to maintain the set point deflection.

### **3.2 Powder Processing**

The following procedure was used only for the C/A-plane Y-doped alumina powders that were initially doped at Carnegie Mellon University and Spark Plasma Sintered (SPS) at Lehigh University. Processing details for the Ca-doped yttria powder used to make the samples discussed in Chapter 4 can be found in reference <sup>16</sup>, and Processing of the La/Y –doped alumina powders used to make the samples discussed in Chapter 5 can be found in Reference <sup>62</sup>.

Care was taken to assure minimal contact of loose ceramic powders with any metallic objects to avoid contamination. Additionally, all objects in contact with the free powder and single crystal interfaces were made of High density polyethylene (HDPE), polytetrafluoroethylene (PTFE) or high purity alumina and were further cleaned using the following cleaning process, with a 15 minute soak in each solution.

1. Aqua-regia (3 HCl: 1HNO<sub>3</sub>)
2. DI water
3. H<sub>2</sub>O<sub>2</sub>
4. DI water

5. Ethanol
6. Acetone
7. DI water

*Notes: The mixture of HCl and HNO<sub>3</sub> produces an exothermic reaction; do not store this solution in an airtight container without first neutralizing the solution and allowing it to cool. Also, be sure that all of the H<sub>2</sub>O<sub>2</sub> is removed from the cleaned surface before soaking in acetone – the combination of the two will form an explosive when dried.*

The yttrium doped alumina powder was prepared by mixing pure alumina powder (Puratronic, Alpha Aesar 99.995% pure, Ward Hill, MA) with 500 ppm Y(NO<sub>3</sub>)<sub>3</sub>•6H<sub>2</sub>O (Alpha Aesar, Ward Hill, MA). To do this, a 0.05 M solution of Y(NO<sub>3</sub>)<sub>3</sub>•6H<sub>2</sub>O was mixed in methanol, and a micropipette was used to transfer precise amounts of the doping element into the pure alumina. The powder suspension was then mixed with methanol and stirred on a hot plate to evaporate in a fume hood; this was done to assure mixing while minimizing environmental contamination. Sapphire single crystals were also purchased (MTI Corp, Richmond, CA) and were thoroughly cleaned as per the process above to avoid contamination.

The dry doped powders were then placed in a plastic bag and rolled with a marble rolling pin and board to break up agglomerates of powder, and loaded into a graphite paper-lined 1 cm graphite die. The sample was organized in the graphite die such that a small amount of Y-doped alumina powder was interfaced with the graphite plunger, the C-plane (0001) oriented sapphire was then laid parallel to the die and the polished side of the crystal was oriented upward. Y-doped alumina powder was then layered onto the C-plane sapphire and finally an A-plane {11 $\bar{2}$ 0} oriented sapphire single crystal was layered on top of the powder with the polish side facing

toward the powder, and topped with a small amount of powder, and a green body was pressed. The layout of the sample can be seen in Figure 3.1. The samples were then spark plasma sintered (Thermal Technologies, LLC, Santa Clara, CA) at Lehigh University, according to the following procedure: A ramp of 100 °C/min to 800 ° and 10 MPa for an initial calcination dwell of 45 minutes, this was followed by an additional 100 °C/min ramp to 1300 °C at 50 MPa for 30 minutes to sinter, and cool at 150 °C/min.

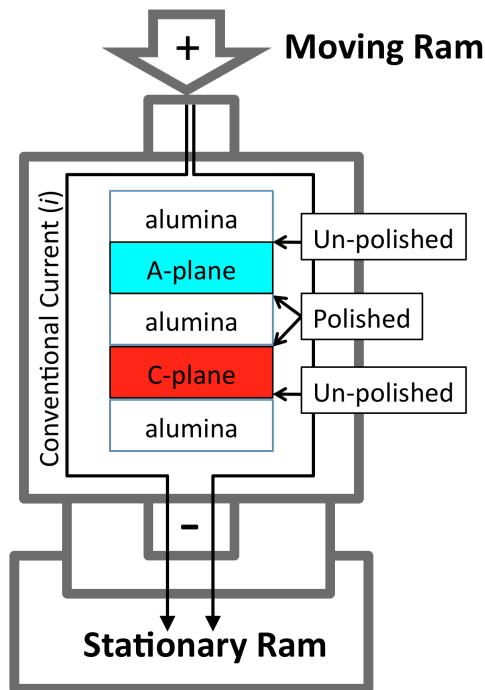


**Figure 3.1.** Schematic of the SPS graphite die holding the C/A-plane alumina sample, showing the current flowing from the moving ram/ positive electrode through the graphite die and to the stationary ram/negative electrode.

### 3.3 Forming Processes

Understanding the mechanisms of ceramic forming processes and their role on microstructural development leads to a better understanding of the material. The following explains the basics of the two main methods used to make the high-density samples analyzed in this document.

### 3.3.1 Hot Press

The Ca-doped yttria samples in Experiment I were hot pressed to form dense ceramic specimens. Hot pressing is a relatively straightforward and well-developed process in which samples are loaded into a die (in this case a graphite die) and uniaxially pressed while also being heated to a sintering temperature in a vacuum atmosphere. The drawbacks of this method are slow heating rates and long holding times, which make the development of fine-grained, transparent ceramics difficult.

### 3.3.2 Spark Plasma Sintering<sup>63-65</sup>

Spark Plasma Sintering (SPS) is a field assisted sintering method in which a uniaxial force is applied to, and direct electric current is pulsed through the sample while held at high vacuum. It is believed that the application of the current induces an electric field through the sample, this causes Joule heating at the contact points of the ceramic powders where sintering occurs. This leads to the ability to ramp at very fast heating rates and extremely short sintering times to form a dense, fine grained sample.

The effect that the electric field has on the sintering characteristics of ceramic powders is not completely understood. The current flows through the electrodes and graphite die, however it is not completely understood how the current interacts with an insulating ceramic. For polarized or highly ionic ceramics, for example, grain size gradients as well as pore or density gradients have been noticed along the electric field. In most cases with alumina the grain morphology and sintering characteristics do not seem to be effected by the electric field. There have, however, been accounts of doped alumina exhibiting higher conductivity when formed using SPS as opposed to non-field assisted sintering methods. Additionally, the sample geometry for the current experiments, which can be seen in Figure 3.1, has never been fabricated

using the SPS method, and there is some uncertainty as to if the field interaction with sapphire single crystals has any effect on the sintering behavior of these materials. Testing the field effect on single crystal morphology will be discussed in Chapter 8 of this document.

### 3.4 Sample Preparation

The pressed pellet was sectioned into smaller portions that were approximately 4 mm thick using a diamond wafering blade (Buehler 20 LC Diamond, Lake Bluff, IL). The edges of the sample that were in contact with the graphite paper were then ground down to remove carbon contamination. Any possible carbon that was diffused into the sample was on the exterior, un-analyzed, side of the single crystal.

The samples were then mounted in a quick setting acrylic (LECOSET 7007) and further polished according to the procedure seen in **Table 3.1**. All of the diamond suspensions were placed in an ultrasonic bath prior to use to avoid diamond agglomeration.

**Table 3.1.** Polishing procedure for dense alumina samples

Surface	Solution	Load (N)	Time (min)	Speed	Rotation
Ultraprep 45 $\mu\text{m}$ diamond	-	8	Until planar	240-300	>>
ApexHerculese H	9 $\mu\text{m}$ MetaDi Supreme Polycrystalline diamond	6	5	150-200	><
Verdutex	3 $\mu\text{m}$ MetaDi Supreme Polycrystalline diamond	6	5	120-180	>>
Verdutex	1 $\mu\text{m}$ MetaDi Supreme Polycrystalline diamond	6	5	100-150	><
Microfloc	0.05 $\mu\text{m}$ MetaDi Supreme Polycrystalline diamond	6	3	100-120	>>
		5	2	100-120	><

*Rotation arrows indicate direction of rotation of sample holder and base plate. This method was adapted from Beuhler's e-club technical information for polishing ceramics.*

The mounting acrylic was then dissolved in acetone and the samples were further cleaned to assure that the surface was free of contamination prior to thermal grooving. The surface cleaning procedure consists of the samples being placed in small glass vials and inserted into an

ultrasonic bath where they were soaked for thirty minutes each in: acetone, ethanol, and DI water. The final polished surface was then sprayed with ethanol and dried using pure nitrogen gas.

### **3.5 Heat Treatments**

#### **3.5.1 Annealing**

Small sections of the C/A plane Y-doped alumina sample were further annealed for set times between 1400° C and 1600° C in an open-air box furnace (Lindberg Blue M, Thermo Scientific Ashville, NC). The sample was held in a 98 % high alumina crucible (CoorsTek Inc., Golden, CO) with sacrificial alumina powder and the furnace was heated at a ramp rate of 10 °/minute.

#### **3.5.2 Thermal Grooving**

Generally, thermal grooving, also known as thermal etching, is conducted at a temperature about 100 °C below the lowest sintering temperature. However because of the already low temperature of the SPS forming process, it was not possible to initiate enough surface diffusion to form distinguishable grain boundary grooves at temperatures below or even at the 1300°C sintering temperature. Therefore the 8 hour annealed Y-doped alumina sample was grooved for 15 hours at 1400°C and the as SPS sample was grooved for 15 hours at 1350°C, both were grooved in an open-air box furnace (Lindberg Blue M, Thermo Scientific Ashville, NC). The grain boundary energies determined from grooves formed at 1350 °C and 1400 °C differed by 7.6%, as seen in Figure 3.2.

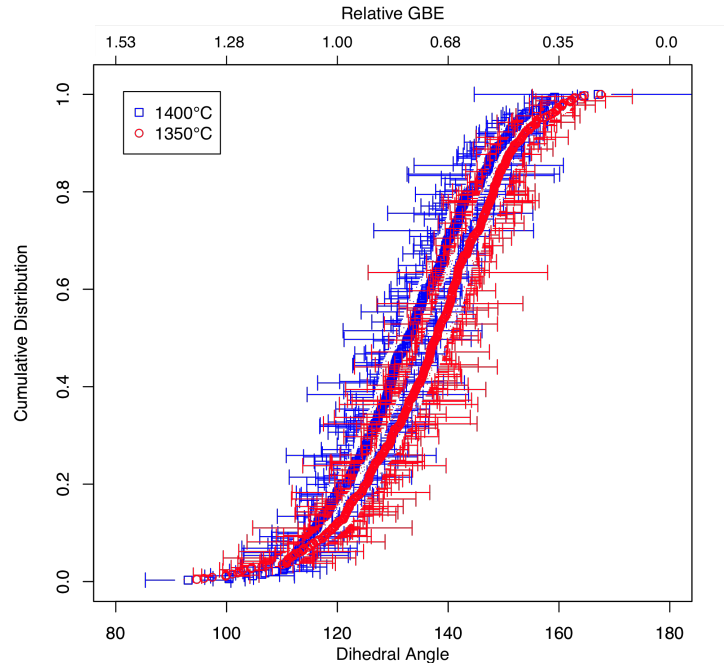


**Figure 3.2.** Full dihedral angle cumulative distribution of thermal groove temperature sensitivity measurements for grooves at 1400 °C (blue) and 1350 °C (red)

The extent of the error bar overlap and consistent distribution shape in Figure 3.2 imply that the relative grain boundary energy measurements would not greatly depend on grooving temperatures. This was the assumption for the measurements collected for the grain boundary energy results presented in Chapter 6 of this dissertation. The measurements presented in Chapter 8 imply that there may be a more significant relative grain boundary energy dependence on thermal grooving temperature in the presented 500 ppm Y-doped alumina sample – this conclusion was drawn after the experiment in Chapter 6 was completed. It is still believed that the comparison of the average energy measurements presented in Chapter 6 are accurate because two interfaces within the same sample - and thus grooved at the same temperature - were compared.

## **3.5 Grain Boundary Character Measurements**

### **3.5.1 EBSD Parameters**

EBSD was conducted on a Quanta 200 field emission microscope (FEI, Hillsboro, OR) interfaced with Orientation Imaging Microscopy (OIM version 5.21) Data Analysis system (EDAX, Mahwah, NJ). Post EBSD processing was done using TSL software (EDAX, Mahwah, NJ). For the Ca-doped yttria and La/Y-doped alumina GBCD analysis, an EBSD step size of 0.1 the average grain size was used to collect EBSD maps containing sufficient resolution for the plane analysis. In the Ca-doped yttria system, a minimum of 50,000 grain boundary line segments was needed for sufficient representation of all possible grain boundary planes for the five-parameter GBCD analysis. In the doped alumina systems, a total of 50,000 grain boundary line segments were needed for the two-dimensional GBCD analysis; however because of the low symmetry of the system a total of 300,000 line segments were needed for the complete five-dimensional GBCD analysis<sup>43</sup>.

### **3.5.2 Analysis Parameters**

The general rule for EBSD measurements intended for GBCD calculations is that the step size must be one tenth of the average grain size. Additionally, after grain boundary line segment extrapolation, there should be an average of about 5 steps per line segment to assure accuracy of the measurements. Specific experimental details of each analysis will be included in the corresponding sections.

## **3.6 Grain Boundary Energy Measurements**

### **3.6.1 AFM Parameters**

AFM measurements intended for grain boundary energy analysis were taken with either Budget Sensor ContAL-G tips (Contact mode, R-freq=13 kHz, Force constant=0.2 N/m) for the yttria experiment, or NanoWorld Pyrex-Nitride tips (Contact mode, R-freq=67 kHz, Force constant= 0.32 N/m) for the alumina experiments. Because of the wear resistance, Pyrex-Nitride tips are suggested for further analysis.

### **3.6.3 Groove measurements and Energy Calculations**

Topographic measurements were taken in contact mode on a Solver NEXT AFM (NT-MDT, Moscow, Russia). Each scan was collected with a 10 nm step size in both x and y, at 1 Hz scan frequency. The raw data was then opened, edited, and measurements taken in an open source program known as Gwyddion<sup>66</sup>. A plane level function was applied to flatten the data and, if needed, a match line correction was applied to eliminate AFM artifacts. However it must be mentioned that minimal editing was always preferred.

Line profiles were then hand drawn perpendicularly across a boundary. Three profiles were measured and averaged together to obtain an accurate representation of groove shape for each grain boundary. Representative AFM images and thermal groove profiles will be shown for each experiment in order to validate the assumption that surface diffusion formed the thermal grooves. The profile heights were then exported to a text file and further imported to a MatLab program that calculates the cumulative distributions of the relative grain boundary energy.

The relative grain boundary energy for bulk polycrystalline materials, such as those discussed in the Ca-doped yttria experiment in Chapter 4, were analyzed using Mullins' original full dihedral angle analysis. However, Mullins assumed that the surface energy of each grain

was isotropic, and Saylor's modifications allowed for isotropy as long as the grains were randomly oriented. In the case of a single crystal/ poly crystalline interface, such as in the samples discussed in Chapter 6, one side of the grain boundary is always the orientation of the sectioned surface of the single crystal. In that case, the grain boundary half-angle was analyzed, where the width of the groove ( $w$ ) was the horizontal distance from the minimum of the groove to the local maximum on the polycrystal side. This is discussed in more detail in Section 2.2.

## **4. Experiment I: Changes in grain boundary character and energy distributions resulting from a complexion transition in Ca-doped Yttria**

The following chapter discusses the changes in the grain boundary character and energy distributions in the Ca-doped yttria system before and after a complexion transition. This work was completed in collaboration with Lehigh University, and the results can be found mainly in reference <sup>14</sup>, with added data from reference <sup>21</sup>. The overarching goal of this experiment was to evaluate changes in the width of the grain boundary character distribution and the relative grain boundary energy distribution that result from a grain boundary complexion transition. In this case, the indicator of the complexion transition was abnormal grain growth. Also, for the first time, the aforementioned changes were measured in a non-alumina system. The results showed an increase in the width of the grain boundary character distribution and a decrease in the relative grain boundary energy when high mobility boundaries – indicative of a complexion transition - were compared to slow moving boundaries presumed to be of a different complexion. This project also provoked interesting questions about the use of abnormally large grains as the indicator for complexion transitions; the results indicate that in some circumstances, grain boundaries may transform to a new complexion if they are connected to a transformed boundary, while not bounding an abnormally large grain.

### **4.1 Motivation and Overview**

As discussed in Section 3, controlling the microstructural development to obtain a theoretically dense material has been the primary objective of research on yttria. Ma recently conducted a comprehensive investigation of the grain growth kinetics of dense Ca and Si doped-yttria in a reducing atmosphere. It was found that the 100 ppm Ca-doped yttria sintered at

temperatures above 1700 °C for six hours exhibited abnormal grain growth. Mobility measurements paired with HRTEM images classified the boundaries surrounding the largest or abnormal grains as an amorphous intergranular film. The boundaries around grains with normal sizes observed in 100 ppm Ca-doped yttria had a bilayer of segregated Ca<sup>16</sup>. Due to the different grain boundary structures, as well as lack of sufficient time and/or temperature steps, it is assumed that the method of obtaining a bimodal microstructure is through a complexion transition resulting in abnormal grain growth and not coarsening<sup>27</sup>.

The following work on 100ppm Ca-doped yttria system investigates the hypothesis that a complexion transition resulting in abnormal grain growth will reduce the relative grain boundary energy of the transformed boundaries. The transformed lower energy boundaries then increase in relative area, resulting in increased anisotropy of the grain boundary character. The results of this work provide further insight into both the tendency for a complexion transition to occur on specific crystallographic planes and/or misorientations as well as the grain boundary energy changes that accompany complexion transitions. This was the first time that a concurrent investigation of changes in the grain boundary character and energy distributions resulting from a complexion transition has been investigated in a non-alumina system.

## **4.2 Experimental Procedures**

A detailed description of the process used to produce the yttria samples can be found in reference<sup>16</sup>. Briefly, the samples used in the current study were hot pressed to obtain a near theoretical density and further annealed at 1700°C in a 5 % H<sub>2</sub>-N<sub>2</sub> atmosphere with two different dwell times. The “0 hour dwell” sample was fabricated by raising the furnace temperature to 1700°C and then immediately quenching. This sample had a normal grain size distribution and is referred to as NGG. The second sample was annealed at 1700 °C for 6 h and then quenched.

It had a bimodal or abnormal grain size distribution and is therefore referred to as the AGG sample. Kinetic and HRTEM analysis of the boundaries found an equivalent bilayer of Ca at the grain boundaries in the NGG sample (0 h dwell) and an intergranular film surrounding abnormally large grains in the AGG sample (6 h dwell). Kinetic analysis allowed for the assumption that the boundaries surrounding lower mobility grains in the AGG sample exhibited a bilayer of Ca segregation.

Automated EBSD mapping data was collected for both the NGG and AGG samples on a Quanta 200 Field Emission SEM with dedicated OIM EDAX Delphi software configured with TSL analysis (EDAX Inc, Mahwah, NJ). The EBSD step size for the NGG sample was 0.1  $\mu\text{m}$  on a hexagonal grid with an accelerating voltage of 10 kV. The AGG sample was imaged with a 1  $\mu\text{m}$  step size and an accelerating voltage of 20 kV, when the sample had a thin Ir coating, and 15 kV when the coating was removed. This coating was initially applied to eliminate charging, but was found to be unnecessary; there were no significant differences in the maps of samples with or without the coating. Both samples were imaged at a working distance of 15 mm.

The images were processed before extracting the line segments using the following steps. First, a single iteration grain dilation filter with a minimum grain size of five pixels and a tolerance of  $5^\circ$  was applied to each image. This changed 3.1% of the pixels in the AGG images and 7.6% of the pixels in the NGG images. Next, a single orientation was assigned to each grain, again with a tolerance of  $5^\circ$ . The grain boundaries were then approximated by a series of line segments with a deviation tolerance of two pixels. The process resulted in 68,116 line segments from the NGG sample and 130,087 line segments from the AGG sample. The GBCD was then calculated using open source programs that implement a stereological procedure for determining the GBCD<sup>67</sup>.

Thermal grooves were produced by heating the yttria samples in an air furnace (Lindberg furnace, Los Angeles, CA) for 30 min at 1300°C; the samples were heated to this temperature at 5 °C/min and cooled at 10 °C/min. Contact AFM topographs were recorded on these grooved samples using SolverNext NT-MDT AFM (NT-MDT, Zelenograd, Moscow) and Budget Sensor ContAL-G tips (Contact mode, R-freq=13 kHz, Force constant=0.2 N/m). The topographic images were taken with a step size of 10 nm and a 5 to 20 μm field of view. The AFM images were edited with the open source software Gwyddion<sup>66</sup>. The images were edited only if necessary. The two corrections that were sometimes applied were a plane level function to remove global tilts and, if needed, a match line correction to eliminate AFM artifacts. The dihedral angles were then determined from the widths and depths of the thermal groove, using the procedures described in Chapter 3.

Topographic data of lines perpendicular to grain boundaries were measured on both the NGG and AGG samples. For the NGG sample, all of the boundaries were considered equivalent. For the AGG sample, the boundaries were classified into three categories. Figure 4.1 shows an AFM image of the AGG sample and the corresponding topographic profiles across a boundary between a larger grain (labeled 1) and a smaller grain (labeled 2) and between two of the smaller grains (labeled 2 and 3). The boundaries surrounding larger grains, such as the one between grain 1 and 2, were designated as abnormal grain boundaries. The boundaries between two grains adjacent to the larger grains, such as the boundary between 2 and 3, were designated as normal grain boundaries adjacent to the abnormal grains. Grain boundaries between normal grains far from the area of abnormal grain growth were also measured. Over 200 boundaries were measured in each sample and for each one, three parallel topographic traces were extracted from the images. A text file of thermal groove profiles was extracted using Gwyddion<sup>66</sup>. A

program developed in house was then used to automatically determine the depth and width of the groove to calculate the dihedral angles, the relative energies, and the standard deviations of these quantities for each boundary. The accuracy of the program was verified by comparing its output to the values produced by a manual measurement of the same boundaries, this is found in Figure 4.2.

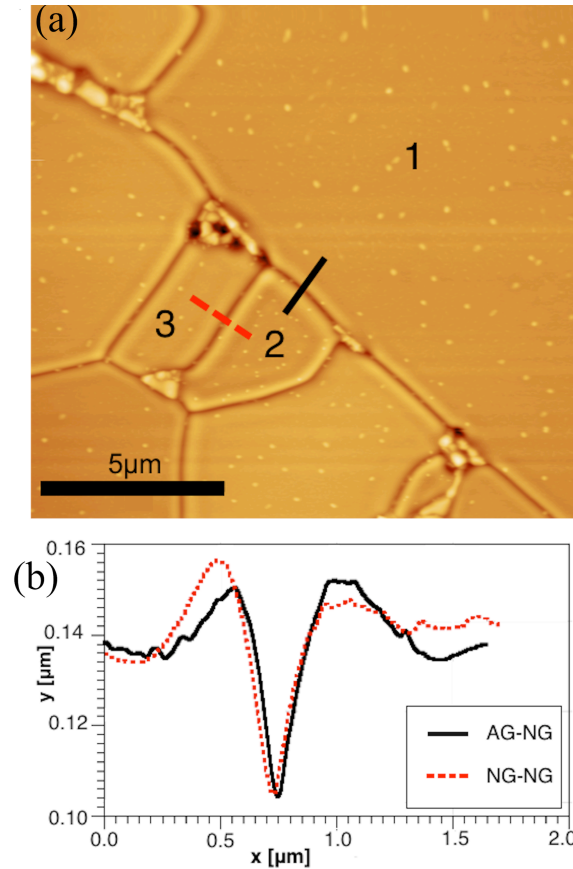


**Figure 4.1.** (a) Topographic AFM image of the thermally grooved AGG sample, where the solid line indicates the location from which the topographic data in (b) was extracted across a boundary surrounding an abnormal grain and the dashed line indicates the source of the data from the adjacent boundary that between normal grains. (b) The corresponding grain boundary topographs, the height of the boundary is on vertical-axis and width on horizontal-axis. The solid line corresponds to the solid line across the abnormal boundary scan line in (a). Similarly, the dashed line corresponds to the topographic data across a boundary between two smaller grains.

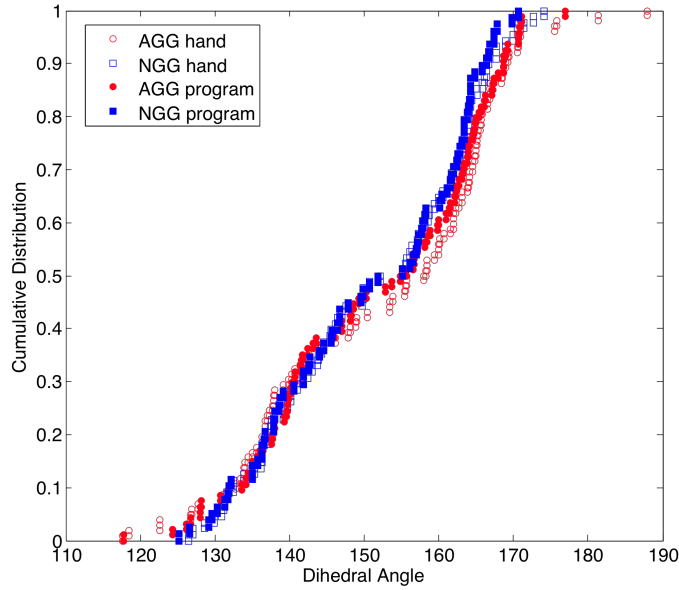


**Figure 4.2.** Cumulative distribution of a portion of dihedral angles for AGG and adjacent NGG boundaries, solid shapes are angles calculated using the automated method while the empty shapes are calculated by manually recording the width and depth of each groove. There is no distinguishable difference between the methods, verifying the accuracy of the automated process.

### 4.3. Results

Orientation maps were measured for both the AGG and NGG yttria samples. Over 50,000 grain boundary line segments were extracted from each data set, which is sufficient to represent all grain boundary possibilities at a resolution ( $\Delta$ ) of  $10^{-43}$ . Grain orientation maps from the EBSD measurements, with superimposed reconstructed grain boundaries from each sample, are shown in Figure 4.3. The grain orientation texture in each sample is further quantified by the [001] inverse pole figures in Figure 4.4.

The colors in the orientation map of the AGG sample indicates that the (111) orientation is predominately normal to the surface, while the NGG sample seems to have a more random distribution. The IPFs in Figure 4.4 are consistent with this observation, showing that the (111)//[001] is preferred, with a peak of approximately 3 MRD. The NGG sample does not have any peaks above about 1.5 MRD, consistent with the random coloring in the orientation map.

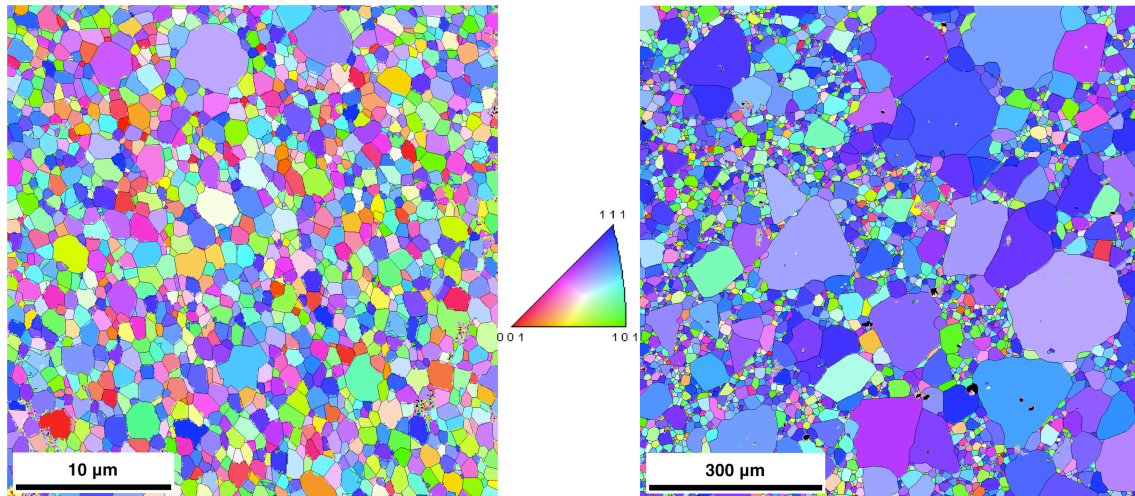


**Figure 4.3.** Inverse pole figure maps from EBSD data with superimposed reconstructed grain boundaries for (a) NGG sample, which exhibits a homogeneous grain size distribution, and (b) AGG sample, displaying a bimodal grain size distribution and an apparent change in texture.

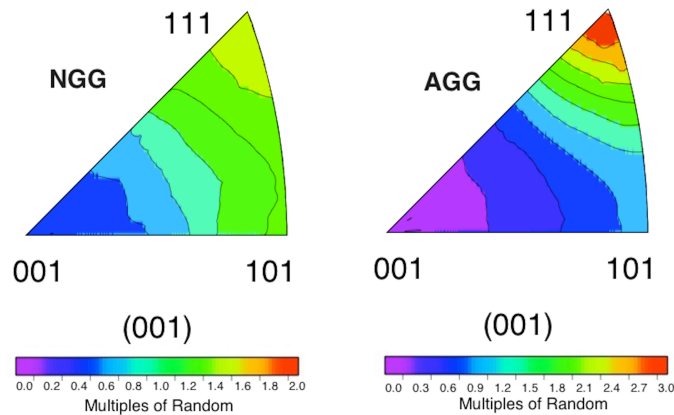


**Figure 4.4.** Inverse pole figures for the [001] sample reference direction. (a) The NGG sample lacks significant texture. (b) The AGG sample shows a preference for  $\{111\}$  orientations.

The grain boundary plane distributions of the NGG and AGG yttria samples, determined without consideration of the misorientation, are shown in Figure 4.5(a) and 4.5(b), respectively. The distributions are significantly different in the two samples. The NGG sample has a weak preference for  $\{111\}$  grain boundary planes, while the AGG sample favors  $\{001\}$  and is two times more anisotropic. It should be mentioned that the difference in texture could influence the calculated grain boundary plane distribution<sup>32</sup>. In particular, the result from the AGG sample will have some bias because of the non-random orientation distribution. However, the (111)

texture in the AGG sample would, if anything, lead to an overestimation of the population of (111) planes. Therefore, the observation that (100) planes are dominant is not an artifact of the texture.

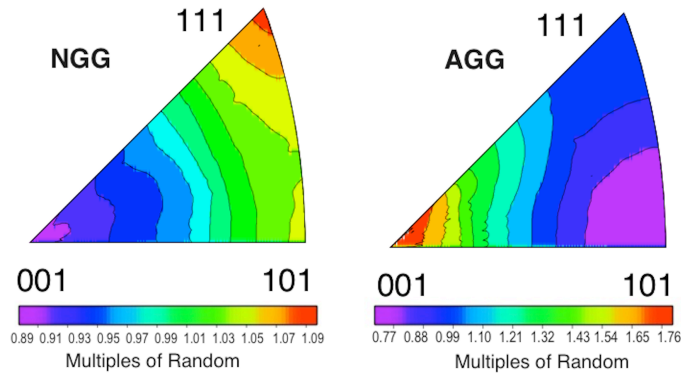


**Figure 4.5.** The grain boundary plane distributions, independent of misorientation, for the (a) NGG sample and (b) the AGG sample plotted in the standard stereographic triangle.

The stereographic projections in Figures 4.6 - 4.8 show the distributions of grain boundary planes at specific misorientations. The most notable peak in the distributions of both the NGG and AGG samples is the twist grain boundary at  $45^\circ/[100]$ , terminated by (100) and  $(\bar{1}00)$  planes. The maximum at the twist position is about 4 MRD for the NGG sample and 5.1 MRD in the AGG sample (see Figure 4.5). In the AGG sample,  $30^\circ/[110]$  shows a high population of (001) and  $(\bar{1}\bar{1}2)$  asymmetric tilt boundaries (see Figure 4.7). These grain boundaries are not highly populated at the same misorientation for the NGG sample. Additionally, the  $60^\circ/[111]$  NGG distribution shows a broad peak in the vicinity of the (111) twist boundary while the AGG distribution shows a shift in the distribution with high populations at all of the {001} and {111} planes (see Figure 4.8). All three of these misorientations show a significant change in the anisotropy of the grain boundary character between the NGG and AGG sample. Additionally, the occurrence of increased grain boundary populations at {100} orientations in the grain boundary plane distributions at specific misorientations for the AGG

samples is consistent with the shift from  $\{111\}$  to  $\{100\}$  in the two-parameter grain boundary plane distributions of the NGG and AGG samples (see Figure 4.5).

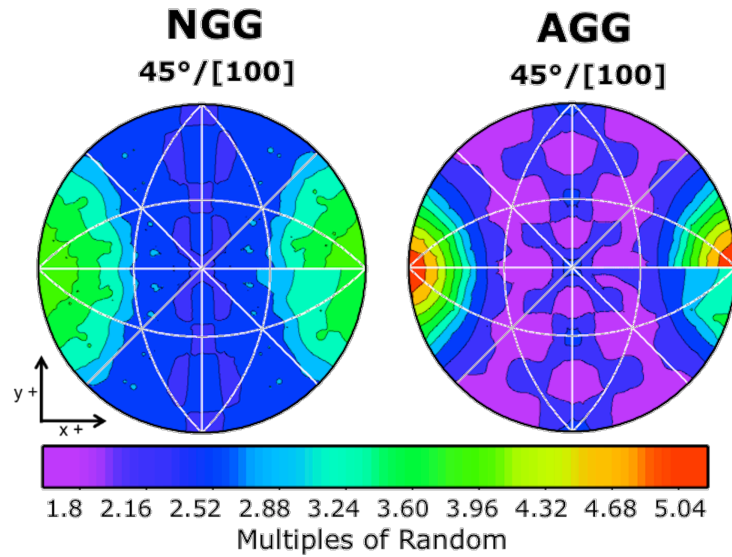


**Figure 4.6.** Grain boundary plane distributions for the misorientation of 45 ° around [100], plotted in stereographic projection, with the [100] direction orientated horizontally to the right and the [001] direction is normal to the figure. Subsequent figures are plotted in the same way. (a) NGG sample. (b) AGG sample.

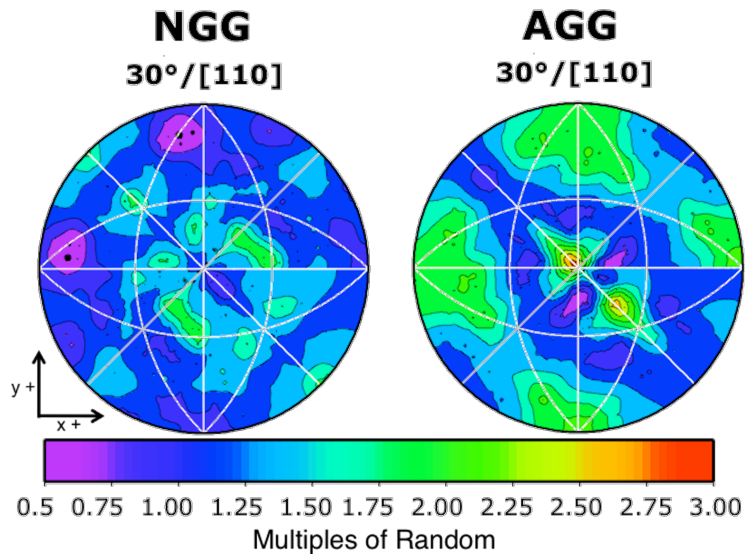


**Figure 4.7.** Grain boundary plane distributions for the misorientation of 30 ° around [110]. (a) NGG sample. (b) AGG sample.

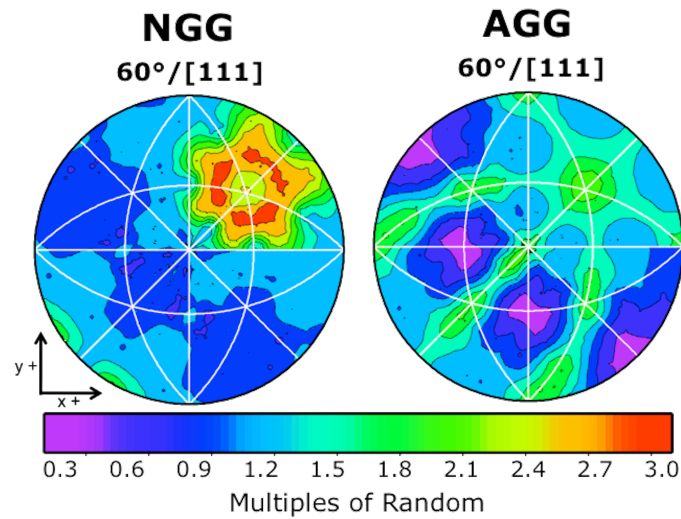


**Figure 4.8.** Grain boundary plane distributions for the misorientation of  $60^\circ$  around  $[111]$ . (a) NGG sample. (b) AGG sample.

AFM images were used to measure the topography of the grain boundary thermal grooves on both samples. Figure 4.1(a) shows an example of an AFM image and the corresponding topography along a single line that crosses the boundary between an abnormal and a normal grain, 1 and 2, and the adjacent boundary between two normal grains, 2 and 3. At first, the boundaries adjacent to the abnormal grains were the only normal grain growth boundaries analyzed in the AGG sample, this was done as an attempt to keep the local chemistry near the boundaries consistent. However, due to the initial grain boundary energy results, an area of normal grain growth at least ten grains away from the AGG region of the AGG sample was also analyzed. Similar topographic data was obtained for lines across boundaries with well-defined grooves in the NGG sample. Figure 4.1(b) shows an example of topographic data from the AGG sample that corresponds to the line profiles across the grain boundaries indicated on Figure 4.1(a). Representative AFM topographs of the three areas of grain growth that were analyzed can be seen in Figure 4.9. Where Fig 4.9(a) shows an example AFM topographic scans from the

NGG sample, Figure 4.9(b) shows the normal grain growth region of the AGG sample, and Fig 4.9(c) shows the abnormal and the adjacent normal grains.

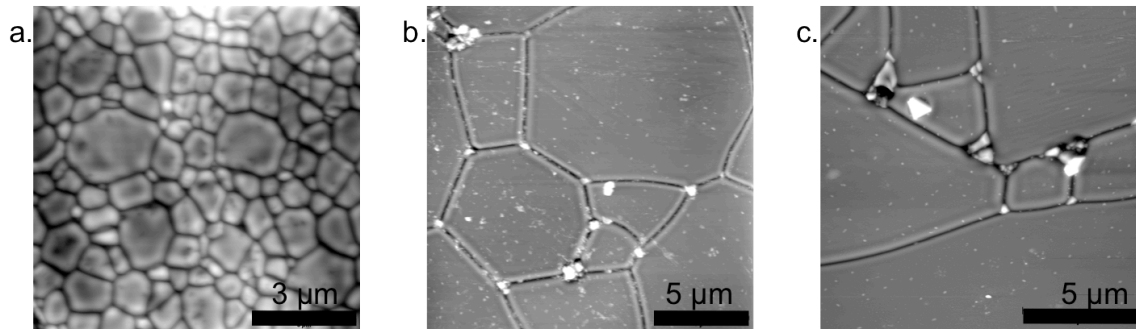


**Figure 4.9.** Topographic AFM images of the (a) NGG sample, (b) AGG sample far from abnormal grains, and (c) AGG sample with a section of a very large grain in the lower part of the field of view.

The cumulative distribution of the dihedral angles for the boundaries surrounding abnormal grains (AGG), boundaries between normal grains that were adjacent to the abnormal grains in the AGG sample (NG adj. AGG), boundaries in the normal grain growth region far from the abnormal grains in the AGG sample (NGG far AGG), and normal grain growth grain boundaries in the NGG sample (NGG) are shown in Figure 4.10. The average values of the dihedral angle and relative interfacial energy for each boundary type are tabulated in the inset. It was found that the NGG sample had an average relative interfacial energy of 0.42, the normal grain growth region in the AGG sample was slightly higher, at 0.47, but within uncertainty of the NGG energy measurement. The average relative interfacial energy for the boundaries surrounding abnormally large grains and adjacent boundaries between two normal or smaller grains in the AGG sample is 0.28, corresponding to a 33% reduction in energy between the NGG regions and boundaries surrounding and adjacent to abnormal grains.

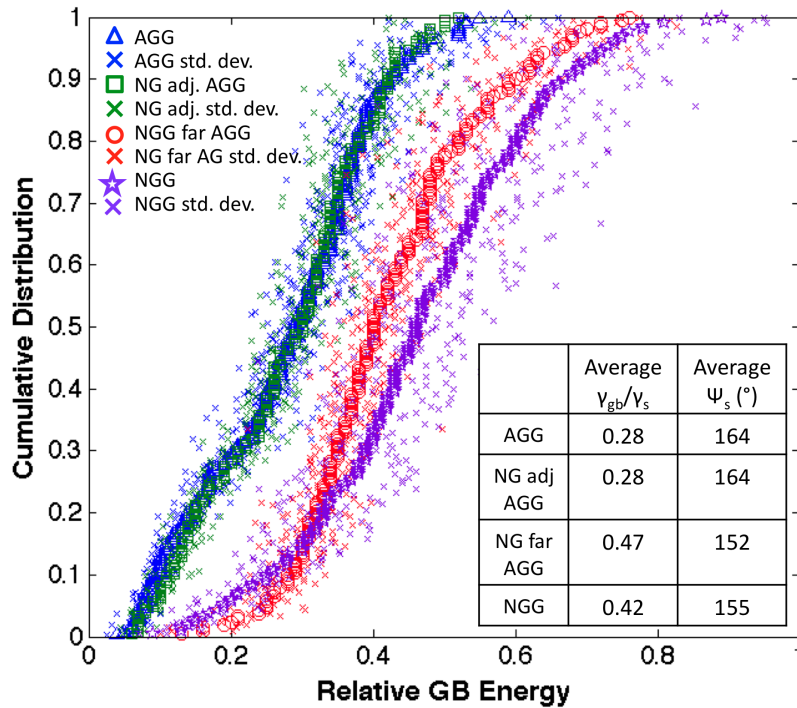


**Figure 4.10.** Cumulative distribution function comparing relative grain boundary energies for boundaries surrounding abnormally large grains (triangle), boundaries surrounding smaller grains that are adjacent to large grains in the AGG sample (square), boundaries surrounding smaller grains far from the large grains in the AGG sample (circle), and mean boundary energy for all boundaries in NGG sample (star).

## 4.4 Discussion

### 4.4.1 Grain Boundary Character

The five parameter GBCD of 100 ppm Ca-doped yttria can be compared to previous measurements of the GBCD of undoped yttria reported by Dillon and Rohrer<sup>68</sup>. Of the two samples considered here, the GBCD of the NGG sample was most similar to that of the undoped sample. However, one significant difference between the two distributions was found at the  $45^\circ/[100]$  misorientation. For the 100 ppm Ca-doped samples, the twist boundary at this misorientation is the maximum of the distribution (see Figure 5b), while it was a minimum in the undoped sample. In the past, impurities have been shown to influence grain boundary plane

distributions<sup>69</sup> and in this case, the higher population of the {100} type planes for the 45°/[100] twist boundaries could be caused by the Ca impurities. Additionally, the change from a preference for {111} planes in the grain boundary plane distribution of the NGG sample (Figure 4.4a) to {001} for the AGG sample (Figure 4.4b) is consistent with the stabilization of {001} planes by Ca. The preference for a specific grain boundary plane orientation caused by the addition of segregating impurities is one of the causes of the observed increase in GBCD anisotropy.

The results show that there are significant differences in the GBCD of the NGG and AGG sample. This is consistent with results from several doped aluminas reported by Dillon et al.<sup>5</sup>, which showed that complexion transitions altered the two-parameter grain boundary plane distributions. Analogous to the present study, the change in the grain boundary plane distribution was accompanied by an increase in the anisotropy of the distribution. In the present work, the samples differ only in the amount of time that they were annealed at 1700 °C and the changes in the GBCD are also attributed to a complexion transition. Based on the work of Ma et al.<sup>16</sup>, who studied the same Ca-doped yttria samples, the slower moving grain boundaries have a bilayer of Ca and the faster moving boundaries have an intergranular film. It is assumed that all of the boundaries in the NGG sample have the bilayer complexion and, in the AGG sample, the boundaries around the largest grains have the intergranular film and the boundaries around the smaller grains have the bilayer complexion. The co-existence of two grain boundary complexions resulted in the abnormal grain growth in the AGG sample. It has been established by studies of other systems that the GBCD is inversely correlated to the grain boundary energy distribution<sup>70</sup>. Therefore, the changes in the GBCD observed here are presumably associated

with changes in the grain boundary energy that are correlated with the complexion transition. This idea is supported by the results of the thermal groove analysis.

#### **4.4.2 Grain Boundary Energy**

The results in Figure 4.10 clearly show that the grain boundaries around the very large grains and around grains adjacent to the large grains have indistinguishable energies that are lower than the others. Furthermore, the grain boundaries around small grains that are distant from the large grains but still in the AGG sample have a similar higher mean energy as the sample that does not exhibit abnormal grain growth (the NGG sample). The interpretation is that both the grain boundaries around the large grains and the grains nearby have undergone a complexion transition and have an intergranular film at the boundary. The other small grains that are removed from the AGG have a bilayer of Ca and, therefore, a different complexion. It should also be noted that the width of the relative energy distribution is larger for the grains with the intergranular film. This is consistent with earlier results from doped aluminas, which showed both an increase in anisotropy and a reduction in the relative boundary energy resulting from a complexion transition<sup>6</sup>.

It should be noted that the dihedral angles between abnormal and adjacent normal grain boundaries, such as those seen in Figures 4.1 a and 4.9 c indicate that the adjacent normal grain boundary is very low in energy while the abnormal boundary energies are expected to be much higher than the normal. The inclination of these boundary planes has not been accounted for, and thus this dihedral angle measurement is not a true representation of what occurs in the three-dimensional microstructure. Additionally the torque terms, which have been ignored in the groove dihedral angle analysis<sup>37</sup> cannot be ignored when analyzing the dihedral angles at the grain boundary triple junction, especially in the case of highly faceted grains<sup>71</sup>. Overall, the use

of boundary triple junction dihedral angle analysis for these measurements would yield inconclusive results.

In the previous work<sup>6</sup>, when the energies of boundaries around large grains were compared to the energies of boundaries around small, but adjacent grains, it was not always possible to detect a difference. One possible explanation that was suggested is that because the energy measurements are made long after the complexion transition had occurred, they do not necessarily reflect the energy at the time of the transition. Here, we propose a different explanation. The transformation of the boundary complexion occurs preferentially in boundaries connected to those that have already transformed. However, because the prior grain has a large size advantage, it rapidly annihilates the newly transformed boundary as it grows. If the complexion transition propagated faster than the growing grains, then all grains would eventually have high mobility boundaries. However, because the boundaries around the distant grains remain in a higher energy state, the rate of propagation must be low.

These observations provide a possible explanation for the earlier results in doped aluminas where the largest grains and the neighboring grains had the same energy. It is possible that if grains further away were probed, a decrease in energy would have been detected. It is also important to recognize that in most cases, the smaller adjacent grains did have measurably higher energies, indicated that propagation of the complexion transition beyond the first boundary does not occur in all cases. All of the experiments where the boundaries surrounding abnormally large grains and those surrounding small grains that were adjacent to the abnormal grains had the same energy were also cases where the large grain had a complexion that involved an intergranular film. It may be that this complexion is easier to propagate than those involving ordered multilayer adsorption.

### 4.4.3 Texture analysis

As a final point, the colors in the orientation map of the AGG sample, seen in Figure 4.3, indicates that the (111) orientation is predominately normal to the surface, while the NGG sample seems to have a more random distribution. The IPFs in Figure 4.4 are consistent with this observation, showing that the (111)//[001] is preferred, with a peak of approximately 3 MRD. The NGG sample does not have any peaks above about 1.5 MRD, consistent with the random coloring in the orientation map.

It should be noted that after annealing the surface layer was removed by polishing so the large grains visible in the images could not have benefitted from a surface energy advantage. In previous studies of alumina, no changes in texture were associated with complexion transitions and the mechanism by which texture increases is not obvious here. However, it is not unusual for hot pressing to create texture and this is likely the source of the (111)//[001] texture in the AGG sample. Because the texture is mostly associated with the larger crystals whose surrounding boundaries transformed to the higher mobility complexion at an earlier time, one may speculate that non-uniform residual stresses induced by the hot pressing may promote the nucleation of complexion transitions on grains of a specific orientation. If that were the case, it would provide a new mechanism for the control of interface kinetics and microstructure development.

## 4.5 Conclusions

Ca-doped yttria samples of the same composition, sintered at the same temperature but held for different times, have significantly different grain boundary character distributions and mean grain boundary energies. Abnormal grain growth at longer annealing times initiated a clear shift in the population of grain boundary planes from a weak {111} preference to a stronger

{001} preference. This indicates that the complexion transitions influence the relative interfacial energies. The AFM thermal groove analysis showed that the grain boundaries in the 6 hour sample near the abnormal grain growth had energies that were, on average, 33% lower than in the sample without abnormal grain growth or in areas of the AGG sample far from the abnormal grains. The complexion transition leading to abnormal grain growth may be attributed to this reduction in energy. The results presented here are consistent with the idea that the complexion transition altered the grain boundary energy anisotropy and this led to a change in the mesoscale grain boundary character distribution.

## **5. Experiment II: Influence of Y and La Additions on Grain Growth and the Grain Boundary Character Distribution of Alumina**

The following section is part of a larger collaborative work between Carnegie Mellon University, EPFL, and the University of Stockholm, in which dopant elements and SPS sintering conditions were evaluated with the goal of better understanding the effects of these parameters on microstructural development in alumina. The overarching goal of this study was to fabricate transparent alumina. The findings and conclusions in this chapter have already been published (reference <sup>72</sup>) and are a result of the work done by the authors at Carnegie Mellon University to determine the effects of processing conditions and various dopants on the grain boundary character of opaque samples from the sintering study.

### **5.1 Introduction**

Yttrium and Lanthanum doping have been shown to significantly increase the creep resistance of polycrystalline alumina<sup>23–25, 58, 73</sup>. Y-doping decreases the creep rate of alumina by a factor of two and is more effective than La-doping<sup>24</sup>. In both cases, it is known that the dopant cation strongly segregates to the grain boundaries without forming an amorphous intergranular film<sup>19, 74</sup>. It is believed that the creep resistance is related to this segregation, but the mechanisms are still not fully understood. In the past, this “Y-effect” has been attributed to changes in grain boundary diffusivity, solute drag, second phase precipitation, and cation effects on dislocation motion and resistance to grain boundary sliding<sup>18</sup>. However, the most well supported work in this field shows that a change in the bonding character between the adsorbed Y atoms and the bulk lattice is the most likely cause of these enhanced properties<sup>23, 75, 76</sup>. It has also been shown that grain boundary sliding rates depend on the grain boundary plane orientation, at least for  $\Sigma 7$

grain boundaries<sup>73</sup>. Therefore, both the grain boundary chemistry and the orientation of the grain boundary plane may influence creep resistance.

In some investigations, abnormal grain growth leading to a bimodal grain size distribution has been seen in the Y-doped alumina samples. It has been shown that ultra-pure highly dense Y-doped alumina does not exhibit this abnormal growth<sup>77</sup>. However, when these samples were exposed to Si, whether intentionally doped or contaminated by the processing environment, large equiaxed grains grew abnormally fast<sup>59</sup>. The addition of Si alone has been shown to result in abnormal grain growth at much higher temperatures, so it can be suggested that both Si and Y play a role in the initiation of AGG. One study on the grain boundaries in Y-doped alumina has shown that the boundaries surrounding abnormally large grains have a larger amount of Si compared boundaries around normal grains in the same system, where the total amount of adsorbents is equivalent to roughly a monolayer – as compared to smaller concentrations at boundaries surrounding smaller grains.<sup>59</sup> However, the overall literature-based analysis on the concentration and structure of grain boundaries in the Y-doped alumina is largely inconclusive<sup>17, 18, 59, 78–80</sup>. The amount of Y segregated to alumina grain boundaries has been shown to be proportional to the bulk concentration of Y, up to a specific “super saturation” point, beyond which YAG precipitates are formed that exist in equilibrium with a lower Y concentration<sup>79, 81</sup>. In light of more recent developments in the field of grain boundary kinetics, it is likely that the Y (Si)-doped alumina system displays a grain boundary complexion transition that results in increased grain boundary mobility and AGG.

On the mesoscale, both lanthanum and yttrium doping in alumina have been shown to enhance densification and decrease grain growth of alumina<sup>77, 82</sup>. However, in Y-doped alumina sintered above 1550°C, the densification rate decreases and the rate of coarsening increases<sup>77</sup>. In

other systems, a change in sintering properties as a function of dopants and thermodynamic variables such as temperature can be attributed to a change in grain boundary complexion<sup>7, 29</sup>. One point of particular interest is the complexion transition that has been reported to occur in Y-doped alumina<sup>1</sup>. As a result of the transition, the grain boundary mobility increases and the relative grain boundary energy decreases by 46 %<sup>6</sup>. In this work, we will describe the changes in the grain boundary character distribution that accompany this transition.

The lowest energy interfaces for undoped alumina have been reported to be either (0001) or  $\{1\bar{1}02\}$  planes<sup>5, 83, 84</sup>. However, it is expected that the addition of an impurity will change the bonding structure at the boundary thus changing the preferred grain boundary plane. It should also be noted that the Wulff shape of a material does not directly correlate with the Wulff shape of a bi-crystal<sup>85</sup>.

There have been many sub-nanometer investigations of the grain boundaries in doped aluminas. The limited numbers of boundaries analyzed in each study usually had a special (high symmetry) geometry, so they are not necessarily representative of the bulk of the microstructure<sup>17-19, 23, 25</sup>. There have also been mesoscale studies of similarly doped aluminas by EBSD in which the misorientation angle distributions from many grain boundaries were analyzed<sup>81, 86</sup>. However, such analysis does not reveal information about the grain boundary plane distribution. The purpose of this chapter is to determine and compare the complete grain boundary character distributions, including the grain boundary plane distributions, in La- and Y-doped alumina. The results show how the dopants influence the grain boundary populations in alumina, presumably through their influence on the grain boundary energy.

Previous work by Stuer et al.<sup>62</sup> investigated the effect of processing variables on the SPS of Mg, Y, and La-doped alumina. While Stuer's work concentrated on the transparency of fine-

grained doped alumina, the current work investigates the grain boundary character of larger-grained opaque samples and focuses more on understanding the effect that Y and La have on the GBCD at different sintering temperatures.

## **5.2 Experimental Procedure**

### **5.2.1 Sample preparation <sup>1</sup>**

Dense polycrystalline pellets of Y and La-doped alumina at a doping level of 450 ppm and Y+La co-doped alumina at a total doping level of 450 ppm were prepared with an ultra pure  $\alpha$ -alumina powder (AA04, Sumitomo, Tokyo, Japan) and pulsed electric current sintering (PECS), also commonly referred to as spark plasma sintering. The powder preparation and SPS procedures are described in detail elsewhere <sup>62</sup>. For this work, the Y, La, and Y+La-doped samples were sintered at 1450 °C, 1500 °C and 1600 °C with a heating rate of 100 °C/min and dwell times and sintering pressures as summarized in Table 5.1. The resulting sample pieces were then polished by a series of diamond lapping films down to a surface roughness of 1  $\mu$ m, with a subsequent final polishing step using an oxide polishing solution (OPS) of silica to form the mirror-like surface needed for EBSD measurements. Note that all of the sintered samples were sufficiently dense to show transparency or translucency depending on their grain sizes <sup>87</sup>. The changes in the sintering pressures and dwell times served the purpose of promoting grain growth and/or rendering the grain sizes comparable among the samples.

### **5.2.2 Microstructure characterization by EBSD**

EBSD maps were collected for 450 ppm La-doped alumina sintered at 1500 °C and 1600 °C, 450 ppm Y-doped alumina sintered at 1450 °C, 1500 °C, and 1600 °C, and 450 ppm La and Y co-doped alumina sintered at 1500 °C and 1600 °C. The step size for each EBSD map, listed in

---

<sup>1</sup> This Section was written by M. Stuer

Table 5.2, was one-tenth the average grain size, such that the average length of the grain boundary line segments was greater than four steps per line segment. Each map was cleaned up in the TSL software<sup>88</sup> to remove unindexed points using a single iteration grain dilation with a minimum grain size of three to five pixels/grain and a tolerance angle of 5°. The resulting grains were then assigned a single average orientation. Multiple grains in each scan had assigned orientations that were influenced by the so-called “pseudo-symmetry” problem, where the EBSD pattern recognition software could not distinguish between two similar orientations separated by particular rotations about symmetry axes, resulting in a low average confidence for the affected areas. This causes many false grain boundaries, obvious in orientation maps such as the one shown in Figure 5.1(a), that influence the misorientation distributions.

**Table 5.1.** Summary of processing parameters used in the sample preparation.

<b>Dopants</b>	<b>Sintering Temperature [°C]</b>	<b>Sintering Pressure [MPa]</b>	<b>Dwell time [min]</b>
Y	1450	100	1
Y	1500	100	3
Y	1600	100	3
La	1450	100	1
La	1500	50	3
La	1600	50	3
Y+La	1450	100	2
Y+La	1500	50	3
Y+La	1600	50	3

**Table 5.2.** EBSD clean-up parameters and results

<b>Dopant (ppm)</b>	<b>SPS Temp. (°C)</b>	<b>Step Size (µm)</b>	<b>Cleanup* (%)</b>	<b>Steps/Segment**</b>	<b>Line Count**</b>
Y	1450	0.09	12.5	7.3	44,818
Y	1500	0.2	9.1	6.9	238,968
Y	1600	1.3	6.9	8.5	49,420
La	1500	0.5	10.0	6.7	325,425
La	1600	1.5	9.6	4.9	60,476

Y+LA	1500	1.4	5.2	7.0	62,314
Y+La	1600	2.3	9.5	5.7	43,305

\* Percent of data changed was before the CI standardization and corresponding partition

\*\* Steps/segment and line count collected after pseudo-symmetry cleanup

In the present case, the false boundaries were mostly 30° or 60° rotations about [0001]. To remove the orientations introduced by pseudo-symmetry, a grain confidence index (CI) standardization was applied, and an average CI partition was set, where the minimum grain size is two pixels, the minimum CI is 0.4, and the partition is set to only show grains with a CI greater than 0.4. This partition depends on scan quality, so poorer quality scans require a lower confidence index partition. By careful inspection of many orientation maps, it was ascertained that this procedure removes all false boundaries as well as areas obscured by contamination, leaving only true grain boundaries to be analyzed.

It should be noted that the built-in pseudo-symmetry clean-up method in the TSL software removes all boundaries according to a misorientation criterion. When implemented here, it removed not only those introduced by the pseudo-symmetry problem, but also true boundaries with the same misorientation, producing gaps in the misorientation distribution at these angles. It was also attempted to remove the false boundaries using geometric filters such as a minimum grain boundary segment length criterion, increasing the minimum grain size to 20 pixels, and analysis of the tortuosity and connectivity of grain boundary segments. However, none of these methods removed only the false boundaries introduced by the pseudo-symmetry problem.

Figure 5.1 illustrates both the effects of pseudo-symmetry on grain boundary maps for a representative microstructure, the misorientation distribution, and the grain boundary plane distribution, as well as its removal using the CI partition method described above. In the grain boundary map in Figure 5.1(a), boundaries with misorientations of 30°, 60°, and 75° around [0001] are colored blue, red, and green, respectively. Most of the boundaries are clearly part of

the true grain boundary network. However, boundaries that result from the pseudo-symmetry effect are also found in tortuous paths within apparent grains (see area marked by arrow). Such boundaries always have one of the special misorientations and can create peaks in the distribution of grain boundaries as a function of misorientation angle (Figure 5.1(b)). After the pseudo-symmetry clean-up procedure described above, the false boundaries in Figure 5.1(a) are removed and the real boundaries are preserved (see Figure 5.1(d)). Furthermore, when the misorientation distribution is recalculated (see Figure 5.1(e)), the artificial peaks produced by the false boundaries are no longer found. Note that because of the random orientations of the false pseudo-symmetry boundary planes, the grain boundary plane distributions (Figure 5.1(c) and (f)) are not significantly influenced.

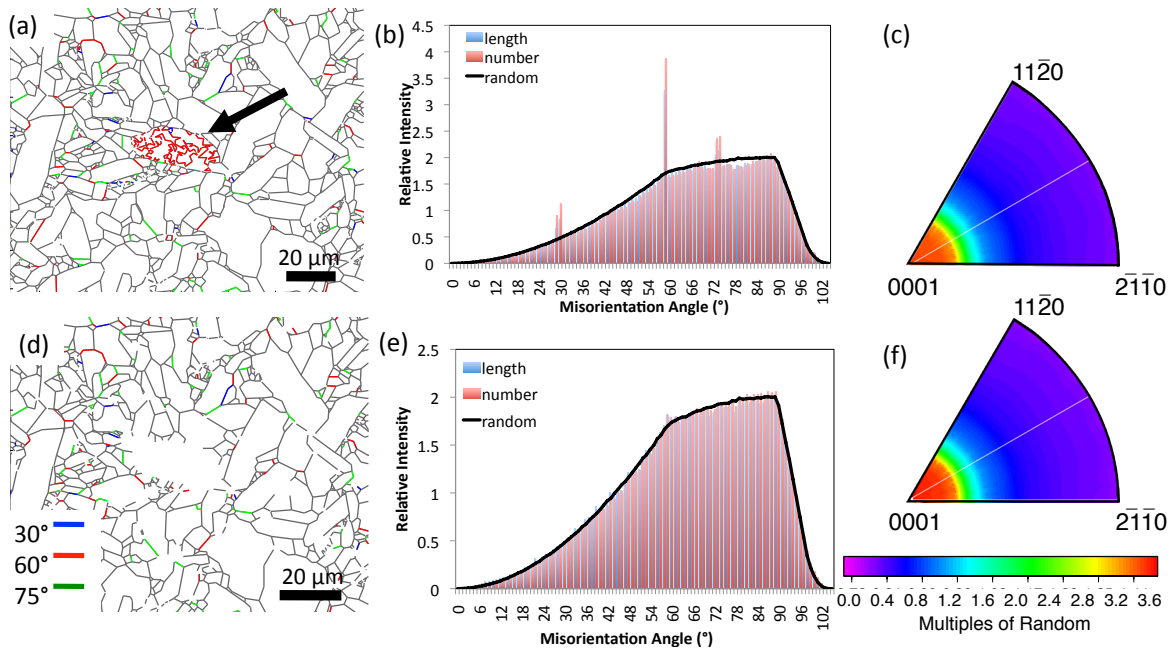


**Figure 5.1.** Effect of pseudo-symmetry on grain boundary distributions in La-doped alumina sintered at 1500°C. Reconstructed line segments before clean up where red/blue/green lines show pseudo-symmetry orientations (a), the corresponding one-dimensional misorientation distribution where the red bars are binned by grain boundary line count, the blue bars represent line length weighted distributions, and the black line represents a simulated random distribution (b) and grain boundary plane distribution in the crystal reference frame (c). Post clean-up line segment reconstruction showing removed pseudo-symmetry (d), the corresponding misorientation distribution (e), and plane distributions (f).

After the clean up, the grain boundary line segments were extracted using the TSL software. The acquisition of several hundred thousand grain boundary line segments for the 450 ppm Y-doped and 450 ppm La-doped aluminas sintered at 1500 °C made it possible to calculate the five parameter grain boundary character distributions at misorientations where the population is higher than random. For the other samples, only the distribution of grain boundary planes in the crystal reference frame, independent of misorientation, was calculated. The GBCD calculations, which use the stereological relationship between line length per area and area per volume, were carried out using a modified version of `calc_gbcd_stereo`<sup>42, 67</sup>. The program discretizes the grain boundary parameters and, in the original version of the program that was used in previous studies, the domain of Euler angles was limited to angles between zero and 90 °. This is acceptable for higher-symmetry materials, but is a fraction of a single fundamental zone for trigonal materials. To accommodate the trigonal symmetry, we used a domain that contains the full range of possible Euler angles, discretized into bins approximately 10 ° wide. In the calculations, we used the symmetry operators of point group 32, because this is the rotation group of alumina's  $\bar{3}m$  Laue group.

### 5.3 Results

Figures 5.2-5.4 show representative grain orientation maps for all seven samples. From these maps, it is possible to comment on the effect of sintering time and dopant on the microstructural development of alumina. La-doped alumina sintered at 1500 °C shows a high aspect ratio grain morphology and normal grain growth, as seen in Figure 5.2(a). Figure 5.2(b) shows La-doped alumina sintered at 1600°C, exhibiting the same elongated grain growth and a larger, yet still unimodal, grain size.

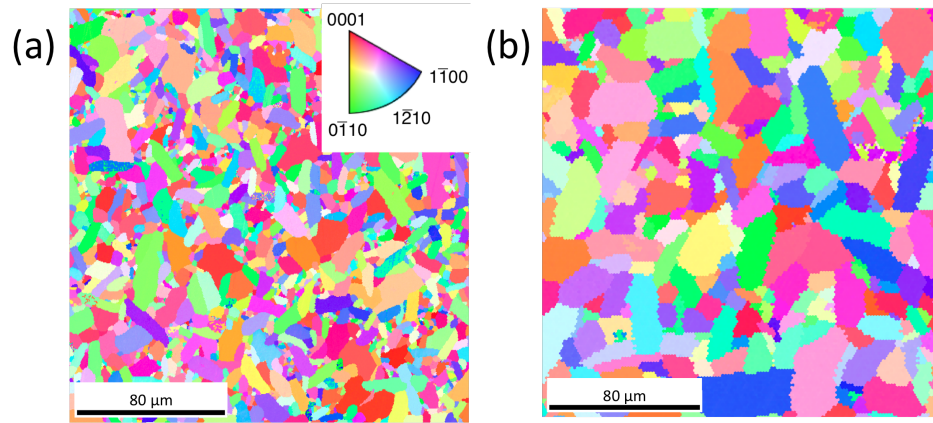


**Figure 5.2.** Orientation maps of 450 ppm La-doped alumina (a) SPS temperature 1500 °C and (b) SPS temperature of 1600 °C. Images from before pseudo-symmetry clean up.

Y-doped alumina sintered at 1450 °C displayed an equiaxed grain morphology and normal grain growth, as seen in Figure 5.3(a). When the sintering temperature was increased to 1500 °C, the microstructure consisted of both small and very large equiaxed grains – indicating abnormal grain growth (see Figure 5.3(b)). When sintered at 1600 °C, the faster-growing grains impinge to form a coarser-grained microstructure, shown in Figure 5.3(c).

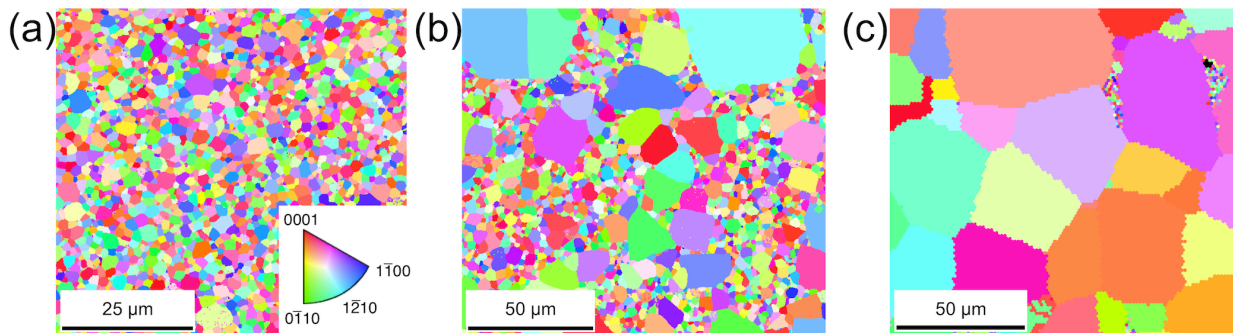


**Figure 5.3.** Orientation maps of 450 ppm Y-doped alumina with an SPS temperature of (a) 1450 °C, (b) 1500 °C, and (c) 1600 °C. The scale bar for (a) is 25 μm while in (b) and (c) the scale bars are 50 μm. Images from before pseudo-symmetry clean up.

Y+La co-doped alumina sintered at 1500 °C and 1600 °C both displayed an equiaxed grain morphology and normal grain growth, as illustrated in Fig 5.4(a) and (b). The microstructures exhibit characteristics of both the Y and La singly-doped samples. Like the Y-

doped samples, the microstructures have an equiaxed grain morphology, and like the La-doped microstructures, the grain growth is normal at 1600 °C.

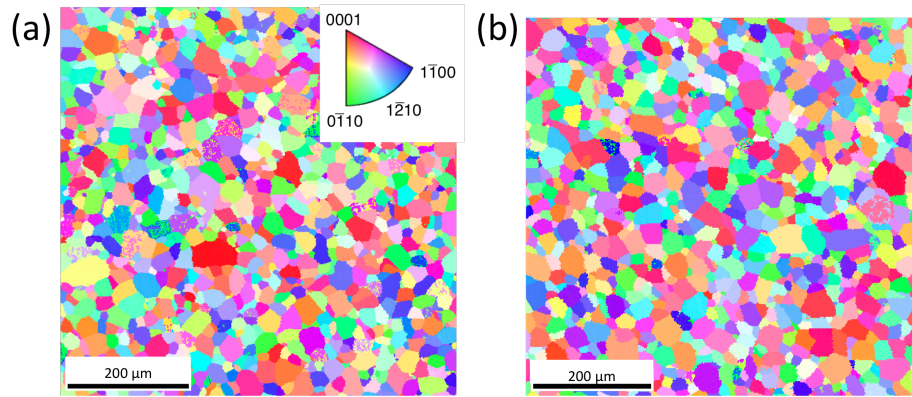


**Figure 5.4.** Orientation maps of 450 ppm Y and La co-doped alumina at (a) 1500 °C and (b) 1600 °C. Images from before pseudo-symmetry clean up.

The distributions of grain boundary planes, independent of misorientation, were calculated for each sample. The distributions for La-doped alumina at 1500 °C and 1600 °C are shown in Figs. 5.5(a) and (b), respectively. It was found that both the 1500 °C and 1600 °C La-doped alumina samples showed a significant preference for (0001) planes. The 1600 °C sample shows a 15 % decrease in the relative population of (0001) planes, suggesting that as the temperature increases, the distribution becomes less anisotropic.

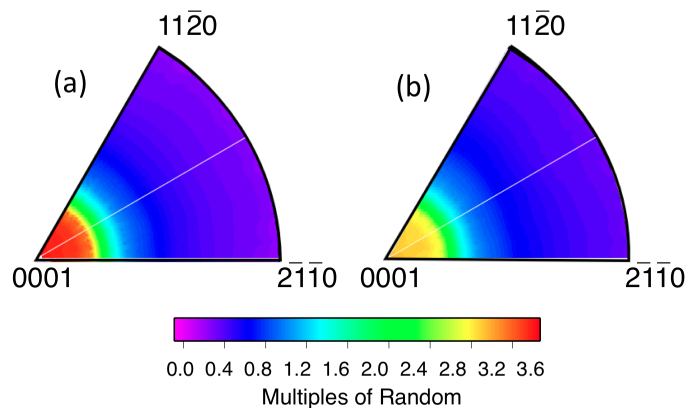


**Figure 5.5.** Grain boundary plane distributions, independent of misorientation, plotted in stereographic projection with the  $(2\bar{1}\bar{1}0)$  plane orientated horizontally to the right and the (0001) plane normal to the figure. Subsequent figures are plotted the same way. La-doped alumina sintered at (a) 1500 °C, and (b) 1600 °C.

The distribution of grain boundary planes, independent of misorientation, in the Y-doped alumina samples sintered at 1450 °C (Figure 5.6 (a)) showed a random distribution of grain boundary planes. The sample sintered at 1500 °C (Figure 5.6 (b)), which had a bimodal grain size distribution, had a preference for grain boundary planes with the  $\{01\bar{1}2\}$  orientation, referred to as the R plane. In the impinged microstructure, sintered at 1600 °C, the preference was for grain boundary planes with the  $\{1\bar{1}20\}$  orientation (Figure 5.6(c)), referred to as the A plane. Note that the widths of these distributions are much narrower than the La-doped samples.

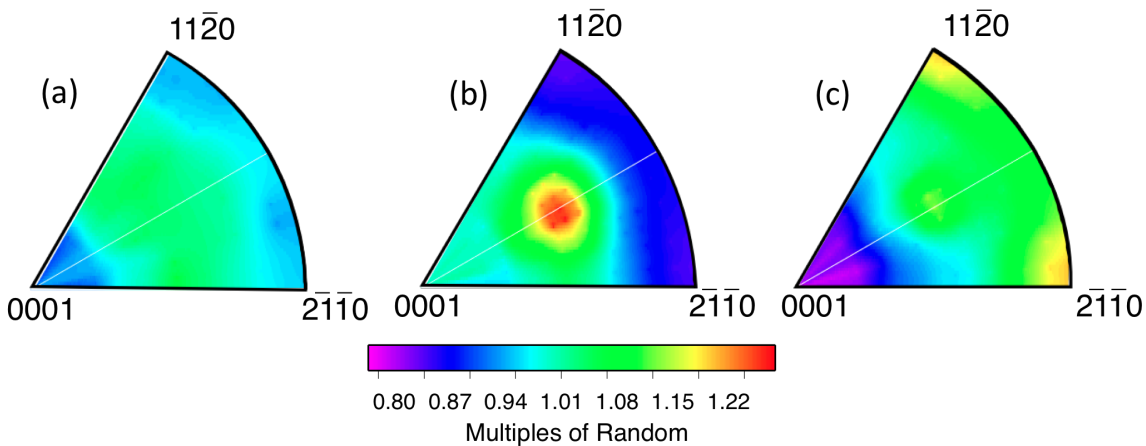


**Figure 5.6.** The distribution of grain boundary planes, independent of misorientation, in Y-doped alumina after heating at (a) 1450 °C, (b) 1500 °C, and (c) 1600 °C.

Finally, the grain boundary plane distribution for the Y+La co-doped alumina is shown in Figure 5.7. This distribution has a preference for (0001) and  $\{01\bar{1}2\}$  oriented grain boundary planes, as well the orientations between these planes. Furthermore, the distribution was approximately the same at both 1500 °C and 1600°C. This suggests that La suppresses the transition in grain boundary mobility that is found in the Y-doped sample at 1500 °C.

The grain boundary misorientation distribution was calculated with the same EBSD derived line segments used for the GBCD calculations. Note that a large amount of data was used for these calculations, as seen under the total line segments analyzed in Table 5.2, and that

these distributions are representative of the entire analyzed microstructure, rather than a single field of view. Previously reported misorientation distributions had fewer observations and were therefore classified into bins with a wider angular range. The earlier work showed a general trend for slightly higher populations of boundaries with misorientations near  $30^\circ$ ,  $60^\circ$ , and  $90^\circ$ <sup>81, 89</sup>. The current work, with many more boundary observations, use a finer ( $1^\circ$ ) discretization and is still able to produce smooth distributions. Additionally, because false boundaries related to pseudo-symmetry have been removed, we can have confidence that non-random features in the distribution are meaningful.

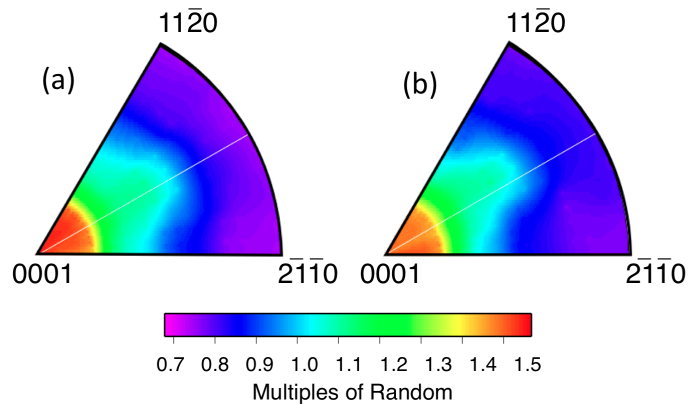


**Figure 5.7.** Distribution of grain boundary planes, independent of misorientation, for Y+La co-doped samples sintered at (a) 1500 °C and (b) 1600 °C.

The distributions of grain boundary misorientations depend on the dopant as well as grain growth kinetics. The Y-doped alumina samples show an increasing population of  $60^\circ$  boundaries with increasing sintering temperatures and increasing population of high mobility boundaries. This is illustrated in Figure 5.8, where the distributions of all grain boundary misorientations are compared to grain boundary maps of subsets of the data with  $60^\circ$  misorientations highlighted.

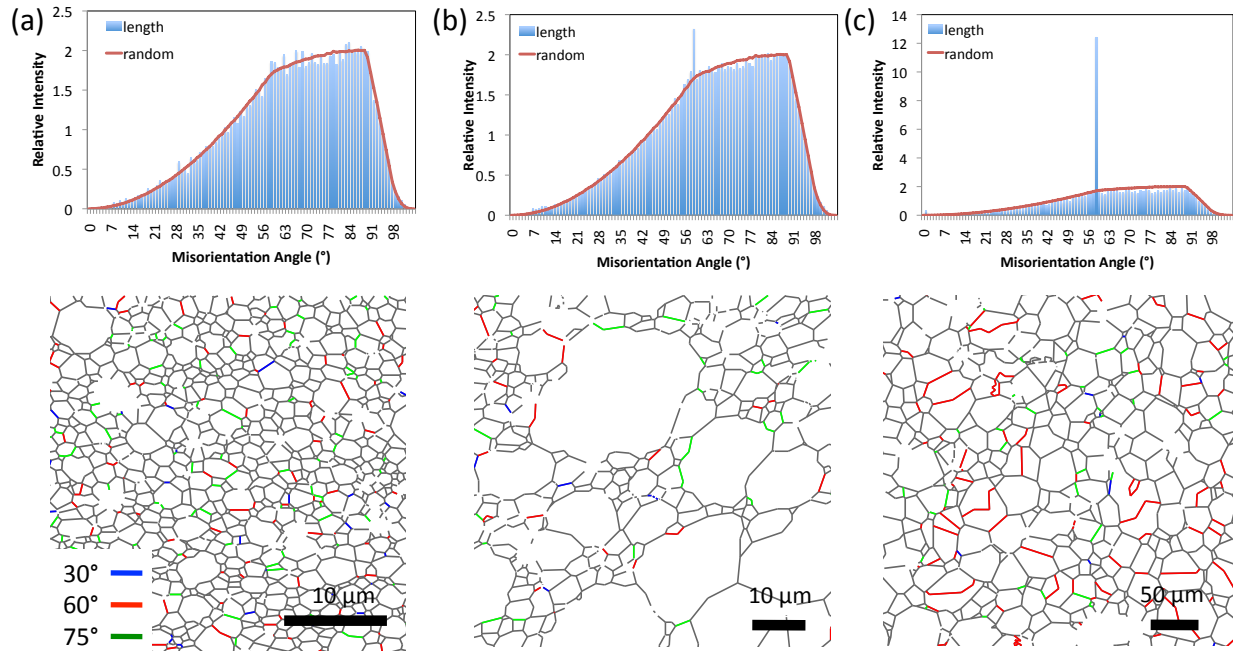


**Figure 5.8.** Misorientation distributions and corresponding reconstructed grain boundary line segments for Y-doped alumina sintered at 1450°C (a), 1500°C (b), and 1600°C – exhibiting a large increase in 60° boundaries (c). Based on the configuration of the 60° boundaries, it is concluded that they do not result from incorrect indexing because of pseudo-symmetry. Misorientation angle distribution bin sizes are 1° and range from 0 to 104 °.

After calculating the three parameter misorientation distribution function (shown in Figure 2.6), it was concluded that the peak at 60° corresponded to 60°/[0001] misorientation which is the  $\Sigma 3$  boundary in the alumina system. A large population of what appear to be twin boundaries (highlighted in red in Figure 5.8c) appears after the impingement of the large, fast-growing grains in the Y-doped alumina sample sintered at 1600 °C. The La-doped alumina samples, one of which can be seen in Fig 5.1, do not exhibit the same trend and there are no significant deviations from the random distribution. The Y+La co-doped samples exhibit a consistently high population of 60 ° misorientation boundaries where the maximum peak relative intensity is between that of the 1500 °C and 1600 °C Y-doped samples. This allows us to conclude that while the Y+La co-doping did not exhibit abnormal grain growth at the tested

sintering temperatures, the increased population of  $60^\circ$  misorientations indicates a misorientation dependence similar to Y-doped samples that exhibit AGG.

The distribution of grain boundary planes for the  $\Sigma 3$ , or  $60^\circ/[0001]$  boundaries for Y and La-doped alumina sintered at  $1500^\circ\text{C}$  are shown in Figure 5.9. There is a preference for  $\{01\bar{1}2\}$  orientations in Y-doped alumina and for  $(0001)$  orientations in La-doped alumina, which is consistent with the two-parameter grain boundary plane distributions shown in Figs. 5.5 and 5.6. For the case of the  $60^\circ/[0001]$  boundary in the Y-doped sample (Fig 5.9a), the relative areas of the  $\{01\bar{1}2\}$  orientations are 50 % greater than random. In the distribution for the La-doped sample (Fig 9b), the maximum is approximately 3.2 MRD. Based on the data in Figure 5.8(b), one might expect this to be larger. However, the relatively large bin size used for the five-parameter calculation ( $10^\circ$ ) effectively smoothes the maximum in the one-parameter misorientation distribution.

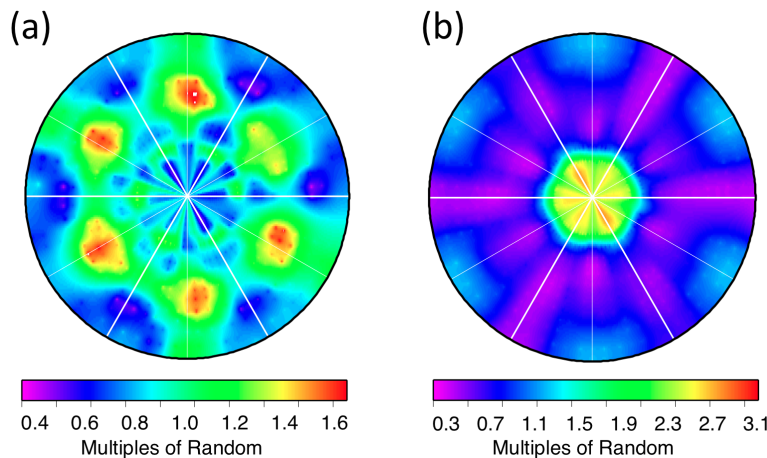


**Figure 5.9.** The grain boundary plane distribution in Y-doped alumina sintered at  $1500^\circ\text{C}$  at a  $60^\circ/[0001]$  misorientation (a) and in La-doped alumina sintered at  $1500^\circ\text{C}$  at a  $60^\circ/[0001]$  (b).

## 5.4 Discussion

The current results provide a comprehensive description of the grain boundary character distribution in Y- and La-doped alumina. Previous research has concluded that during normal

grain growth, the GBCD reaches an approximate steady state that is insensitive to average grain size<sup>90,91</sup>. This is consistent with the observations in the La-doped and Y+La co-doped alumina, shown in Figs. 5.5 and 5.7, which show only minor changes with grain growth. However, when abnormal grain growth occurs in the Y-doped alumina<sup>19</sup>, there is a significant change in the grain boundary character distribution. This is also consistent with observations in other doped aluminas and in Ca-doped yttria<sup>5,14</sup>. This change in the grain boundary plane distribution has been connected to changes in the grain boundary energies, which tend to decrease for complexions with increasing concentrations of solute<sup>6,14,21</sup>. Similarly, the misorientation angle preference in the case of AGG caused by the complexion transition shows a distinct increase in 60° misorientations as well as a change in the preferences for the orientations of grain boundary planes. However, with normal grain growth in the La and Y+La co-doped samples, the misorientation distribution is constant as well as the distribution of boundary planes. The observation that the GBCD is sensitive to dopants is consistent with the conclusions from a study of doped magnesia<sup>69</sup>. This understanding of the relationship between doping elements, grain growth kinetics, and grain boundary character development, if predictable, could lead to new insights into ceramic grain boundary engineering. At the same time, we must also note that the mesoscale results presented here do not allow us to be certain about the atomic scale structure and composition of the interfaces in these materials.

The previous studies of the effect of complexion transitions on grain boundary plane distributions only considered the distributions before and during the transition; here we also have data after the transition<sup>5,14</sup>. The distribution of planes during the expansion of the fast growing grains into the smaller grains is dominated by  $\{01\bar{1}2\}$  planes, but after the grains impinge,  $\{1\bar{1}20\}$ -type planes are preferred. In the absence of abnormal grain growth, the relative grain

boundary energies are the most important factors that influence the grain boundary population<sup>33, 90</sup>. Therefore, the observations indicate that after the complexion transition, the boundaries terminated on  $\{1\bar{1}20\}$ -type planes have relatively lower energies. However, in the transient growth stage, the boundaries around the large abnormal grains will dominate the population, and the orientation of these boundaries is more likely to be determined by relative mobilities. It should be noted that the grain boundary orientation distribution in the Y-doped alumina system is not strongly anisotropic. The relative areas of the preferred grain boundary planes are only about 1.3 times more likely to occur than an orientation in a random distribution. The more important non-random characteristic of the grain boundary distribution is found in the domain of misorientations, with a strong preference for the  $\Sigma 3$  grain boundary (see Figure 5.8). There is ample experimental and theoretical evidence that as grain growth occurs, the lowest energy boundaries are eliminated less frequently and accumulate in the network<sup>68</sup>. This is one possible explanation for the increase in  $\Sigma 3$  grain boundaries with grain growth. However, it is also possible that the uniaxial load from the SPS and degraded creep properties at 1600 °C could have activated basal slip, which has been previously observed in the Y-doped alumina<sup>58, 81, 92</sup>. It should also be noted that the La and Y+La-doped alumina show a strong preference for (0001) grain boundary plane orientations, regardless of misorientation.

Galmarini et al.<sup>93</sup> simulated the effect of Y segregation on the energies of alumina surfaces and grain boundaries. From these calculations, it was determined that Y segregated to  $\{1\bar{1}20\}$  and  $\{01\bar{1}2\}$  surfaces at 1600°C, with the  $\{1\bar{1}20\}$  plane having its relative energy decreased the most. The energies of selected low  $\Sigma$ -CSL boundaries with and without Y were also calculated. The results showed that Y segregated to some, but not all boundaries, and also lowered the energy. With limited numbers of calculations, it is not possible to make detailed

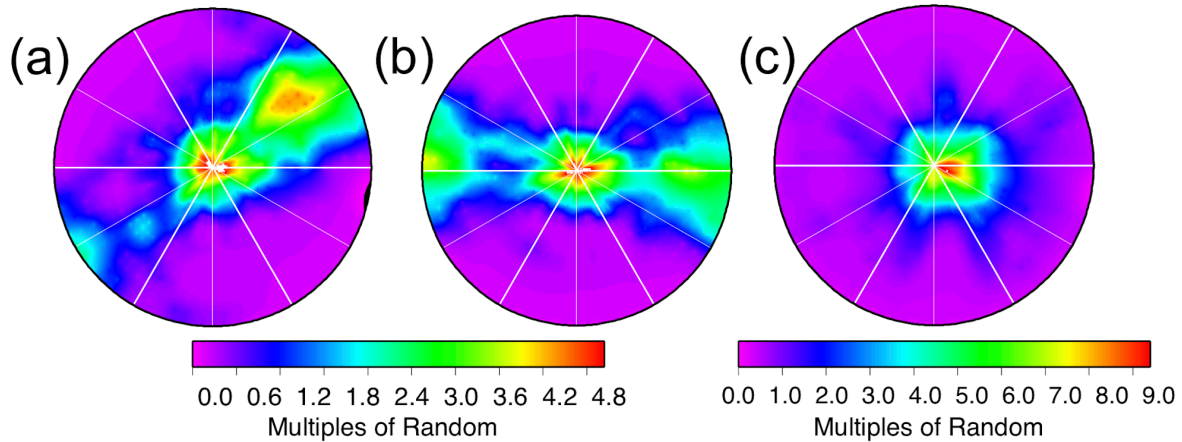
comparisons to the present work. However, we can remark that Galmarini's prediction that for the  $\Sigma 3$  boundaries,  $\{11\bar{2}0\}$  plane grain boundaries in Y-doped alumina are much lower in energy than the (0001) plane boundaries is consistent with the observed populations.

Experimentally, Gülgün et al.<sup>18</sup> observed a high proportion of (0001),  $\{11\bar{2}0\}$ , and  $\{01\bar{1}2\}$  plane interfaces in the Y-doped alumina samples they investigated using transmission electron microscopy (TEM). Similarly, another TEM study, reported by Bouchet et al.<sup>17</sup>, showed that Y-doped alumina sintered at 1450°C and 1550°C both showed a higher level of Y segregation to the  $\{01\bar{1}2\}$ -plane than to (0001); in their study, the Y/Al intensity peak ratio for  $\{01\bar{1}2\}$  planes was 2.5-2.7 compared to 0.2-1.7 for (0001) planes. Both of these investigations are consistent with the current mesoscale experimental results that at temperatures above 1450°C, Y segregation leads to a complexion transition that lowers the energy of boundaries with  $\{01\bar{1}2\}$  planes and increases the grain boundary mobility. When the transition occurs only around some grains, AGG results. After the fast-growing grains impinge, the  $\{01\bar{1}2\}$  plane is the most common, suggesting that this orientation has the lowest energy.

There have been several mesoscale studies of grain boundary populations in alumina. In general, no large-scale deviations from random misorientation distributions have been found in pure or doped aluminas<sup>81, 86, 89</sup>. Furthermore, the populations of low  $\Sigma$ -CSLs are only modestly enhanced in population over the population expected in a random distribution. For example, Vonlanthen and Grobety<sup>89</sup> found that about 4 % of the boundaries in alumina could be classified as belonging to a CSL misorientation with  $\Sigma \leq 28$ , compared to an expectation of 2.7 % in a random distribution. Cho et al.<sup>81</sup> reported that Y-doping increased the occurrence of  $\Sigma 3$  boundaries from roughly 0.6 % to 2.3 %. The observed increase that occurs with Y-doping is consistent with the current study.

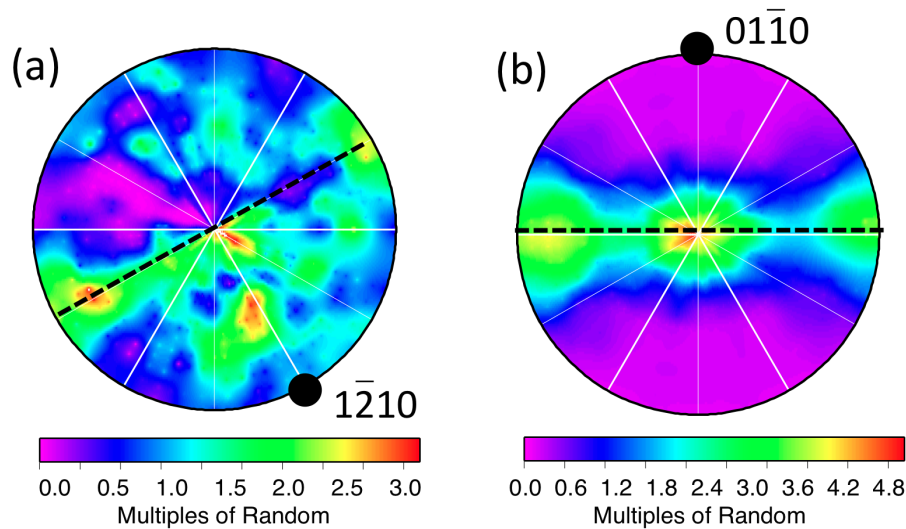
While it has been shown that lattice coincidence is not a good predictor of the relative population or energies of the grain boundaries<sup>33, 34</sup>, the use of CSL notation is convenient when trying to compare results from different analysis techniques, and is prevalent in alumina grain boundary research. However, this literature is not entirely consistent in nomenclature. The first list of CSL misorientations for rhombohedral  $\alpha$ -alumina was published by Grimmer et al<sup>94</sup>. More recently, Vonlanthen and Grobety<sup>89</sup>, beginning from Grimmer's previous report on coincident orientations in rhombohedral materials<sup>95</sup>, accounted for the possibility of small variations in the c/a ratio and in some cases reached different results for alumina. So that there is no confusion, the source of the specified notation and misorientation will be labeled in each case with a "G" Grimmer et al<sup>94</sup> or a "V" for Vonlanthen and Grobety<sup>89</sup>.

Figure 5.10 shows the distribution of grain boundary planes for the  $\Sigma 7_a(G)$ ,  $\Sigma 7_2(V)$ , and  $\Sigma 31_b(G)$  boundaries in La-doped alumina sintered at 1600°C. In each case, the maximum is near (0001), indicating a preference for the basal plane. This is consistent with the results in Figure 5.5 that are averaged over all misorientations. It should be noted from the grain boundary plane distributions that these misorientations are not significantly different from those at randomly selected misorientations. This leads us to conclude that lattice coincidence does not impart any special significance to these boundaries. Similar plots for the Y-doped system (not shown) did not show strong maxima or other characteristics that distinguished them as special. However, we also note that at the current resolution of approximately 10°, there is a possibility that a special boundary that occurs in a very narrow angular range will be averaged with neighboring boundaries such that its apparent population is less than its true population. It is currently not possible to examine plane distributions at specific misorientations at higher resolution, because of the size of the domain of boundary types.



**Figure 5.10.** Grain boundary plane distributions for La-doped alumina sintered at 1600°C. (a)  $\Sigma_{7a}G$  ( $85.9^\circ/[02\bar{2}1]$ ), (b)  $\Sigma_{7_2}V$  ( $85.9^\circ/[24\bar{6}1]$ ), (c)  $\Sigma_{31_b}G$  ( $63.15^\circ/[11\bar{2}3]$ ).

The grain boundary energies of symmetric tilt boundaries have been experimentally evaluated using bicrystals<sup>20, 96–98</sup>, calculated by static lattice simulations<sup>99</sup>, and density functional theory<sup>100</sup>. Kenway<sup>99</sup> calculated the grain boundary energy of the  $\{10\bar{1}1\}/\{10\bar{1}\bar{1}\}$  tilt with a near  $\Sigma_{11}$  misorientation, the boundary was tilted  $144.8^\circ$  around  $\langle \bar{1}2\bar{1}0 \rangle$ . Milas et al.<sup>100</sup> further modeled the same near  $\Sigma_{11}$  boundary to explore the grain boundary structure with the addition of transition metals, such as Y. Here we look at experimental measurements of bulk alumina to determine the likelihood of grain boundaries with these misorientations occurring in a real sample. The Y-doped alumina GBCD for  $144.8^\circ/[1\bar{2}10]$  shows a strong population of  $(\bar{1}0\bar{1}\bar{1})$ ,  $(0001)$ , and  $(10\bar{1}0)$  planes along the tilt axis (Figure 5.11 a). While the expected  $\{10\bar{1}1\}/\{10\bar{1}\bar{1}\}$  planes did occur, they are not the only tilt boundaries at the specified misorientation. The GBCD of the  $\Sigma_{11}$  boundaries in the La doped sample shows a high population of  $(0001)$  planes with no tilt boundary preference. However, a real  $\Sigma_{11_b}(G)$  boundary at  $95.2^\circ/[01\bar{1}0]$  in La-doped alumina reveals a tilt boundary of  $(0001)$  and a geometrically necessary complement of  $(\bar{2}110)$  planes (Fig 5.11 b). Note that this preference for the basal orientation on one side of the boundary is a characteristic at all tilt angles.



**Figure 5.11.** The grain boundary plane distribution for boundaries with a misorientation of  $144.2^\circ/[1\bar{2}10]$  (near  $\Sigma 11$ ) of Y-doped alumina, showing  $(\bar{1}0\bar{1}\bar{1})$ ,  $(0001)$ , and  $(10\bar{1}0)$  planes oriented along the tilt zone (a). The misorientation axis and tilt zone are defined by black circle and dotted line, respectively. The grain boundary plane distribution for boundaries with a misorientation of  $95.2^\circ/[01\bar{1}0]$  ( $\Sigma 11_b$ ) of La-doped alumina showing a symmetric boundary with high populations at  $(0001)$  and  $(\bar{2}110)$  planes – both of which are oriented along the  $[01\bar{1}0]$  tilt axis (b).

Nishimura et al.<sup>96</sup> investigated the atomic structures and energies of  $\Sigma 7$  ( $38.2^\circ/[0001]$ ) symmetric tilt boundary bi-crystals with grain boundary planes  $\{4\bar{5}10\}$ ,  $\{2\bar{3}10\}$ , and  $\{\bar{1}\bar{1}02\}$ . While the chemistry of these samples is not the same, this is the only prior work available for comparison in which all of five crystallographic parameters of the measured grain boundaries were controlled. It was found that the  $\{\bar{1}\bar{1}02\}$  plane exhibited the lowest grain boundary energy, and concluded that the grain boundary energy is highly dependent on the grain boundary plane. Figures 5.12a and b show the  $\Sigma 7$  boundary in the Y-doped and La-doped alumina samples, respectively. The Y-doped sample shows a weak preference for  $\{\bar{1}\bar{1}02\}$  planes and this suggests that it is the lowest energy grain boundary plane, consistent with the findings of Nishimura et al.<sup>96</sup> The La-doped sample shows a preference for the  $(0001)$  twist boundaries. The lack of

agreement in this case is not surprising considering that the grain boundary chemistry differs and this can alter the grain boundary energies.

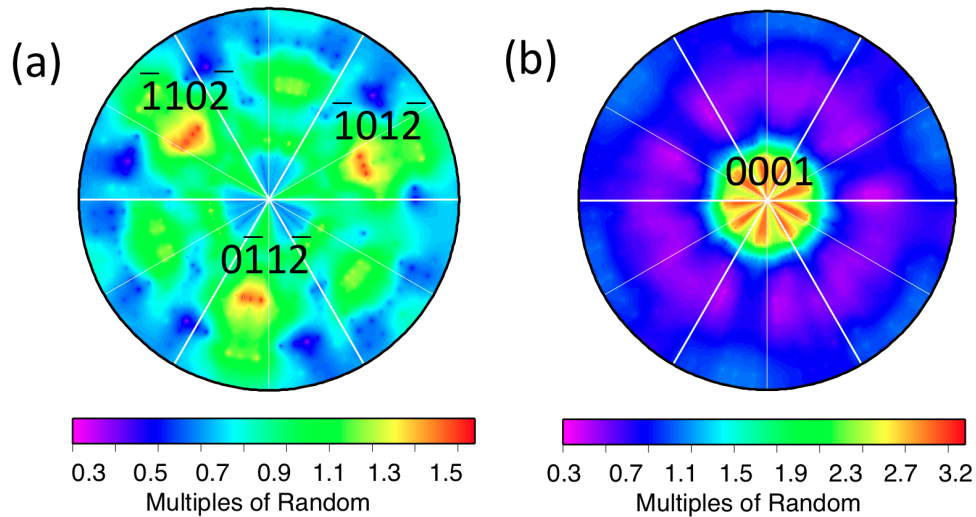


**Figure 5.12.** Distribution of grain boundary planes for the misorientation of  $38.2^\circ/[0001]$  ( $\Sigma 7$ ) for (a) Y-doped alumina and (b) La-doped alumina.

## 5.5 Conclusions

While Y and La doping both increase the creep resistance in alumina, they have different grain boundary plane and misorientation distributions. After false boundaries that derive from pseudo-symmetry effects are removed, the misorientation distribution in La-doped alumina is essentially random. However, the grain boundaries do show a preference for (0001) planes at all temperatures and at all misorientations. At 1500 °C, the preference is, on average, 3.7 times random. Y-doped alumina, on the other hand, has a larger than random population of  $\Sigma 3$  grain boundaries, with a  $60^\circ$  misorientation about the [0001] axis. After annealing at 1600 °C, these boundaries occur in the population six times more than expected in a random distribution. With that one exception, other low  $\Sigma$  CSL boundaries had no characteristics to distinguish them from random boundaries in any of the samples. Y-doped alumina undergoes a complexion transition between 1450°C and 1600°C in which higher mobility grain boundaries appear, leading to

abnormal grain growth. The Y-doped materials have a preference for  $\{01\bar{1}2\}$ -planes during abnormal grain growth and  $\{1\bar{1}20\}$ -planes after the abnormal grains impinge. Y+La-co-doping results in a microstructure consisting of equiaxed grains that exhibit both a preference for (0001) and  $\{01\bar{1}2\}$  orientations. This work verifies the hypothesis that the grain boundary character anisotropy increases with a complexion transition. An unexpected result, however, is that after the abnormal grains impinge, a different plane is preferred.

## **6. Experiment III: Experimental test of the effect of grain boundary energy on the nucleation of complexion transitions**

The following chapter takes the understanding that grain boundary complexion transitions decrease the relative grain boundary energy of a material as well as increase the anisotropy of the grain boundary character distribution, and further explores potential applications of this knowledge. By using the mesoscale results for Y-doped alumina presented in Chapter 5, we now present an experiment that controls the energy by controlling the character of specific interfaces within a doped polycrystalline sample. By doing this, we can test the hypothesis that by controlling the energy of interfaces we are able to control when and where complexions occur.

### **6.1 Introduction**

The yttrium doped alumina system was selected for this investigation because this dopant causes an apparent discontinuous complexion transition that results in abnormal grain growth. Furthermore, as discussed in the introduction of Chapter 5, yttrium increases the creep resistance and decreases the grain growth rate of alumina – leading to an ideal combination of properties<sup>23, 24, 58, 73, 77, 82</sup>. All mesoscale observations of abnormal grain growth in this system - such as the GBCD, grain boundary energy, and changes in mobility - indicate that a complexion transition has occurred<sup>1, 6, 72</sup>. However there have not been any conclusive results indicating that there is in fact a difference in grain boundary structure and/or chemistry between the boundaries surrounding the largest grains compared to those surrounding the smallest grains. Therefore, choosing this system facilitates both a mesoscale characterization study on the grain boundary character and energy influence on complexion transitions and an investigation on grain boundary structure and chemistry with a specific focus on classifying different complexions.

The previous work on doped-alumina and doped-yttria indicate that the mean relative interfacial energies of the boundaries surrounding abnormal grains resulting from the nucleation of an equilibrium complexion are lower than the energies of metastable grain boundaries surrounding normal grains in the same material<sup>6, 14, 21</sup>. In the case of Y-doped alumina, we see a 46% decrease in mean relative boundary energy when comparing the energy distributions of boundaries surrounding abnormally large grains compared to those surrounding smaller grains that are adjacent to the abnormal grains<sup>6</sup>. This corresponds to an increase in anisotropy of the grain boundary plane distribution, which ultimately results in a larger population of  $\{1\bar{1}20\}$  planes and fewer (0001) planes<sup>72</sup>. Because grain boundary populations are inversely related to grain boundary energy<sup>35, 68, 101, 102</sup>, it can be assumed that the (0001) planes exhibit a higher interfacial energy in the Y-doped alumina system than  $(1\bar{1}20)$  planes. Additionally, Dillon et al.<sup>5</sup> measured the interfacial energy between undoped polycrystalline alumina and single crystal sapphire with low index (C, A, R) orientations. It was found that these low index planes exhibited lower mean energies than randomly distributed grain boundaries. The relative differences in energy were in agreement with surface energy measurements in the literature.

The current work systematically combines the previous results to determine if grain boundary energy is truly an influential factor in the nucleation of complexion transitions. By comparing the relative grain boundary energies and the population of abnormal grains at the interface of (0001) and  $(1\bar{1}20)$  single crystals embedded in Y doped-polycrystalline alumina, it will be possible to directly link grain boundary energy to the nucleation of complexion transitions.

## 6.2 Experimental Procedures

Yttrium doped alumina powder was prepared by mixing pure alumina powder (Puratronic, Alpha Aesar 99.995% pure) with 500 ppm  $Y(NO_3)_3 \cdot 6H_2O$  (Alpha Aesar, Ward Hill, MA). The powders were mixed with methanol and stirred on a hot plate in a fume hood to evaporate the liquid; this was done to assure mixing while minimizing environmental contamination. Sapphire single crystals were also purchased (MTI Corp, Richmond, CA) and were thoroughly cleaned to avoid contamination.

The sample was organized in the graphite die such that a small amount of Y-doped alumina powder was interfaced with the graphite plunger, the C-plane (0001) sapphire was then laid parallel to the die and the polished side of the crystal was oriented upward. Y-doped alumina powder was then layered onto the C-plane sapphire and finally A-plane ( $11\bar{2}0$ ) sapphire single crystal was layered on top of the powder topped with a small amount of powder, as seen in figure 3.1, and a green body was pressed. The samples were then spark plasma sintered (Thermal Technologies, LLC, Santa Clara, CA) according to the following procedure: A ramp of 100 °C/min to 800 °C and 10 MPa for an initial calcination dwell of 45 minutes, this was followed by an additional 100 °C/min ramp to 1300 °C at 50 MPa for 30 minutes to sinter.

The SPSed sample was then sectioned into smaller cross sections. One section was further sintered in air for 8 hours at 1500°C – a known temperature for AGG in Y-doped alumina. Each section was then polished to a 0.05  $\mu\text{m}$  diamond finish (Buehler, Lake Bluff, IL), removed from its mount, and thoroughly cleaned. Thermal grooving was then preformed at 1350°C for the as SPS sample and 1400 °C for the 8 hour annealed sample for 15 hours. See Section 3.5.2 for further discussion regarding the difference in groove temperature. Automated EBSD maps were then collected to analyze the overall distribution of grain sizes along the

interfaces, as well as to assure there was no grain growth while grooving, representative EBSD maps can be seen in Figure 6.1. Topographic images of each interface were also collected using contact mode AFM, these can be seen in Figure 6.2.

At least 100 individual boundaries were analyzed along both the (0001) and  $(11\bar{2}0)$  interfaces, and a modified half angle version of Mullins' analysis<sup>5</sup>, as described in Chapter 3, was performed according to the methods described by Saylor et al.<sup>37</sup> with the modifications introduced by Dillon et al.<sup>30</sup>. This analysis allows for the calculation of the relative grain boundary energy of each interface. From this, the cumulative distribution of the average and standard deviation of the ratio of grain boundary to surface energy for each boundary were plotted according to the adjacent single crystal interface, and statistics from that distribution were compared.

### 6.3 Results

The orientation maps along both the as SPSed (0001) and  $(11\bar{2}0)$  interfaces can be seen in Figure 6.1 a and b. The regions of constant orientation on the left and right sides are the edges of the single crystals. The polycrystalline material between the single crystals is dense and shows a normal distribution of grain sizes, with an average size of 1.02  $\mu\text{m}$ . The single crystal surfaces do not remain perfectly flat because they sinter with the alumina powder. However, the average orientation of the interface is maintained.

Because multiple measurements were made for each boundary, a mean and standard deviation were determined and plotted in Figure 6.3 – these measurements represent the change in a single boundary as opposed to the uncertainty of a single measurement. Cumulative distribution plots for the measured dihedral angles and the relative grain boundary energies at the (0001) and  $(11\bar{2}0)$  interfaces are compared for the as sintered sample in Figure 6.3(a). As

expected from the results presented in Chapter 5, the grain boundary character distribution, the interface with the  $(1\bar{1}20)$  interface has a lower mean relative energy (0.55) than the one with the  $(0001)$  orientation (1.15). Furthermore, the standard deviation of the higher energy interface (0.30) is larger than that of the lower energy interface (0.21). Random boundaries at least two grains away from both the  $(0001)$  and  $(1\bar{1}20)$  interfaces in the as sintered sample have an average relative energy (0.71). This indicates that a random sampling of polycrystalline grain boundaries displays a 62% lower energy than the high energy  $(0001)$  plane, but also 22 % higher than the lowest energy  $(1\bar{1}20)$  plane.

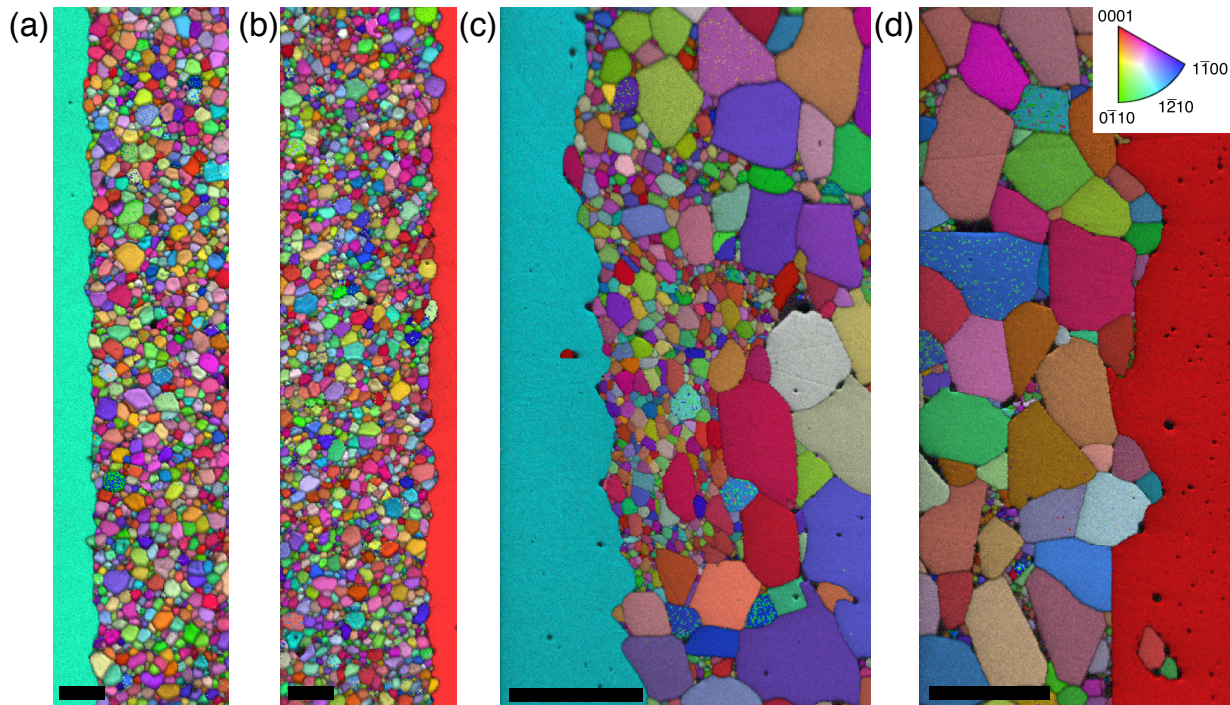


**Figure 6.1.** Inverse Pole Figure +Image Quality Maps looking down the  $[010]$  direction for Y-doped alumina as SPS  $(1\bar{1}20)$ - plane (a) and  $(0001)$ -plane (b), and sintered at  $1500^{\circ}\text{C}$  for 8 hours  $(1\bar{1}20)$ -plane (c) and  $(0001)$ -plane (d). The square in (d) indicates the faceting that occurs along the  $(0001)$  interface. The lengths of the scale bars are (a) 5 mm, (b) 5 mm, (c) 50 mm, and (d) 45 mm.

The sample containing the  $(0001)$  and  $(1\bar{1}20)$  oriented crystals was then heated in air for 8 h at  $1500^{\circ}\text{C}$ , which is above the temperature where a grain boundary complexion transition is expected. The sample was then polished to a  $0.05\ \mu\text{m}$  diamond finish and thermally grooved at

1400 °C for 15 h in air. Orientation maps of this sample are illustrated in Figure 6.1(c) and 6.1(d). After the high temperature anneal, there is a bimodal grain size distribution in the bulk of the polycrystal, where the average grains size for grains smaller than 10 μm was 3.2 μm and the average grain size for grains larger than 10 μm is was 19.8 μm. However, there is also a distinct difference between the two interfaces. The microstructure along the (0001) interface contains nearly all larger grains, but the microstructure along the  $(11\bar{2}0)$  interface contains mostly smaller grains. The maps in Figure 6.1 are characteristic of the entire interface.

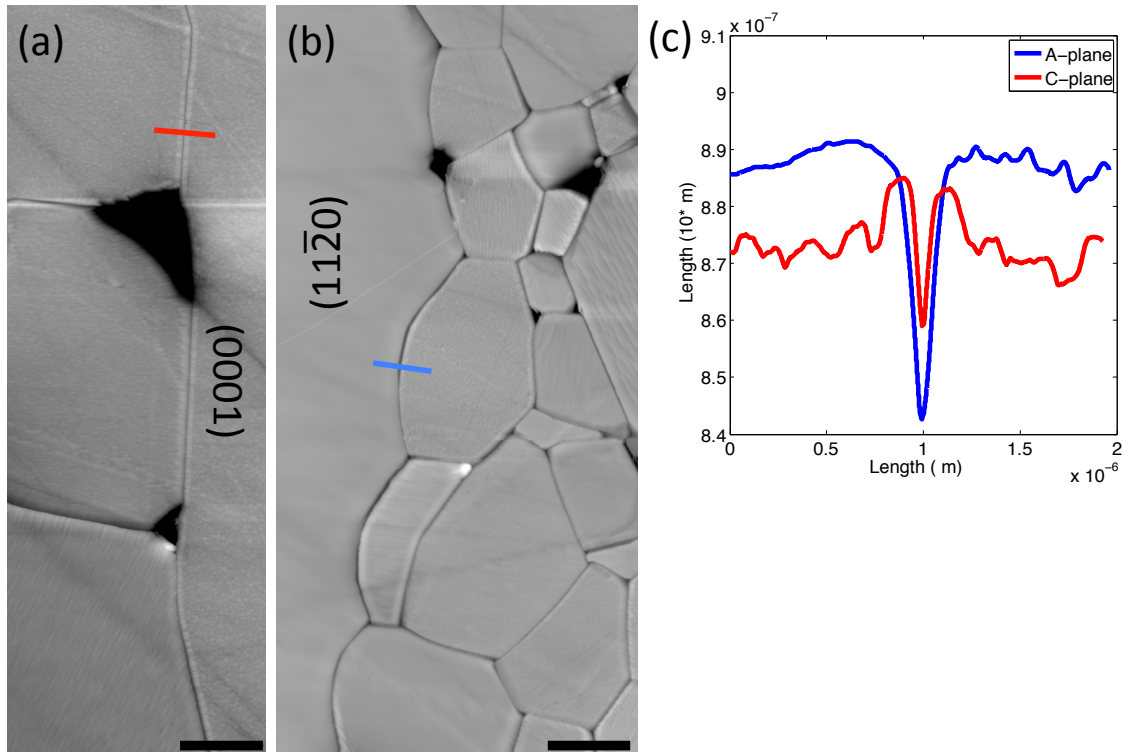


**Figure 6.2** Representative AFM images of the partially transformed  $(11\bar{2}0)$  interface (a), almost completely transformed  $(0001)$  plane (b), and example boundary line profiles from each scan (c). The red line profile corresponds to the red line in (a), and the blue corresponds to the blue line in (b). The lengths of scale bars in (a) and (b) are 3 μm

The relative grain boundary energies were measured for the sample that was heated for 8 hours at 1500 °C, measuring the  $(0001)$  and  $(11\bar{2}0)$  interfaces in the same way as before the heat treatment, and the cumulative distributions are shown in Fig 6.3(b). As before the anneal, the

(0001) plane has a higher energy than the  $(11\bar{2}0)$  plane. However, the grain boundary energies decreased by 19 % for the (0001) interface and 27 % for the  $(11\bar{2}0)$  interface. Table 6.1 shows the statistical mean, deviation, and number of grain boundaries analyzed for each energy distribution.

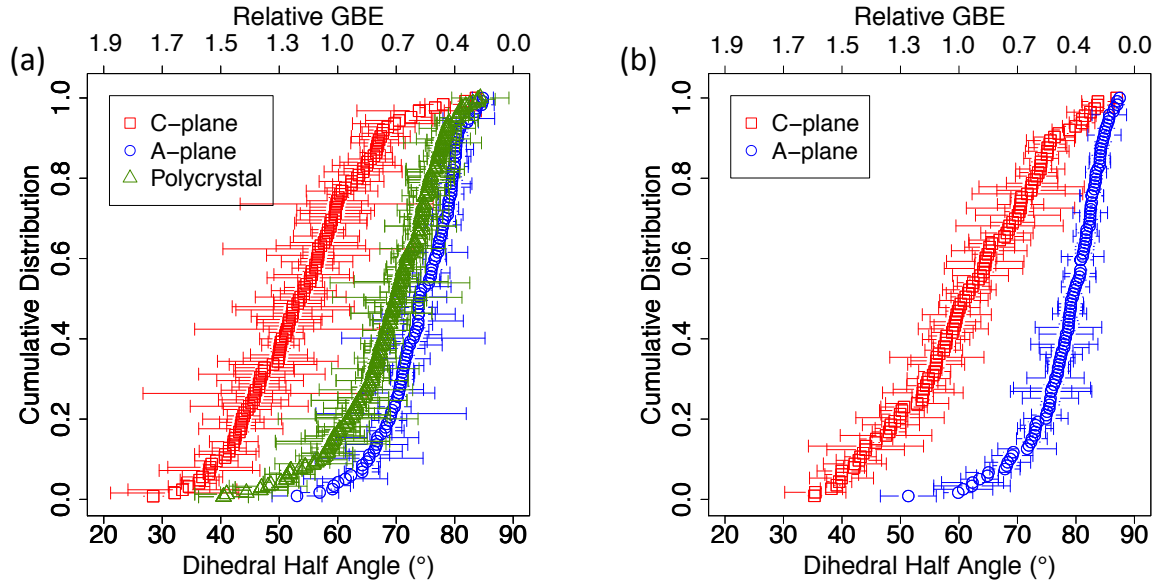


**Figure 6.3.** Cumulative distributions of relative grain boundary energy for (a) the sample that was thermally grooved immediately after SPS, and (b) the sample annealed for 8-hours at 1500°C inducing AGG. (c) A-plane before (blue) and after (red) the 8 hour anneal and (d) the C-plane before (blue) and after (red) the 8 hour anneal.

**Table 6.1.** Statistical results of Grain Boundary Energy Distribution

Sample	Interface	Mean energy	St. Dev.	Groove Count
As SPS	A-plane	0.55	0.21	118
	C-plane	1.15	0.30	126
8h at 1500°C	A-plane	0.40	0.21	119
	C-plane	0.93	0.37	113

A-plane is  $\{11\bar{2}0\}$  and C-plane is (0001)

## 6.4 Discussion

These results show that more abnormal grains grew along the initially higher energy (0001) interface. This suggests that the higher average energy at the (0001) interface ( $d_p$ )

decreased the energy needed to overcome the nucleation barrier ( $\Delta E$ ) to form the lower energy complex, as seen schematically in Figure 6.4. The decrease in energy and only partial transformation along the  $(11\bar{2}0)$  interface implies that the energy barrier surmounted to nucleate the transition on the boundaries that were transformed was greater than that at the  $(0001)$  interface. If this is the case, then a difference in boundary energy can lead to a range of nucleation barriers needed to transform the grain boundary from a metastable to an equilibrium complex. After the transition occurs, there would again be a range of character-dependent boundary energies for the new, lower energy complex.

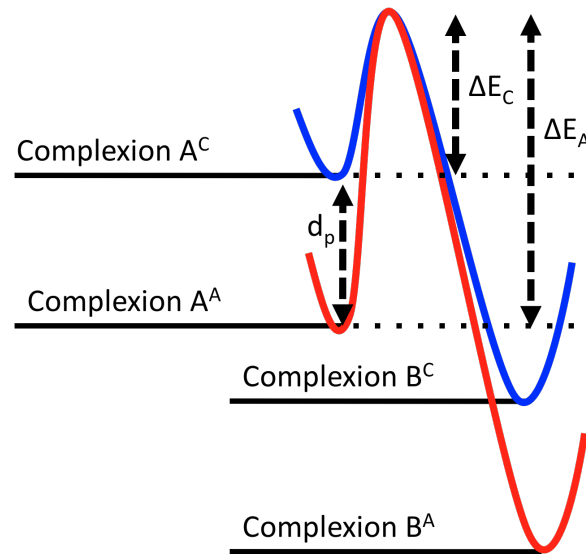


**Figure 6.4.** Grain boundary energy schematic showing the difference in initial interfacial energy of the C/ $(0001)$  and A/ $(11\bar{2}0)$  planes ( $d_p$ ) exhibiting complexion A, and the corresponding activation energies ( $\Delta E_C$  and  $\Delta E_A$  respectively) needed to nucleate the equilibrium complexion B.

The bimodal grain size distribution and the 27% decrease in energy along the  $(11\bar{2}0)$  interface of the 8 hour annealed sample indicate that there may also be a temperature and grain boundary energy dependence on the rate of complexion transitions. Where the rate of nucleation of transitions is dependent on the temperature available to nucleate the transition as well as the available grain boundary energy. It is possible that all of the boundaries along both the  $(0001)$

and  $(1\bar{1}\bar{2}0)$  interfaces transformed, but the boundaries along the lower energy  $(1\bar{1}\bar{2}0)$  interface transformed at a later time because of their lower energy, and the grains did not have enough time to grow abnormally large. A difference in misorientation and slight differences in boundary plane orientation would result in a range of boundary energies along the crystal interface, and in the case of the lower energy  $(1\bar{1}\bar{2}0)$  interface it would cause a portion of the boundaries to transform long before others – resulting in some abnormal grains. If, however, the samples were heated for a shorter time, less of the grains along the  $(0001)$  interface would exhibit AGG, and an even smaller portion along the  $(1\bar{1}\bar{2}0)$  interface would exhibit AGG. Subsequently, at longer times both interfaces might be lined with impinged abnormal grains.

The previously discussed Ca-doped yttria experiments have shown that while large grains are a good indicator of a transformed boundary, not all transformed boundaries necessarily bound just the largest grains<sup>14, 21</sup>. The Ca-doped yttria results showed that some boundaries ahead of the growing abnormal grains have already transformed. Another possibility for the bimodal distribution along  $(1\bar{1}\bar{2}0)$  is that the entire interface may have transformed, but the grains were not connected in a way that promoted single large grains to grow. However, because of the statistical nature of these energy distributions, it is not possible to state the true cause of the inconsistent AGG.

In prior work, the energy change associated with this complexion transition was measured to be 46 %<sup>68</sup>. In the current experiment, the measured decreases were 19 % for the  $(0001)$  interface and 27 % for the  $(1\bar{1}\bar{2}0)$ . While these decreases are smaller, the initial state was also quite different. In the earlier experiment, the energies of boundaries surrounding only abnormally large grains were compared to boundaries surrounding only small grains. In the current work, a bimodal distribution occurred along both the  $(0001)$  and  $(1\bar{1}\bar{2}0)$  interfaces so a

partial transformation along those interfaces is assumed. The average energy along each interface was measured without knowing the complexion of any specific grain boundary. Therefore, a sampling of both grain boundary states was incorporated in the result. This resulted in the smaller decrease in grain boundary energy along both interfaces after the grain boundary transition occurred, compared to the previous experiment.

It is also possible that multiple types of discrete grain boundary complexion transitions may have occurred in this experiment. Dillon et al. showed that in the Si/Y co-doped alumina system, there were at least five discrete grain boundary complexions<sup>11</sup>. The sample in the current experiment was only doped with Y, however some Si contamination could have occurred during the heating process. From that it could be also possible that two or more transformations resulting in two distinct energy reductions as well as two mobilities could have occurred when heated to 1500 °C. Due to the mesoscale nature of this analysis the precise chemical composition and structure of individual boundaries cannot be verified.

The cumulative distribution of relative boundary energies along both the (0001) and (11 $\bar{2}$ 0) interfaces exhibit a distinct shape. The boundaries formed at the (11 $\bar{2}$ 0) oriented crystal interface in the as sintered sample have a relatively symmetric distribution, characteristic of a normal cumulative distribution. However, when heated for 8 hours at 1500°C, the highest 20% of measured boundaries are still greater than the average of the untransformed dataset, and the maxima are the same within uncertainty. In other words, even though the mean of the partially transformed distribution is 27% less than the mean of the original pre-transformation sample, the highest energy boundaries in the tail appear to remain. This underscores the fact that we are not looking at the same boundaries before and after and that as the microstructure evolves, new boundaries that sample the entire range of energies are constantly being created when two grains

grow into one another. Therefore, even though the mean value decreases, this does not preclude the formation of new, high energy boundaries during the normal course of microstructural evolution.

Additionally, it should be noted that the crystal interfaces are no longer planar. So while the orientations of the grain boundaries are, on average, equal to the original orientation, there are significant local deviations. In the case of the original (0001) interface, some (0001) faceting does seem to occur (as indicated in Figure 6.1). The previous Y-doped alumina grain boundary character distribution results showed a preference for  $60^\circ/[0001]$  misorientation<sup>72</sup>, which appeared to be a type of twin in the microstructure of impinged AGG. This could explain the faceted grain morphology in the case of the impinged AGG along the (0001). Unexpectedly, however, it appears that those facets could be the (0001) plane, which was not the case in the original GBCD experiment.

These results show that, after sintering at 1500°C, the initially higher energy (0001) interface is surrounded by many more abnormally growing grains compared to the  $(11\bar{2}0)$  interface. However, the energy measurements for each interface indicate that both boundaries transformed to a lower mean energy. This raises questions about the link between the rate of grain boundary complexion transitions and the obvious appearance of abnormal grains.

## 6.5 Conclusions

Measurements of the relative grain boundary energy in the as SPS Y-doped alumina sample show that the grain boundaries at the  $(11\bar{2}0)$  interface have lower average energies than those at the (0001) interface. Further microstructural analysis shows that complexion transitions do not occur homogeneously, where the transformation to the high mobility complexion is more extensive at the higher energy (0001) interface. Measurements of the relative grain boundary

energy after the high temperature anneal show that the relative energies decreased, indicating that the complexion transition occurred on both interfaces. Overall, this work has shown that complexion transitions are more probable at higher energy grain boundaries, and further work must be done to fully understand the relationship between grain boundary energy, the rate of these transformations, and the eventual appearance of abnormally large grains.

## 7. Experiment IV: Investigating the Kinetics of Grain Boundary Complexion Transitions

Throughout research on complexion transitions in alumina, there has been an assumed one-to-one association between abnormally large grains and grain boundaries transformed to higher mobility complexions. While there is considerable support for this association, it must also be recognized that such an association might not hold in all cases. For example, the case of Ca-doped yttria (Chapter 4), where the boundaries between normal grains that shared a triple point with an abnormal grain had the same energy as the high mobility boundary (but those further away has a much higher energy), illustrates a case where the one-to-one association does not hold. One can imagine several circumstances where this might occur. One is that boundaries might transform, but grains do not appear abnormal until a critical number of boundaries on the periphery of the same grain have transformed and it has time to grow to a noticeably larger size. A second possibility is that so many boundaries transform that no grain has a significant advantage over the others and the grain size distribution remains normal. Additionally, the C/A plane Y-doped alumina experiment in Chapter 6 showed that the grain boundary transformation kinetics may be dependent on the energy of the boundary, where the higher energy (0001) interface will exhibit a higher initial nucleate rate for a complexion transition, causing grains to grow abnormally large, compared to the boundaries along the  $\{11\bar{2}0\}$  interface. While recognizing these ambiguities in associating transformed boundaries with larger grains, quantification of abnormal grain growth remains the most accessible measure of the transition. The goal of this chapter attempts to quantify the occurrence of abnormally large grains along the high and low energy interfaces at a various times and temperatures.

## 7.1 Background

Traditionally, time –temperature-transformation (TTT) diagrams show the fraction of materials transformed along a thermal path. The most common use of TTT diagrams has been to map the transformation kinetics of ferrous alloys, especially for cooling. However, the concept is completely general and can be applied to the transformation from any metastable phase to an equilibrium phase, as long as the rate of transformation is slow enough to be monitored experimentally. The TTT diagram in Figure 7.1 represents the kinetics of a transformation for heating above, or cooling below, a certain equilibrium critical transition temperature,  $T_c$ . The upper half of the diagram shows the case of heating above the critical transition temperature, where the transformation occurs from the low temperature metastable phase to the higher temperature equilibrium phase. When the super heating is low, the driving force is also low and the nucleation barrier is high, making the rate of transformation low. At a high amount of super heating, both the driving force for the reaction and the rate of diffusion is greater and thus the rate of transformation is high and the time it takes to begin the transformation decreases <sup>103</sup>.

While the diagram in Figure 7.1 was meant to explain phase transformations, it is reasonable to hypothesize that grain boundary complexion transformations could exhibit the same time and temperature dependence as bulk phase transformation. However, other factors such as grain boundary energy anisotropy must not be ignored as they could potentially play a role in the nucleation barrier for the transformation (as demonstrated in Chapter 6). Therefore, it could be possible to track the rate of abnormal growth along controlled energy interfaces to determine the kinetics of complexion transformations.

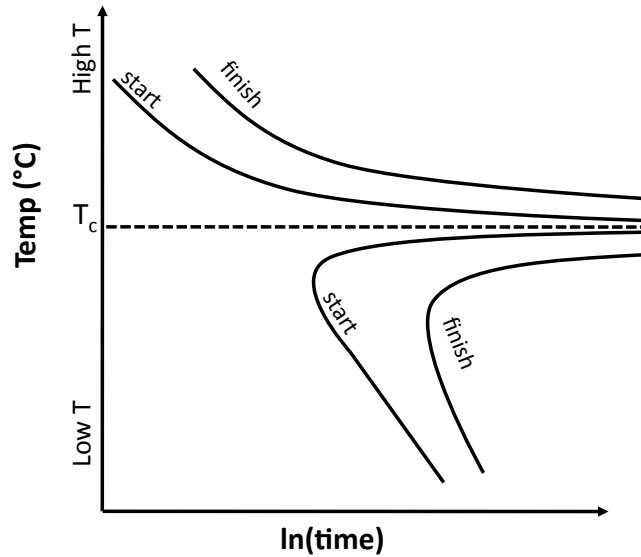


**Figure 7.1.** Schematic of time temperature transformation diagram where the lower portion of the graph represents transformation kinetics upon cooling, and the top portion represents transformation kinetics upon heating, adapted from reference (<sup>103</sup>).

A normal grain size distribution is assumed to be self-similar, and exhibits the same grain size distribution shape over time<sup>28, 104</sup>. The kinetics of normal growth can generally be modeled by equation 7.1, where  $G$  is the average size of a grain when annealed at a specific time,  $G_0$  is the average size of a grain at an initial time ( $t$ ),  $k$  is a grain growth constant, and  $n$  is a grain growth exponent which is typically around 2.

$$G^n - G_0^n = kt \quad (7.1)$$

When abnormal grain growth is present in the microstructure, a bimodal distribution occurs where the grain size distribution changes over time and often exhibits two distinct peaks. If abnormal grains begin to impinge on each other, the grain size distribution returns to normal. Many studies that focus on grain boundary complexions have looked at the grain boundary mobility of abnormal grains compared to that of normal grain growth<sup>1, 11, 59</sup>. However, these investigations do not specifically state what stipulates an abnormal grain. Theoretical treatments

of normal grain growth predict grain size distributions that have log-normal or similar distributions, with a maximum grain size not much larger than twice the mean grain size<sup>28</sup>. According to these definitions, grain size distributions that deviate significantly from log normal, or that have grains more than 2.5 times the mean grain size can be considered abnormal.

Previous work shows that the occurrence of abnormal grain growth leads to a higher population of certain grain boundary planes while decreasing the energy of the boundaries around abnormally large grains<sup>5, 6, 21, 72</sup>. It was then shown that by controlling the interfacial character by inserting a single crystal into a doped-polycrystalline matrix, it is possible to bias the grain boundary energy along that interface and potentially control where a complexion transformation is most likely to occur. The current work aims to repeat the heating experiments in Chapter 6 to test the kinetics of grain boundary complexion transitions as a function of grain boundary energy, time, and temperature for a more precise understanding of how the microstructure development occurs. Abnormal grains will be used as an indicator of a transformed boundary. As acknowledged above, this is not a certain indicator of a complexion transformation, but when coupled with measurements of the average grain boundary energy and grain boundary plane distribution, our confidence in the conclusion from grain size measures can be increased.

Dillon et al showed that the number of abnormal grains per unit area increased linearly with grain size and exponentially with temperature<sup>30</sup>. This indicates that there is a barrier to the nucleation of high mobility complexions during isothermal heating. The current work investigates the hypothesis that a complexion transformation will occur on high-energy interfaces before occurring on lower energy interfaces. Additionally, the rate of transformation of each interface will be tracked over multiple times and at various temperatures to determine if

the transformation always leads to the impingement of abnormal grains at all temperatures, or if there is a maximum number of grain boundaries that can possibly transform at any given temperature (those with a critical temperature below the annealing temperature). The results from the following experiments will ultimately give insight to the equilibrium thermodynamic and kinetic driving forces for a complexion transformation.

## 7.2 Methodology

A bulk sample with (0001) and (11 $\bar{2}$ 0) single crystals of sapphire embedded in a 500 ppm Y-doped alumina polycrystal was spark plasma sintered and further sectioned and polished, as per the methods outlined in section 3.3 and 3.4 in this document. Each of these sectioned samples was then heated to a temperature between 1450 °C and 1600 °C for times between zero and fifteen hours. Table 7.1 summarizes of all time and temperature combinations used in this experiment.

Electron Backscatter Diffraction (EBSD) was used to collect orientation images of the interface and adjacent grains. While the authors recognize that EBSD does not give the most accurate representation of grain size, it was important to know the orientation of the single crystal along which the large grains were characterized. Therefore, the images for grain size analysis used an average step size less than 0.13 times the average grain diameter. All of the EBSD data, regardless of step size, was corrected with a grain dilation of 5 pixels – indicating that the minimum grain size possible in this system could have an area of 5 pixels. This was set somewhat high, and the percent of pixels changed was not recorded because it was more important to remove false two-pixel wide “grains”. Care was taken to remove poorly indexed areas such that the dilation would not create many false grains. Corrections assigning an average orientation per grain and an average confidence index per grain were also applied, and a partition

was set so that grains with a grain average confidence index below 0.15 to 0.4 (depending on scan quality) were removed. This was done to remove indexing pseudo symmetry and grains created from the dilation step, as is discussed in Section 5.2 and reference (72).

**Table 7.1.** Grain size and transformation statistics at different times and temperatures

Temp	Time	Step	Avg GS total	GS Cutoff	Points /Grain	Avg. NGG	Avg. AGG	Total C length	Length C trans.	% C trans.	total A length	Length A trans.	% A trans.
(°C)	(hr)	(µm)	(µm)	(µm)	(pixels)	(µm)	(µm)	(µm)	(µm)	(%)	(µm)	(µm)	(%)
1500	0	2.14	0.71	1.9	7.92	0.7	2.1	100	0	0%	100	0	0%
1500	2	4.53	1.59	3.8	10.60	1.4	4.9	878	38	4%	1017	71	7%
1500	4	7.02	2.93	6.3	8.37	2.4	9.5	1808	571	32%	1449	171	12%
1500	8	6.17	4.18	5.5	13.93	2.0	11.2	1811	1075	59%	1367	236	17%
1500	12	8.07	3.22	7.5	9.20	2.6	11.0	1030	407	39%	488	137	28%
1500	15	10.11	3.80	8.0	7.60	3.3	11.2	1913	508	27%	1370	214	16%
1600	0	4.50	1.55	4.1	15.50	1.5	5.1	1028	197	19%	1163	21	2%
1600	0.5	7.50	4.04	6.8	20.20	2.5	11.3	2032	728	36%	2017	861	43%
1600	2	9.00	7.21	7.0	18.03	3.5	13.9	461	246	53%	343	33	10%
1600	4	9.50	8.61	8.5	10.76	5.0	13.5	671	434	65%	739	154	21%
1600	8	10.00	8.84	8.5	11.05	5.1	13.8	542	313	58%	452	247	55%

By visually inspecting the microstructures of the annealed Y-doped alumina samples, it was clear that some grains were much larger than others. However, there did not seem to be a distinct grain size cut off with which an abnormal grain could be easily defined. Figure 7.2 shows EBSD images displaying varying degrees of abnormal growth, and how the cutoff parameter applied to the average grain size (including both abnormal and normal grains) affects what is called an abnormal grain. In the case of the 1500 °C heated for 0 hours – where the sample was brought to temperature and immediately cooled, by visual inspection, one would say that a few grains look somewhat large, but nothing abnormal. When a partition of three times the average grain size was applied, the three largest grains were removed from the distribution. No grains changed partition until the cut off was 2.6 times the average grain diameter, and more grains were removed. In this sample, a grain cutoff of 2.7 would be acceptable to determine abnormally large grains. However, when a sample was heated to times and temperatures that exhibit a more significant bimodal grain size distribution (1600 °C – 0 hours and 1500 °C – 2 hours), there is a steady increase in the number of grains that were labeled abnormal with

decreasing cutoff parameter. In the 1500 °C sample sintered for 2 hours, it is evident that with every decreasing cutoff for abnormal grains, a different subset of grains is placed in the abnormal partition. From this analysis, we can conclude that there is no perfect cutoff parameter for partitioning the grains into a normal and abnormal distribution. Additionally, this gives interesting insights into the nucleation mechanism for complexion transformations in the Y-doped alumina system – which will be discussed in a Section 7.4.

The method used for quantification of abnormal grain growth both in the bulk and at the single crystal interfaces in this experiment is a combination of qualitative and quantitative techniques. Using the TSL software<sup>88</sup>, a data partition was set to remove all large grains as well as the single crystal interface from the scans. Personal judgment was used to determine what exactly constituted an abnormally large grain. The average grain size of the partitioned smaller or normal grains was then determined. With knowledge of this value, a partition of 2.7 times the average normal grain size was used and the average normal grain size was recalculated and adjusted. This method was iterated until the partition was 2.7 times the average normal grain size. In the case where there were some small grains, but the overall population of grains were clearly impinged large grains; the normal grain size cutoff was estimated by extrapolating data from the un-impinged microstructures heated for shorter times. At temperatures well above the critical transformation temperature, it is expected that the rate of grain growth would decrease with both increasing impingement and increasing solute drag<sup>29</sup>. In these cases, namely the samples sintered at 1600 °C for 2, 4 and 8 hours, the abnormal grain size cutoff was less than 2.7 times the average.

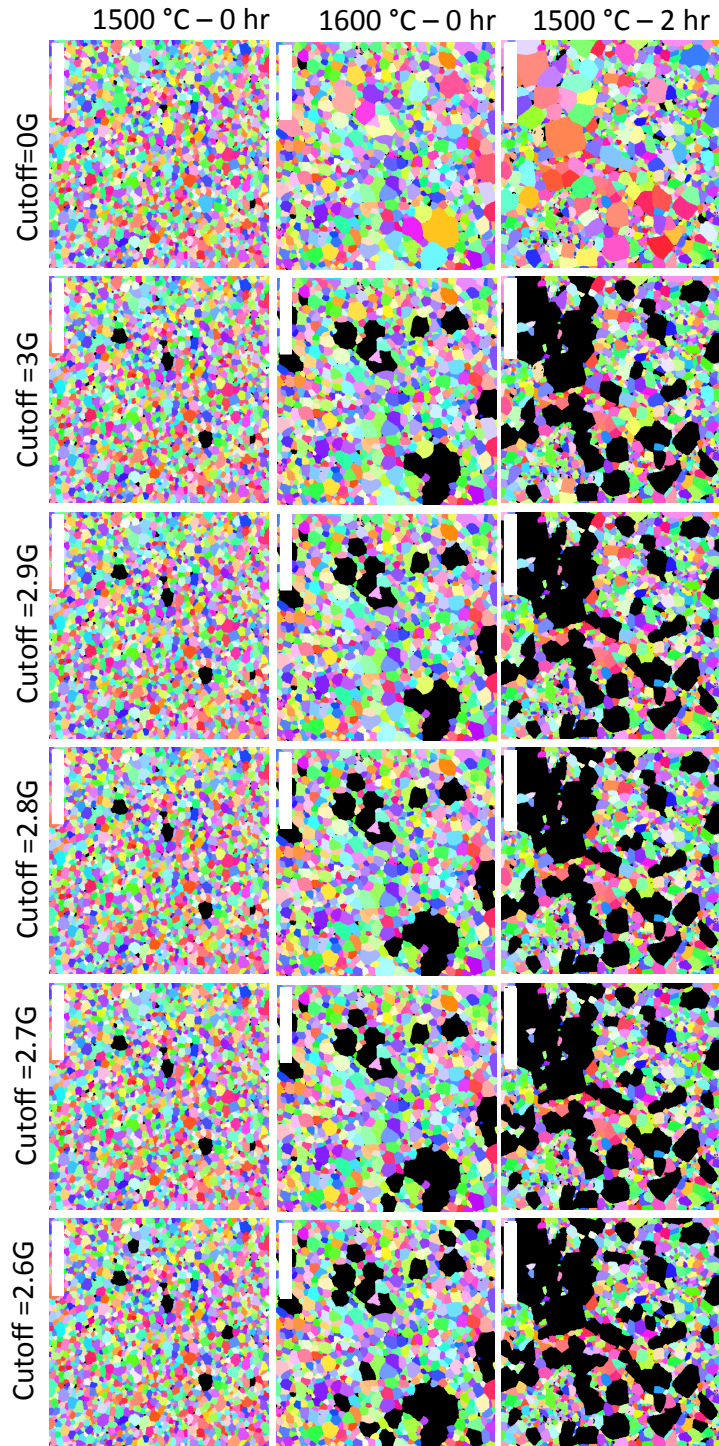


**Figure 7.2.** Representative orientation maps from EBSD data for a unimodal microstructure (1500 – 0 hr) a bimodal microstructure (1600 – 0 hr), and a microstructure displaying significant abnormal grain growth (1500 – 2 hr). Each of the following rows represents a cutoff parameter that is multiplied by the average grain size of the microstructure ( $G$ ). Scale bars are 10  $\mu\text{m}$  (1500 – 0 hr), 15  $\mu\text{m}$  (1600 – 0 hr), and 50  $\mu\text{m}$  (1500 – 2 hr).

After the initial cutoff determining plausible abnormal grain sizes, the full, cleaned data sets were re-partitioned such that the abnormal grains and single-crystal interface could be seen and the normal grains were removed. Due to the qualitative nature of the initial abnormal grain partition, a cutoff parameter of 3 times the average normal grain size was used. This assured that the abnormal grains were truly larger than the normal grains. Using the TSL software, a line was drawn down the entire length of the partitioned single crystal. While the straight line is slightly shorter than the true, meandering interface, all interfaces were treated in the same way and any related uncertainty would affect all of the interfaces in the same way. In the case that the single crystal interface had advanced much further than a few grain sizes into the matrix, multiple line lengths were combined to determine the total length of the interface. Lines were then manually drawn between triple points of abnormal grains that were connected to each interface. The total length of all of the boundaries between an abnormal grain and the single crystal was divided by the total length of the single crystal to determine a percent interface transformed. This worked well in the cases where there was a clear bimodal distribution. However, after the large grains began to impinge on each other leading to a normal distribution with a much larger grain size, it was evident that even with the extrapolated normal grain size, an accurate representation of impinged abnormal grains could not be determined. An example of the grain size partition steps and corresponding microstructures can be seen in Figure 7.3.

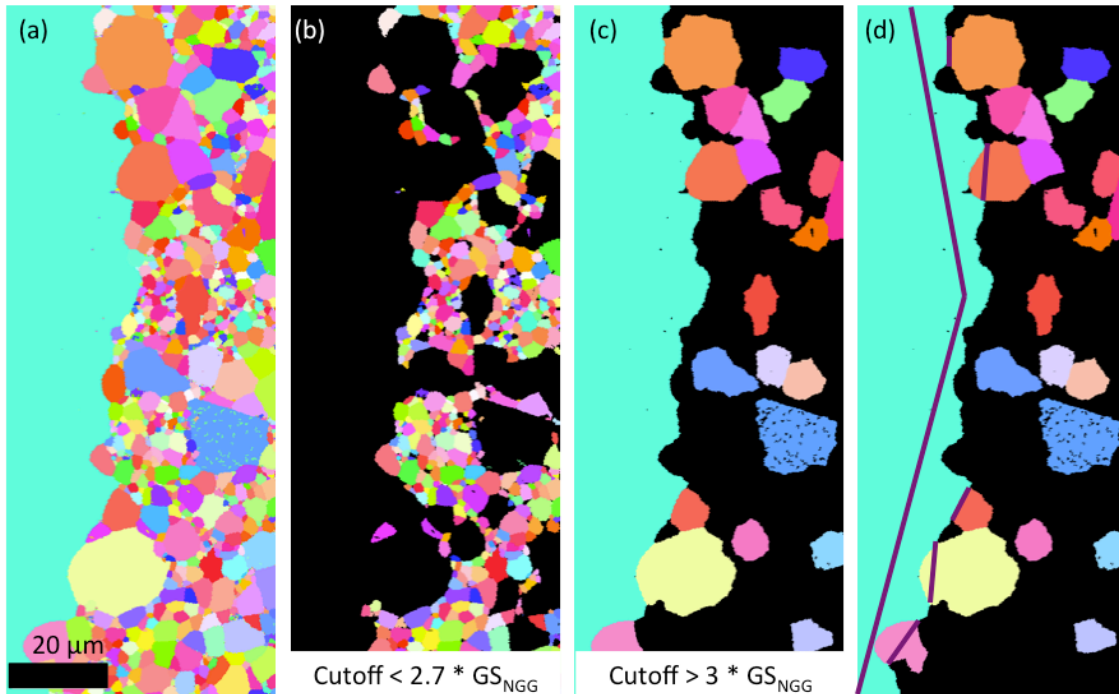


**Figure 7.3.** Method of quantifying abnormal grain growth using an EBSD image along a single crystal interface (a). First, a partition is set to filter out grains that are greater than 2.7 times the normal grain size (b). The first partition is removed, and a second is set such that all grains that are greater than 3 times the normal grain size are shown (c). Finally, the total length of the single crystal interface and the length of the single crystal interface that is in contact with abnormal grains were measured.

### 7.3 Results

Representative EBSD images of the (0001) and  $(1\bar{1}\bar{2}0)$  interfaces and corresponding abnormal and normal grain partitions set at 3 times the normal grain size for the 1500 – 2 hour, 1600 – 0 hour, and 1600 – 4 hour Y-doped alumina samples can be seen in Figure 7.4 a – d respectively. The 1500 – 8 hour sample can also be seen in Chapter 6 Figure 6.1. One point that further exemplifies the difficulty of differentiating normal and abnormal grains can be seen in Figure 7.4 a, where there is a very obviously bimodal distribution along the (0001) (red) interface, but the grains along the  $(1\bar{1}\bar{2}0)$  interface are all significantly larger than the normal grains along the (0001) interface. Because of the mesoscale nature of this analysis it is not possible to determine if the grains along the  $(1\bar{1}\bar{2}0)$  interface have transformed, however this would be a reasonable conclusion based on the fact that they grew much larger than the grains

along (0001). In Figure 7.4 b it is clear that there are much larger grains along the (0001) interface and barely any along the  $(11\bar{2}0)$  interface. Finally in Figure 7.4 c, the sample that was heated to 1600 °C for 4 hours was almost completely impinged, however the grains along the  $(11\bar{2}0)$  interface were significantly smaller than the average extrapolated normal grain size. From these results we can see that the area fraction of abnormal grains is variable with time and temperature, and can go forth from now on assuming that this abnormal growth is dependent on a complexion transition and not nucleation-limited coarsening.

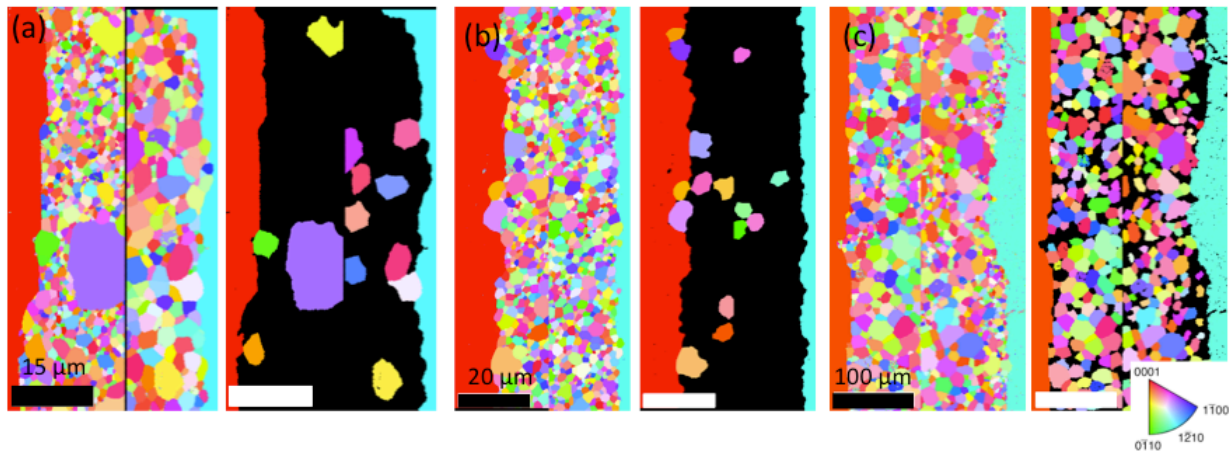


**Figure 7.4.** EBSD images showing the crystal orientation perpendicular to the single crystal interface ([010] sample direction) for the samples heated at 1500 °C for 2 hours (a), 1600 °C for 0 hours (b), and 1600 °C for 4 hours (c). The red single crystal represents the (0001) interface and the blue/green single crystal represents the  $(11\bar{2}0)$  interface. In each set, the pair of interfaces to the left is the complete, un-partitioned EBSD image and the pair of interfaces to the right is the EBSD map that is partitioned such that grains only three times the average grain diameter are shown.

The average total, normal, and abnormal grain sizes are graphed as a function of time for both temperature ranges in Figure 7.5. It was found in both the samples sintered at 1500 °C and 1600 °C that the average normal grain size does not increase significantly with temperature, as was also seen in previous results<sup>59</sup>, while the average abnormal grain size increased until an

approximate maximum was reached. The total average grain size (including both normal and abnormal grains) also increases with temperature. The numerical results are listed in Table 7.1.

The sizes of the abnormal grains in the 1500 °C series (Figure 7.5 a) increase with increasing time, and the abnormal grain size begins to level off at 8 hours, indicating impingement. The normal grain size also increases, but at a lesser rate, and the average total grain size also increases with time and deviates from the normal grain size. Because the average total grain size is not within uncertainty of the abnormal grain size, it is assumed that this transformation did not go to completion - this will be further discussed in the following paragraphs.

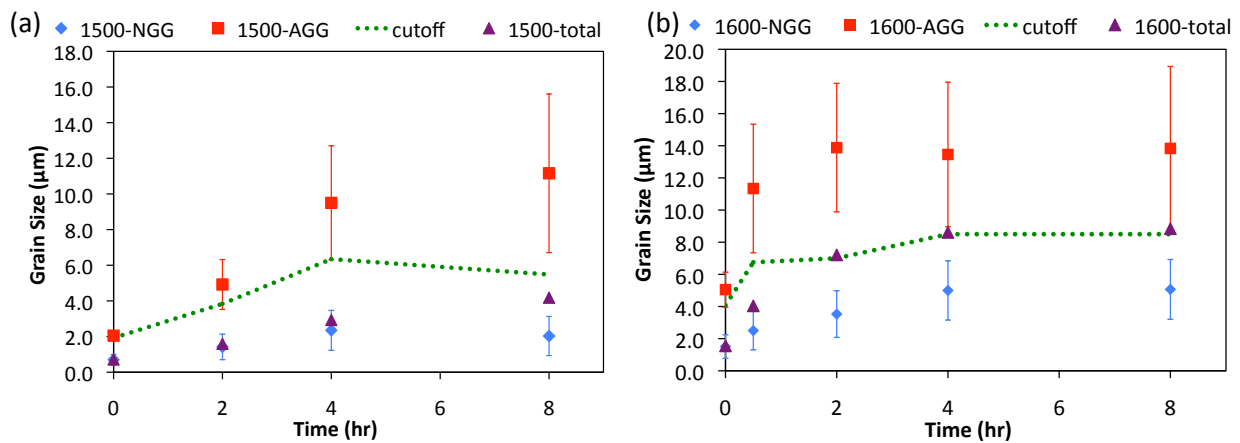


**Figure 7.5.** The grain size as a function of time for the samples annealed at 1500 °C (a) and samples annealed at 1600 °C (b). The red squares represent the average abnormal grain size, the blue diamonds represent the average normal grain size, the purple triangles represent the average total grain size, and the dashed green line represents the cutoff parameter that stipulated an abnormal grain.

The abnormal grains in the 1600 °C series (Figure 7.5 b) reach a constant maximum grain size because, after they impinge, they do not continue to grow at the same rate. In these samples, the normal grains were indistinguishable from the impinged abnormal grains, so a normal grain size was extrapolated from the previous, un-impinged measurements. The average total grain size increases with increasing time from the approximate normal grain size in the 0 hour sample

to, within the uncertainty, the size of the abnormal grains in the sample that was heated for 8 hours. This indicates that the number of abnormal grains increases with time.

To illustrate the need for a variable partition between the normal and abnormal grains, the area-weighted grain size distributions were also plotted for both the 1500 °C and 1600 °C series in Figure 7.6. In these graphs, the X-axes represent the grain diameter binned in 1  $\mu\text{m}$  increments and the Y-axes represent the normalized average area of each bin. In the 1500 °C series (Fig 7.6 a-d), the 1500 °C – 0 hour sample has a narrow grain size distribution, and the 1500 °C – 2 hour sample exhibits a slight increase in grains above a 10  $\mu\text{m}$  diameter. It should be noted that the apparent difference in the average normal grain size along the different planes in the 1500 °C – 2 hour sample that was exhibited in Figure 7.4 fell within a normal distribution curve. The 1500 °C – 4 and 8 hour samples have the signatures of a bimodal distribution. The maximum grain size in the 1500 °C cases is 35  $\mu\text{m}$ .

The 1600 °C series of grain area verses grain diameter distributions are plotted in Figure 7.6 f-j. The 1600 °C sample sintered at 0 hours already has characteristics of a bimodal distribution where some grains are already about 9  $\mu\text{m}$ . The 1600 °C samples annealed at 0.5 and 2 hours exhibit increasingly bimodal distributions while the samples annealed for 4 and 8 hours both exhibit a normal distribution of impinged large grains. The maximum grain size in the 1600 °C cases is 40  $\mu\text{m}$

A sample was also heated to 1450 °C for 15 hours, and the grain size distribution is plotted in Figure 7.6 e. In this sample, there were very few abnormal grains, and the grains that were abnormal were not typically found along either interface. Additionally, the largest grain found in the 1450 °C distribution was 44  $\mu\text{m}$ , which is larger than both the 1600 °C and 1500 °C maximum grain sizes.

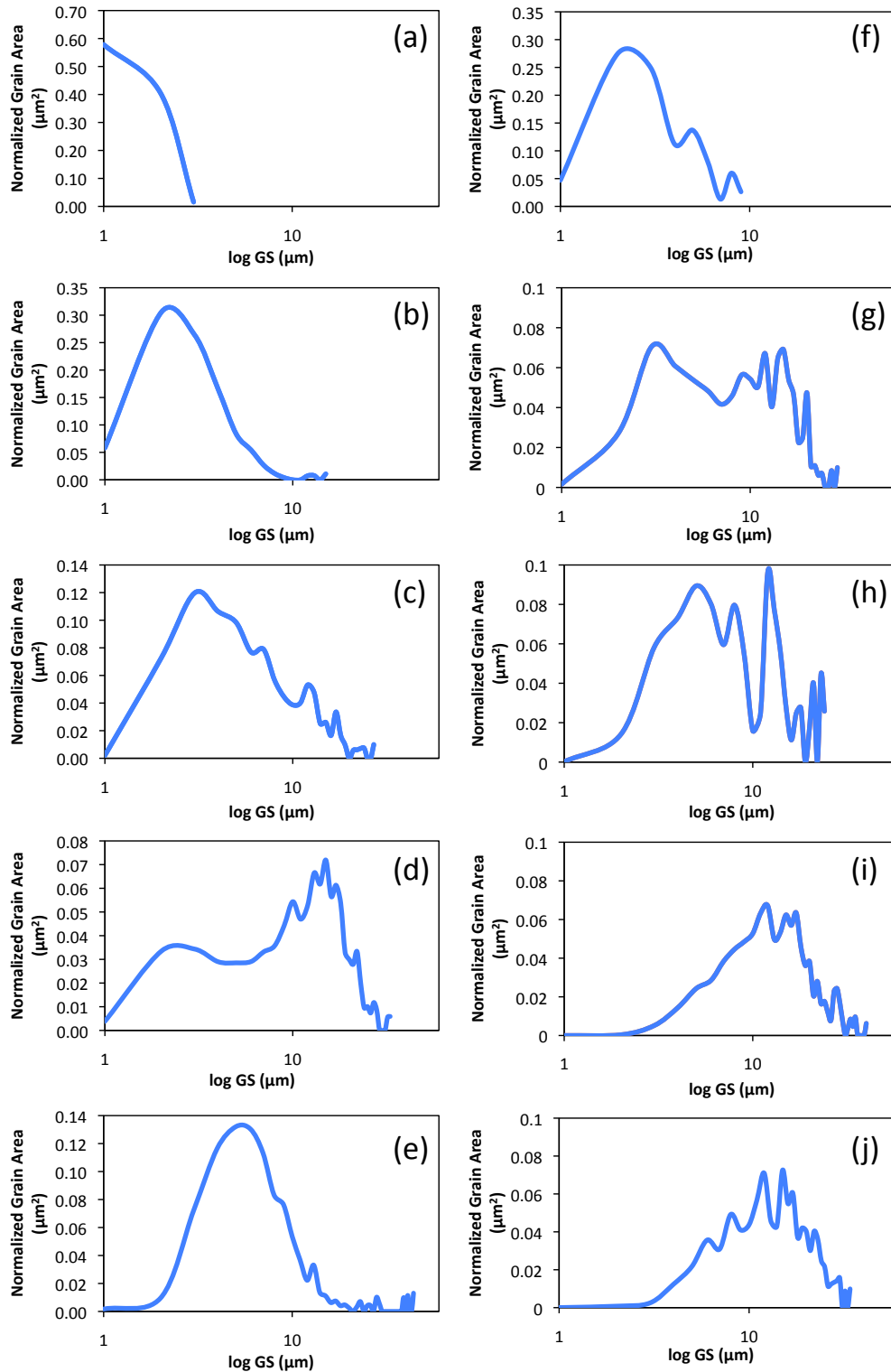


**Figure 7.6.** The average normalized grain area versus log of grain diameter for samples sintered at 1500 °C for 0 hours (a), 2 hours (b), 4 hours (c), and 8 hours (d), 1450 °C for 15 hours (e) and at 1600 °C for 0 hours (f), 0.5 hours (g), 2 hours (h), 4 hours (i), and 8 hours (j). The graphs were normalized such that the total area under each plot is one.

The percentage of the (0001)/C-plane and  $(11\bar{2}0)$ /A-plane interfaces that are in contact with grains three times the average normal grain size is plotted in Figure 7.7. These results indicate that, in general, there are more abnormally large grains along the higher energy (0001) interface than the lower energy  $(11\bar{2}0)$  interface; this is in agreement with the results from Chapter 6. The 1600 °C sample heated for 8 hours consists of large impinged grains that have a normal distribution of sizes – therefore the two single crystal interfaces are essentially the same. The only two samples that did not follow the same trend as the others are the 1600 °C sample heated for 0.5 hours and the 1500 °C sample heated for 2 hours. However, the absolute differences are not large and the difficulty of quantifying the number of abnormal grains in the sample heated at 1500 °C for 2 hours (see Figure 7.3 a) have already been discussed. The difference between the percent of the C-plane that was transformed to that of the A-plane that was transformed is indicated above the bars for each time and temperature.

#### **7.4 Discussion**

The current work tests the hypothesis that there is a nucleation barrier for a complexion transformation, and that this barrier depends on both thermodynamic parameters as well as the energy of the specific grain boundary. It was proposed that complexion transformations exhibit kinetics that are similar to bulk phase transformations, where the transformation rate is nucleation rather than diffusion limited. The current experiment has tracked the changes in grain size with time and temperature along energetically biased interfaces intentionally introduced during the synthesis, so that abnormal grains can be used as indicators for a grain boundary complexion transformation.

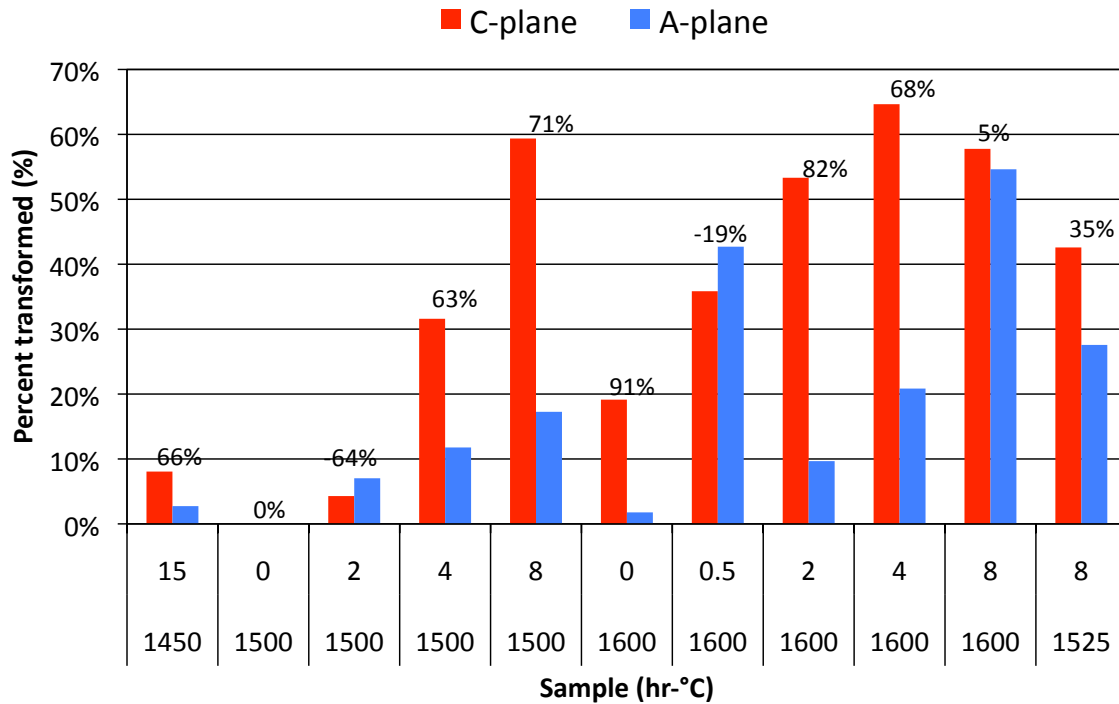


**Figure 7.7.** The percent of the (0001)/C-plane (red) and  $(1\bar{1}\bar{2}0)$ /A-plane (blue) single crystal interfaces that are in contact with abnormal grains 3 times the average normal grain size. Each group of bars is a single anneal time and temperature combination. The numbers above the bars indicate the percent difference of the percent of the C-plane transformed to the percent of the A-plane transformed.

One defining feature for the bulk transformation theory is that the entire phase is uniformly metastable and the driving force for the transformation is constant at constant temperature. In the current work, the transformation is assumed to be complete when the starting microstructure is overgrown completely by faster growing and much larger grains. The 1600 °C samples sintered at 4 and 8 hours display such a distribution, and it can be said that at 1600 °C, the abnormal grains fully impinge in the microstructure. This has also been seen previously in Y-doped alumina sintered at 1600 °C<sup>72</sup>. However, in both the 1450 °C sample heated for 15 hours and the 1500 °C sample heated for 8 hours, there are still a significant number of normal grains. Therefore, at least for the tested times, there is not sufficient evidence to support the claim that once a critical complexion transformation temperature is surpassed, all grain

boundaries will eventually nucleate and abnormal grain growth will proceed to completion. Instead the limiting factor controlling the number of abnormal grains seems to be the grain boundary energy anisotropy of the system. Where the grain boundary energy will determine the height of the nucleation barrier for a complexion transition, and thus the critical nucleation temperature above which the boundary is metastable.

The results suggest that the kinetics of a grain boundary complexion transformation, when the entire grain boundary population is considered as a whole, are not analogous to the kinetics of a bulk phase transformation because there is not one temperature above which all grain boundaries will nucleate transformations. Instead the total number of metastable boundaries, or boundaries that are able to transform, at any temperature will be determined by the distribution of grain boundary energies and associated critical nucleation temperatures. On the other hand, if one considered only a single type of grain boundary with a single transformation temperature, then the analogy would be more accurate. Because grain boundaries with lower energies have high critical temperatures for the transformation, it cannot be assumed that every grain boundary is metastable at a given temperature. Instead, the transformation appears to be a character and temperature-dependent nucleation-limited phenomenon, with the kinetics being faster at higher energy boundaries. In the current experiment, this was tested by controlling the bulk chemistry, temperature, and grain boundary character of the yttrium-doped alumina system, and recording the percent of the interface covered by abnormal grains that appear at different times. It was found that a higher fraction of the higher energy (0001) or C-plane interface was in contact with large grains, while the lower energy ( $11\bar{2}0$ ) or A-plane usually had fewer abnormal grains along its interface, as seen in Figure 7.7.

Dillon and Harmer's results showed a linear dependence of abnormal grains per area fraction with increasing time. In the current work, the fraction of single crystal interface that is in contact with an abnormal grain can be used as a proxy for the fraction of a transformed boundary. Figure 7.8 a shows the percent of each single crystal interface that is transformed verses time. The fraction of transformed interface increased with increasing time, and exhibited a nearly linear relationship. However, if the transformation rate is dependent on the grain boundary energy distribution, then the trend does not necessarily have to be linear. Also, from this data, a direct parallel cannot be drawn to bulk phase transformations since the nucleation of a complexion transformation does not immediately correlate with the presence of an abnormal grain, and because the beginning of the complexion transformation cannot be accurately established simply by monitoring grain size distributions.

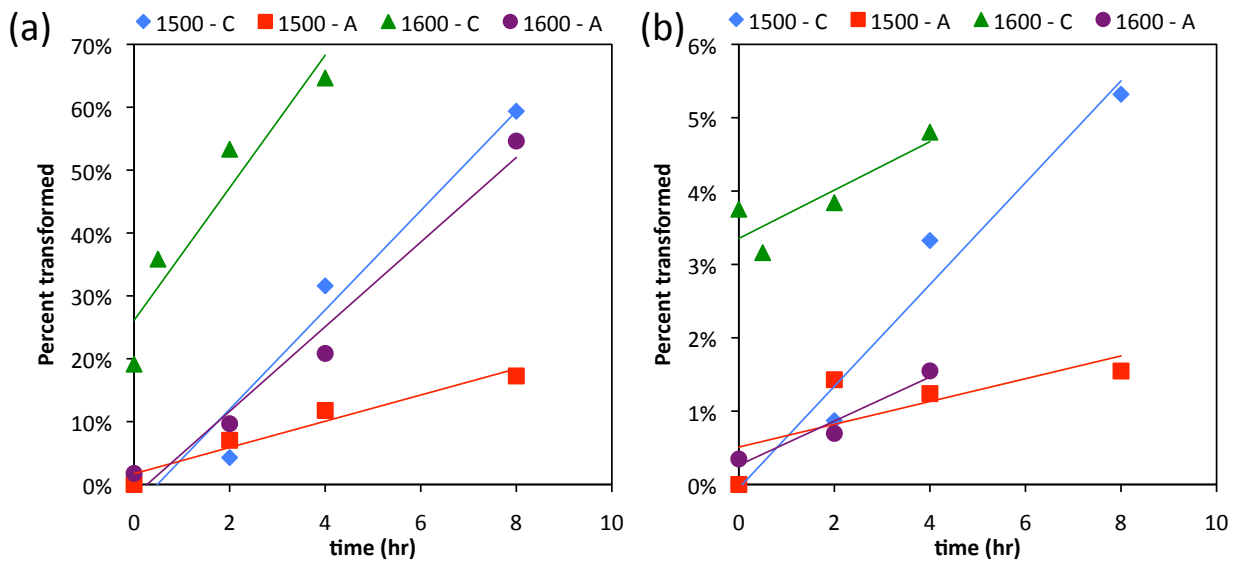


**Figure 7.8.** The percent of the C/(0001) plane single crystal interface that is adjacent to an abnormal grain when sintered at 1500 °C (blue diamond), A/(11 $\bar{2}$ 0) plane when sintered at 1500 °C (red square), C-plane when sintered at 1600 °C (green triangle), and A-plane sintered at 1600 °C (purple circle). Graph (a) represents the directly measured percent transformed against time while graph (b) represents the percent transformed normalized by the average abnormal grain size at the given time and temperature against time.

Another interesting aspect of comparing the percent transformed for both the high and low energy interfaces at various times and temperatures is the ability to compare the rate at which abnormal grains are appearing (represented by the slope of the best fit lines in Figure 7.8a). The rate of transformation is greater for the higher energy (0001) interfaces at both temperatures, where at 1600 °C the C-plane exhibits a 10% increase in transformed interface area per hour, while at 1500 °C the C-plane exhibits an 8% increase per hour. At 1600 °C the A-plane exhibits a similar transformation rate of 7% per hour, and at 1500 °C the A-plane only exhibits an approximate 2 % additional transformation per hour.

It should be noted, however, that the rate of transformation does not account for the increase in abnormal grain size with temperature. It is also possible to compare the apparent nucleation rate of complexion transitions along both the high and low energy interfaces by normalizing the percent transformed by the average abnormal grain diameter, where the approximate nucleation rate of a complexion transition will be represented by the slope of the best fit lines in figure 7.8b. At 1500 °C, the nucleation rate along the higher energy (0001) interface was 0.69 %/ $\mu\text{m-h}$  while the nucleation rate along the lower energy ( $11\bar{2}0$ ) interface was 0.16 %/ $\mu\text{m-h}$ . This indicates that the grain boundary energy distribution may determine the nucleation rate for complexion transitions. At 1600 °C, the nucleation rate along both the (0001) and ( $11\bar{2}0$ ) interfaces are approximately the same at 0.33 %/ $\mu\text{m-h}$  and 0.30 %/ $\mu\text{m-h}$  respectively. However the high energy (0001) interface of the sample that was held at 1600 °C for zero hours exhibited an initial abnormal grain coverage of 3.8 %/ $\mu\text{m}$ , which is 91% higher than the initial lower energy ( $11\bar{2}0$ ) coverage (0.3 %/ $\mu\text{m}$ ). These results imply that there was an extremely high nucleation rate for complexion transitions along the (0001) interface, such that in the twenty minutes that the sample was above 1450 °C, significant abnormal grain growth had already

occurred. This is further evidence that the distribution of grain boundary energies will determine the rate of the nucleation of complexion transitions. It should still be noted that the sample that was annealed at 1600 °C for 0.5 hours does not agree with this conclusion. However, conclusions are drawn from the majority of the observations instead of the outlier.

To test the idea that only a set number of grain boundaries will be metastable at a given temperature, a sample was held near the critical complexion transformation temperature, at 1450 °C, for 15 hours. Because of the small degree of super heating, only a few abnormal grains grew. However, the maximum size of these grains was 44 μm which is greater than the maximum observed grain size for the 1500 °C series (35 μm) and 1600 °C series (40 μm). This implies that, because the grains are not completely impinged in the 1450 °C sample, the abnormally large grains can keep growing. The limited number of abnormal grains, the largest of which are not present along either the (0001) or (11 $\bar{2}$ 0) interfaces, indicates that there is a strong temperature dependence for the nucleation of a complexion transformation and only a small number of high energy boundaries are metastable at 1450 °C. The abnormal grains exhibit a size distribution, as is also seen in all of the other samples that exhibit abnormal grain growth. This indicates that there may have been a heterogeneous nucleation of the complexion transformation, which result in varying coarse grain sizes over time. However, this distribution in size may also be due to the two-dimensional stereological sampling of a three-dimensional microstructure. Dillon and Harmer proposed that there were a critical number of complexion transformations that needed to nucleate, causing abnormal grain growth so that the entire microstructure would become impinged<sup>29</sup>. This seems to be consistent in the current experiments.

From these results, the authors now propose that the number of metastable boundaries is dependent on the temperature of the system; therefore at higher temperatures, more boundaries are metastable and able to transform. If a boundary is not metastable, it will not have the ability to overcome the nucleation barrier to transform to the high temperature complexion. The rate of the transformation is determined by the degree of super heating above the critical temperature needed to overcome the nucleation barrier for an individual boundary- determined by the grain boundary energy. In a way, this is analogous to heterogeneous nucleation of a second phase, however because there is a range of grain boundary transformation temperatures, we cannot compare the rate of a complexion transformation throughout the entire microstructure to that of a bulk phase transformation.

A grain boundary transformation schematic can be seen in Figure 7.9, where Figure 7.9 a shows representative grain boundary energy distribution curves with varying grain boundary energy anisotropy. Figure 7.9 b shows a modified version of a TTT diagram, where the limiting lines that usually represent the percent of the material that undergoes a transformation are now changed to represent the grain boundary energy needed to nucleate a complexion transformation. In this diagram, at low temperatures, close to the minimum critical transformation temperature ( $T_c^{\min}$ ) only the grain boundaries with the highest energies are able to transform. The number of metastable boundaries that are able to transform increases until the maximum critical transformation temperature ( $T_c^{\max}$ ) after which all of the boundaries will be metastable and able to transform. At any given temperature, the rate of transformation will still be dependent on the grain boundary energy anisotropy of the boundaries that are available for transformation.

If a grain boundary energy distribution exhibits many high-energy grain boundaries – such as those experimentally measured along the (0001) plane in Chapter 6 and represented as

the red line in Figure 7.9a. Then it could be possible that the initial rate of transformation along that high energy interface would be greater than a distribution that exhibits many lower energy grain boundaries, like the  $(11\bar{2}0)$  plane in Chapter 6 represented by the blue line in Figure 7.9 a.

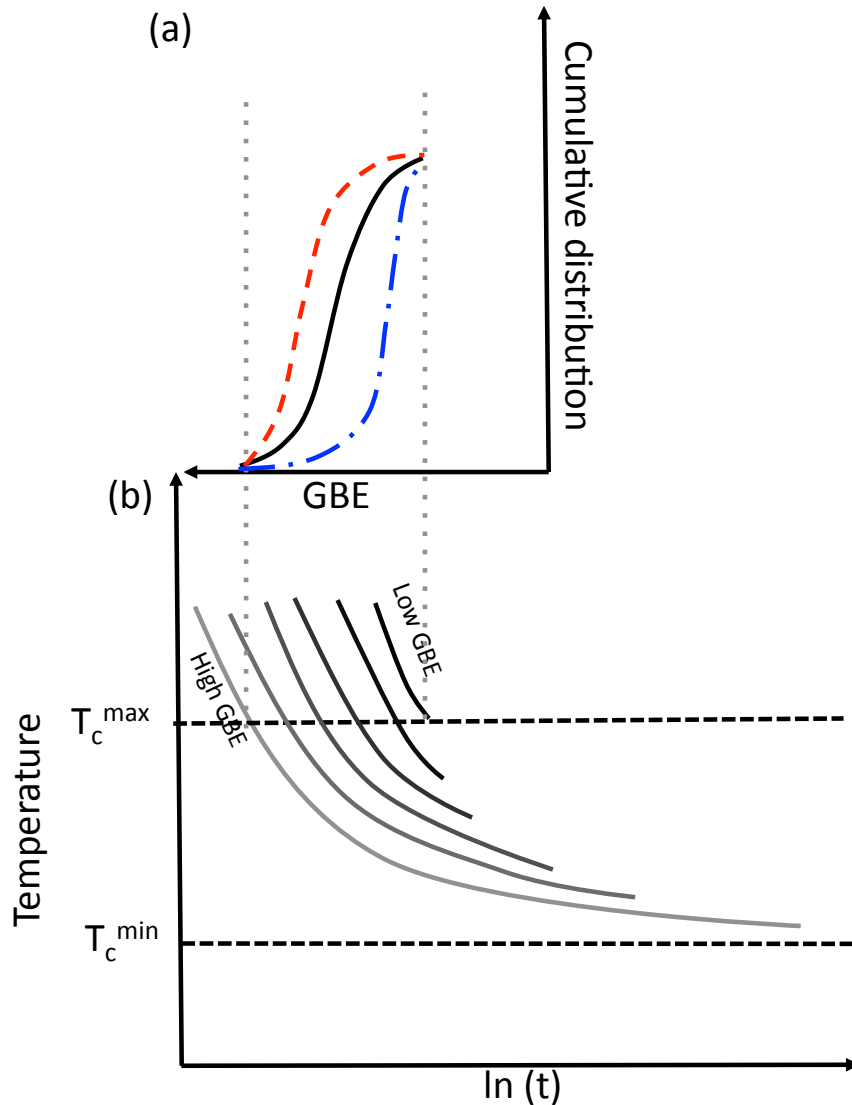


**Figure 7.9.** Representative grain boundary energy distribution showing a normal (solid black line), high (dashed red line), and low (unevenly dashed blue line) energy distributions (a) which correspond to the degree of transformation curve in the TTT diagram (b). Where the number of boundaries that are metastable and thus able to transform at a given temperature are dependent on the grain boundary energy needed at the given temperature to overcome the nucleation barrier for a complexion transformation and the rate of the transformation is dependent on the grain boundary energy anisotropy.

Finally, there have not been any experiments to test if there is an effect of the electric field (current direction) in the spark plasma sintering system on the evolution of these microstructures containing single crystals. Research on the effect of SPS in alumina has shown that there is no field effect on the grain morphology or apparent properties<sup>62, 64, 65</sup>. However, the effect that the applied DC current and induced electric field has on non-conductive samples is not completely understood. Grain size gradients that appear similar to the morphology of the current experiments have been observed in ZnO<sup>105</sup>, and other unexplained morphologies have been observed. Because of this, the authors decided to make an additional 500 ppm Y-doped alumina sample that was SPS'ed with the (0001) and (1 $\bar{1}\bar{2}$ 0) planes reversed from Figure 3.1, where the (1 $\bar{1}\bar{2}$ 0)/A-plane was on the bottom. This bulk sample was prepared according to the previous procedures, annealed at 1525 °C for 8 hours, and the amount of abnormal grains along the interface were observed and can be seen in Figure 7.10. It was found that the C-plane exhibited 35 % more abnormal grains than the A-plane, this is in agreement with the majority of the previous results. From this result we can say that the electric field from the SPS procedure does not have a significant effect on the alumina grain morphology when interfaced with sapphire single crystals that are laid perpendicular to the direction of current flow.

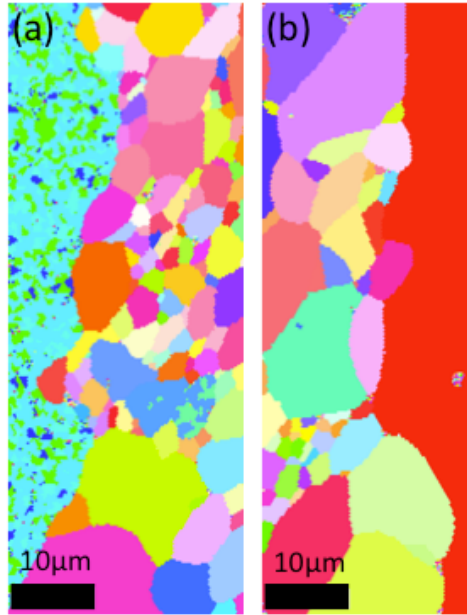


**Figure 7.10.** Orientation maps down the [010] sample direction of the A-plane (a) and C-plane (b) interfaces of the sample used to test the effect of the electric field on the grain morphology.

### 7.5 Conclusions

The current experiment has shown that by controlling the processing temperature and interfacial energy in Y-doped alumina, it is possible to control the rate at which a complexion transformation will occur. Grain boundary energy anisotropy will vary the number of boundaries that can transform at a given temperature. At most annealing temperatures and times, the higher energy (0001) interface exhibited more abnormal grains than the  $(11\bar{2}0)$  interface. The nucleation rate of a complexion transformation along each interface - as indicated by the normalized line fraction of abnormal grains along the single crystal - was greater for the (0001) interfaces than for the  $(11\bar{2}0)$  interfaces. Finally, there was no apparent field effect with the spark plasma sintering method for the sample geometry.

## 8. Experiment V: Temperature dependence of relative grain boundary energy in Y-doped alumina

Understanding mesoscale properties, such as grain boundary energy, in terms of thermodynamic state variables is an important aspect of grain boundary engineering. Investigating the relationship between grain boundary energy and temperature, especially in temperature regimes where there are complexion transitions, will provide insight into the processing conditions that could be used to maintain a microstructure with a uniform grain size distribution and constant properties. Yttria doping in alumina, for example, can be used to maintain a dense, fine-grained, creep resistant microstructure<sup>25, 77, 82</sup>. However, it has been found that when yttria doped alumina is heated at higher temperatures, above 1450 °C, abnormal grain growth occurs resulting in a high level of porosity and decreased creep resistance<sup>59, 72</sup>. The current work describes a method to measure grain boundary energy in yttrium-doped alumina as a function of temperature and uses the results as a means to explain the thermodynamic driving forces behind grain boundary complexion transitions and second phase precipitation.

### 8.1 Background

The interfacial or grain boundary energy of a pure material is known to decrease with temperature; this is due to the entropic contribution to the free energy of the interface<sup>106,107</sup>. However, when a solute or impurity is added to the pure material, the interfacial energy decreases and the activation energy for interface diffusion increases<sup>107-109</sup>. This was theoretically derived by Hondoras et al. using the Gibb's absorption equation<sup>110, 111</sup>. However, when the temperature in an impure system increases the interfacial energy will also increase, this occurs because the large negative enthalpy of segregation more than counterbalances the positive entropy of pure grain boundaries. These two opposite effects will be explained in more detail in

the Section 8.4 of this chapter. The change in grain boundary energy with temperature has previously been measured in both metals and ceramics using two experimental approaches. The first experiment uses radioactive tracers to determine diffusion in both the lattice and along the grain boundary of a material at various temperatures, where the ratio of diffusion coefficients can be related to the interfacial energy of the boundaries. The second method measures the grain boundary to surface energy ratio by measuring the thermal groove dihedral angle of grain boundaries when the groove is formed at different temperatures<sup>107–109</sup>. The current work measures the grain boundary energy as a function of temperature in an impure system using thermal groove dihedral angle analysis. These measurements will be conducted over a temperature range that is known to exhibit abnormal grain growth in the yttria-doped alumina system.

In the previous investigations presented in this document, the presence of a second phase was often ignored. However, in almost all of the systems that exhibit abnormal grain growth caused by a complexion transition, a second phase precipitates. Dillon et al<sup>30</sup> investigated the relative energies of interfaces between a second phase and alumina to that of the undoped alumina grain boundaries, and compared the energies to the likelihood of a complexion transformation as opposed to a phase precipitation in doped alumina. Overall he found that low-energy inter phase interfaces often suppresses complexion transitions and vice versa. Therefore, in any system above its effective solubility limit, there will be a thermodynamic competition between second phase precipitation and a transition to a more disordered complexion. In the case of alumina interfaced with YAG ( $Y_3Al_5O_{12}$ ), Dillon's results indicated that the energy of alumina and YAG interphase boundaries is about the same as the grain boundary energy between

alumina and alumina – this indicates that yttria-doped alumina should not strongly favor complexion transitions over precipitation<sup>30</sup>.

Recent work on doped ceramics has shown that a change from a metastable to equilibrium grain boundary complexion at a specific temperature, interfacial character, and chemical composition can lead to a significant difference in grain boundary energy when comparing the transformed boundaries to the untransformed boundaries<sup>6, 14, 21, 112</sup>. For example, in yttria doped alumina, the mean relative grain boundary energy of transformed grain boundaries – as indicated by the abnormal grain size when compared to the majority matrix grains – was 46% lower than the grain boundaries around smaller grains immediately adjacent to the abnormal grains<sup>6</sup>. This decrease in average energy corresponds to an increase in the population of  $\{1\bar{1}02\}$  and  $\{1\bar{1}\bar{2}0\}$  boundary planes and a minimum population of (0001) planes<sup>72</sup>. Previous work has shown that the population of grain boundary planes is inversely proportional to the grain boundary energy<sup>32, 42</sup>. This indicates that the  $\{1\bar{1}02\}$  and  $\{1\bar{1}\bar{2}0\}$  planes are the lowest energy while the (0001) planes are the highest energy. Additional work on Y-doped alumina (previously described in Chapter 6 and 7 of this document) has shown that the high energy interface is more likely to nucleate a complexion transition resulting in abnormal grain growth than the low energy interface. This indicates that nucleation barriers for a complexion transition are dependent on grain boundary character and energy, where high-energy boundaries have a lower nucleation barrier for the transformation from a metastable to equilibrium grain boundary complexion compared to lower energy boundaries.

Previous investigations looking at the changes of grain boundary energy with complexion transitions heated the samples to a transition temperature, polished the annealed samples, and then thermally grooved the samples at temperatures less than the transition<sup>14, 21</sup>. While it was not

assumed that the high-temperature grain boundary structure was preserved with the low temperature grooving, it was assumed that the corresponding grain boundary character and energy differences between the transformed and untransformed boundaries would not depend on the grooving temperature. The present work explored this by taking the highest temperature, fully transformed sample heated to 1650 °C and polishing and re-grooving at decreasing temperatures.

The current work uses grain boundary thermal groove dihedral angle analysis to investigate the temperature dependence of grain boundary energies in yttrium-doped alumina through a temperature range at which a complexion transition will occur. This will give insight into the thermodynamic considerations for both the formation of a grain boundary complexion compared to the nucleation of a second phase.

## **8.2 Methodology**

Pure alumina was nominally doped with 100 and 500 ppm yttrium using standard powder processing procedures that have been previously described in Chapter 2 of this document. In summary, the yttrium nitrate precursor was mixed with the alumina powder in methanol, evaporated, and spark plasma sintered at 1250 °C and 50 MPa. The spark plasma sintered sample was then cross sectioned into roughly 5 mm<sup>2</sup> pieces, mechanically polished to 0.05 μm diamond finish, and thoroughly cleaned using organic solvents and DI water. The sectioned pieces were then placed polished side up in a 98 % high alumina crucible (CoorsTek Inc., Golden, CO) and thermally grooved in a box furnace (Lindberg Blue M, Thermo Scientific Ashville, NC) at temperatures ranging from 1350 °C to 1650 °C for either three hours for the 500 ppm sample, or five hours for the 100 ppm sample. For the case where the same sample was heated in decreasing temperature increments, the sample was hand polished from a 9 μm to 0.05 μm diamond polish and re-grooved.

Contact mode atomic force microscopy (AFM) was used to measure the topography of each sample. The images were collected with a 10 nm step size over an area covering tens of microns. The images were collected at random locations on the sample surface to average over possible chemical variations and to avoid preferentially imaging areas affected by abnormal grain growth.

The AFM images were analyzed with Gwyddion<sup>66</sup>. The background of each image was corrected using mean plane subtraction and, when necessary, a match line correction was also applied. The widths, heights, and standard deviations of the thermal grooves were determined by extracting three line profiles perpendicular to each grain boundary, an example of which can be seen in Figure 8.1. These profiles were extracted to a text file, and the width and height of the grain boundary thermal groove geometry was measured using an in-house MatLab program. A half angle version of Mullins' analysis, equation 8.1, was then applied to calculate the relative grain boundary to surface energy ratio for each boundary.

$$\frac{\gamma_b}{\gamma_s} = 2 \sin(\tan^{-1}(4.73(\frac{d}{2w}) + \mathcal{N})) \quad (8.1)$$

A cumulative distribution of at least 85 distinct boundaries was then plotted for each temperature, and the mean energy of these distributions is assumed to be representative of the true relative grain boundary energy, as found in previous work<sup>37</sup>.

Thermal grooving kinetics is a function of surface diffusion, so the speed at which a groove forms is dependent on temperature. Because each of the Y-doped alumina samples was heated for a set time at different temperatures, there is a possibility that a systematic change in the grain boundary groove width will lead to systematic uncertainty in the measurement of the relative energy with temperature. Saylor and Rohrer have shown that at groove widths around 1.5 to 2  $\mu\text{m}$ , the AFM probe geometry does not significantly affect the accuracy of the calculated

surface to grain boundary energy ratio; however smaller groove widths introduce larger measurement errors. These errors are tabulated in Figure 8.2, which is reproduced from Reference (<sup>37</sup>). In the current work, grooves formed at lower temperatures are narrower and this will lead to a systematic underestimation of groove angle. We have used the data in Figure 8.2 to correct our measurements (N in equation 8.1), reducing the uncertainty caused by the narrow grooves. Note that while these corrections change the values of the relative energy, the conclusions do not rely on the corrected values.

In the 500 ppm Y-doped alumina samples, a second phase was found at higher grooving temperatures. Dual analysis Electron Backscatter Diffraction (EBSD) and Energy Dispersive Spectroscopy (EDS) (EDAX, TEAM Software, Mahwah, NJ) interfaced with a Quanta 200 environmental SEM (FEI, Hillsboro, OR) was used to identify the composition and structure of the second phase. The EBSD images were collected in high vacuum with a 15 kV accelerating voltage, 5.5 spot size, and high-resolution step size such that a significant amount of data was collected from the second phase region.

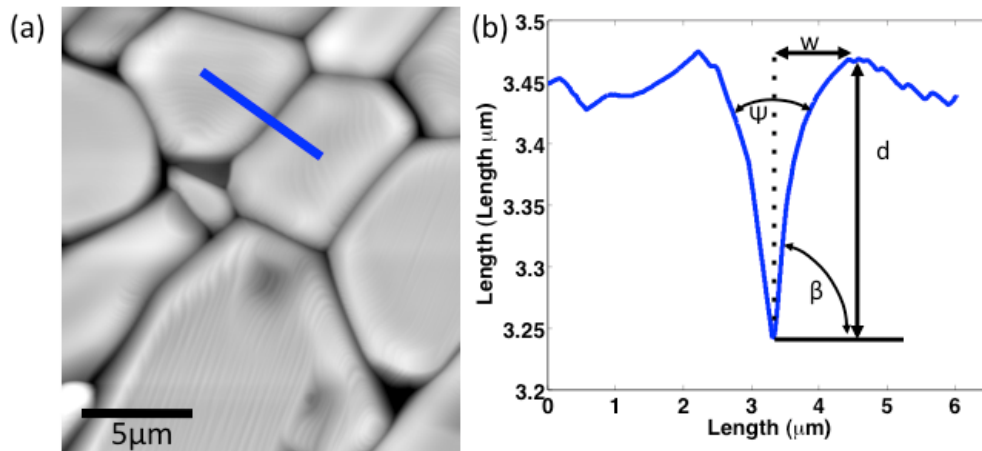


**Figure 8.1.** Representative topographic AFM images for Y-doped alumina (a) and corresponding thermal groove profile (b) where the groove half width ( $w$ ), height ( $d$ ), groove angle ( $\beta$ ) and surface dihedral angle ( $\Psi$ ) are labeled and correspond to equation 1 below.

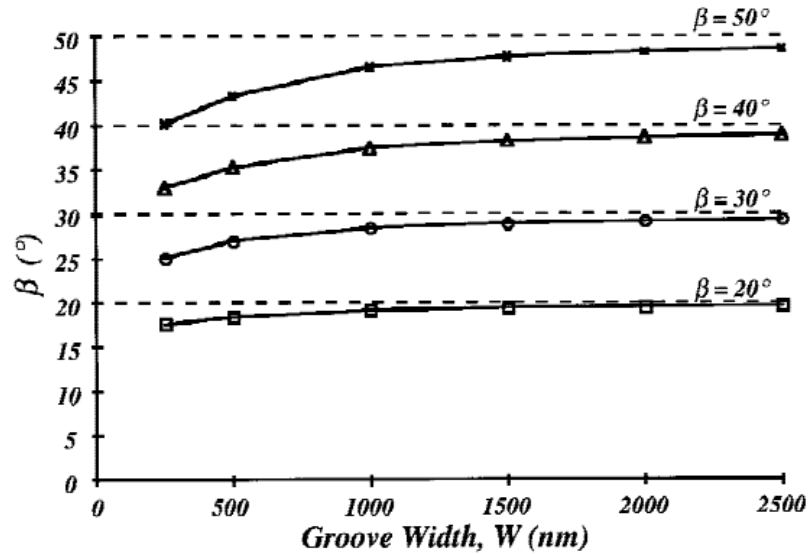


**Figure 8.2.** AFM tip convolution as a function of thermal groove widths at different groove angles ( $\beta$ ). Small widths have a significant tip-induced error, while larger widths exhibit realistic  $\beta$  measurements. Reproduced from Reference (37).

### 8.3 Results

#### 8.3.1 100 ppm Y-doped alumina

The 100 ppm Y-doped alumina pellet was sectioned into many small pieces, polished, and thermally grooved at temperatures between 1350 °C and 1650 °C. Figure 8.3 shows representative AFM images for each temperature step. At 1300 °C and 1400 °C, the microstructure shows a small uniform grain size distribution – in agreement with small grain size measurements observed by previous researchers<sup>21, 59</sup>. Between 1450 °C and 1650 °C, “ghost” boundaries can be seen on some of the grains, as indicated by the arrow in Figure 8.3 d. Ghost boundaries are remnants of thermal grooves that remain at the past locations of grain boundaries after a single grain grows abnormally fast through a smaller grained matrix. These ghost boundaries can be used as an indication for a significant increase in grain boundary mobility of the grains that grew through them, which is typically a sign of a complexion transition<sup>11</sup>.

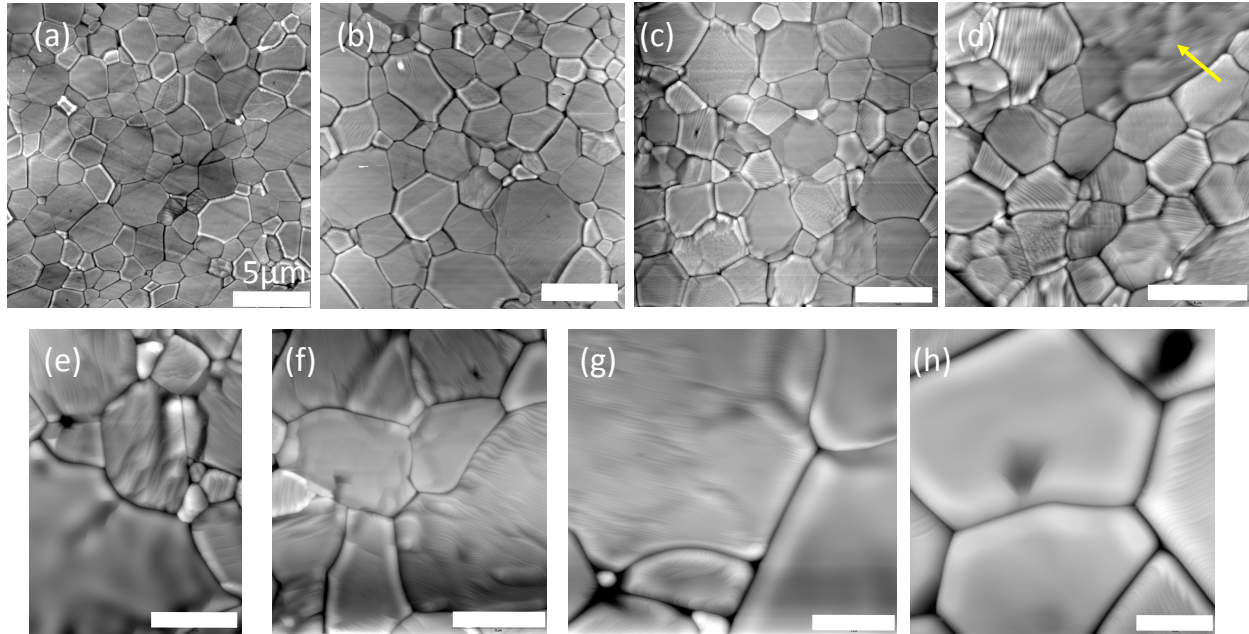


**Figure 8.3.** Representative AFM topographs from each grooving temperature increment in the 100 ppm Y-doped alumina that was thermally grooved at: 1350 °C (a), 1400 °C (b), 1450 °C (c), 1500 °C (d), 1525 °C (e), 1550 °C (f), 1600 °C (g), 1650 °C (h). Where the yellow arrow indicates the presence of an abnormally large grain with ghost boundaries. The scale bar in all cases is 5  $\mu\text{m}$ .

Example cumulative distributions for the uncorrected data annealed at 1350 °C, 1450 °C, 1550 °C, and 1650 °C can be seen in Figure 8.4. The mean grain boundary to surface energy ratio of the 100 ppm sample at each of the temperatures is plotted in Figure 8.5 a, where the blue line indicates the average of the raw relative grain boundary energy measurements and the red line indicates the average of the relative grain boundary energy measurements that were corrected for the error that is expected to arise from the narrow groove width. The groove width is plotted as a function of temperature in Figure 8.5 b.

In both the original and corrected analyses of the 100 ppm experiment, the grain boundary energies increased with increasing temperature from 1350 °C to 1450 °C. Between 1450 °C and 1500 °C the mean energy decreased 15 % from 0.84 to 0.71 (original) or 20 % from 1.05 to 0.84 (corrected). At 1550 °C, the mean energy was about the same as that at 1500 °C. In an attempt

to find the minimum energy in the lower energy regime, the grain boundary energy was measured at 1525 °C, this measurement was unexpectedly higher than both the 1500 °C and 1550 °C measurements. The average energies increased at temperatures above 1550 °C – indicating that the majority of the boundaries transformed to the lower energy state and thus the segregation-driven increase in energy with temperature was again dominant.

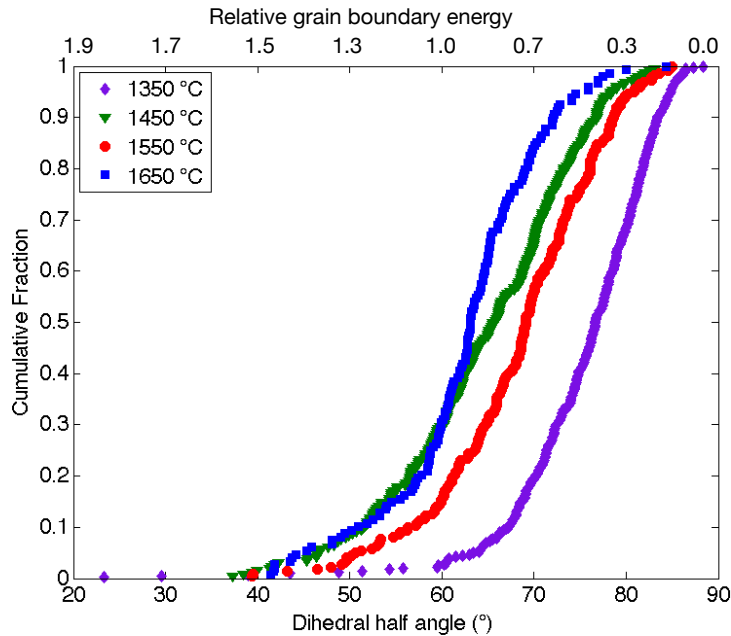


**Figure 8.4.** Cumulative distribution of relative grain boundary energies for the 100 ppm samples grooved at 1350 °C (purple diamond), 1450 °C (green square), 1550 °C (red circle), and 1650 °C (blue square)

The 100 ppm sample that was grooved at 1650 °C was then re-polished, cleaned, and grooved at 50 ° temperature increments from 1600 °C to 1400 °C for three hours. The energy decreased with decreasing temperature (green in Figure 8.5a), and the average groove widths (Figure 4b) were greater than those measured in the increasing temperature experiments, so there was no need to correct for errors associated with narrow grooves. There was a 7.6% increase in mean energy at 1500 °C; this indicates that the complexion transition that decreased the grain boundary energy at 1500 °C may be reversible. Additionally, the groove widths were wider for

this decreasing energy experiment. It is hypothesized that the larger widths are due to the difference in surface quality from different polishing procedures – where this series of measurements were taken in between a hand polishing procedure. The different finished surface could have resulted in increased plastic damage causing an increased stored surface energy; this could result in enhanced surface diffusion compared to mechanically polished samples.

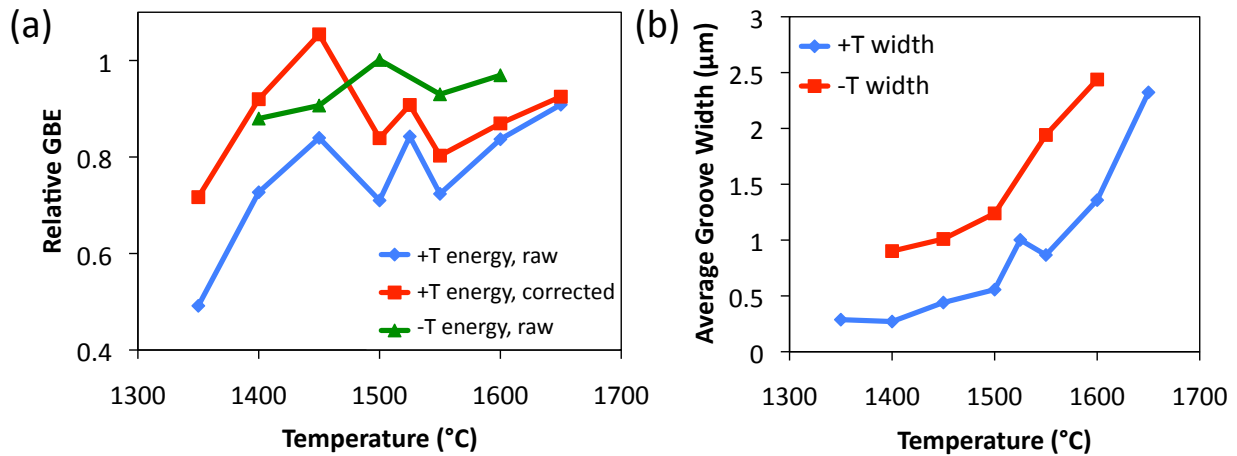


**Figure 8.5.** The relative grain boundary energy as a function of temperature for the 100 ppm Y-doped alumina sample can be seen in (a). The original measurements are in blue (diamond), the corrected measurements are in red (square), and the decreasing temperature measurements are in green (triangle). (b) Shows the groove width as a function of temperature for the increasing temperature experiment in blue (diamond) and the decreasing experiment red (square).

### 8.3.2 500 ppm Y-doped alumina

The 500 ppm Y-doped alumina samples were heated for 5 hours at the same temperatures as the 100 ppm sample. Representative topographic AFM images for each grooving temperature are shown in Figure 8.6 and the corresponding energies and groove widths can be found in figure 8.7 a and b respectively. At 1350 °C and 1400 °C, there is again a small uniform grain morphology, similar to that of the 100 ppm sample. The average relative grain boundary energies were fairly consistent at around 0.7, however the groove widths were significantly different, where the average width at 1350 °C was 0.3 μm, and the average width at 1400 °C was 1.1 μm. After correcting for the error caused by the narrow width, the energy significantly

decreased between the temperature of 1350 °C and 1400 °C. The grain boundary energy increases between 1400 °C and 1450 °C and the groove width remained constant. The grain boundary energy then decreased by 25% between 1450 °C to 1550 °C, at which point the groove width decreased by 14% from (1.18  $\mu\text{m}$  to 1.02  $\mu\text{m}$ ). This decrease in energy was accompanied by both the presence of abnormal grain growth as well as the precipitation of a second phase. It is possible that the high mobility grain boundaries – those that surrounded grains containing ghost boundaries – had less time at any given location to form the grooves, which could result in the observed decrease in groove width. However, the shape is assumed to be self-similar, so this should not affect the energy determination.

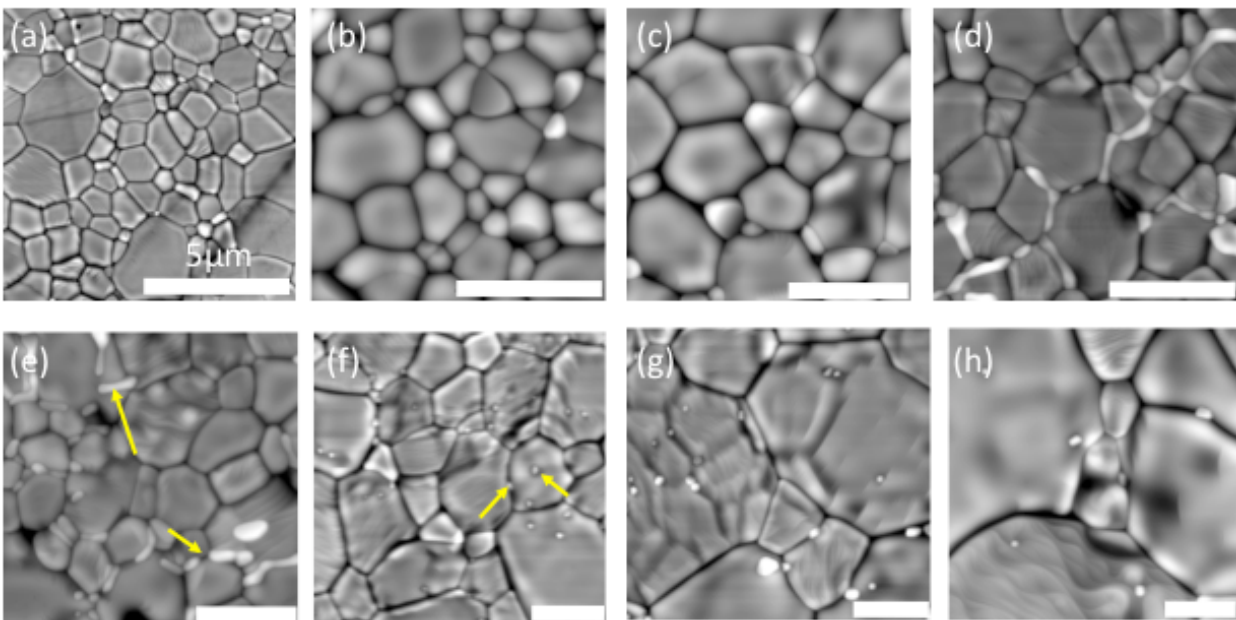


**Figure 8.6.** Representative topographic AFM images of 500 ppm Y-doped alumina grooved at: 1350 °C (a), 1400 °C – showing exaggerated grooving (b), 1450 °C – showing exaggerated grooving (c) and second phase precipitation (d), 1500 °C – showing ghost boundaries and the arrows indicate a wetting second phase (e), 1550 °C – where the arrows show small second phase particles (f), 1600 °C (g), and 1650 °C (h). In these images, the yellow arrows indicate different second phase morphologies including wetting along the boundaries and smoothly curved particles. All scale bars are 5  $\mu\text{m}$ .

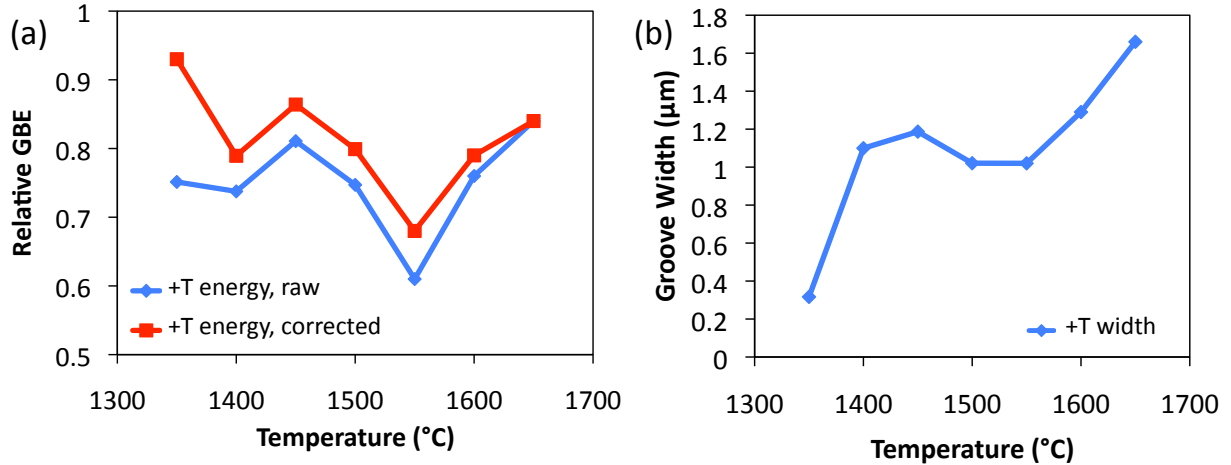


**Figure 8.7.** (a) The relative grain boundary energy as a function of temperature for the 500 ppm Y-doped alumina sample where the blue (diamond) represents the original data and the red (square) represents the groove width corrected data. (b) Shows the average grain boundary groove width as a function of temperature.

## 8.4 Discussion

### 8.4.1 Why is the slope positive?

As mentioned in the background section of this chapter and in the background of this document (Chapter 2), the grain boundary energy of impure materials has been shown to increase with increasing temperature<sup>107–109</sup>. In the current work, this trend is also observed, where the average grain boundary energy increases with increasing temperature. However, the temperature dependence of the average grain boundary energy in the temperature range where a complexion and/or phase transformation occurs has not been previously observed.

The interfacial or grain boundary energy of a pure material is known to decrease with increasing temperature; this is due to the positive entropy of the interface and thus the negative entropic contribution to the free energy<sup>106,107</sup>. The temperature dependence of grain boundary energy in a non-pure material is dependent on both the excess entropy as well as the adsorption of the impurity to the interface. These are related through the Gibbs adsorption equation (Equation 8.2), where  $\gamma$  is the interfacial energy,  $s^s$  is the specific interfacial excess entropy,  $\Gamma_i$  is

the specific interfacial excess or adsorption of component  $i$ , and  $\mu$  is the chemical potential of component  $i$ .

$$d\gamma = -s^s dT - \sum_i \Gamma_i d\mu_i \quad (8.2)$$

It is possible to write the surface energy of a multi-component system in terms of internal specific energy ( $e^s$ ), interfacial excess entropy, and the change in energy that results from adsorption. This is described by equation 8.3, and is known as the surface excess grand potential.

$$\gamma = e^s - Ts^s - \sum_i \mu_i \Gamma_i \quad (8.3)$$

To determine the temperature dependence of the adsorption parameters in the grand potential, the Langmuir-McLean isotherm can be used. In this case, the ideal solution approximation is applied to relate the atomic fraction of adsorbent at the interface ( $x^s$ ) and in the bulk ( $x$ ) to an Arrhenius temperature dependence, described by equation 8.4.

$$\frac{x^s}{1-x^s} = \frac{x}{1-x} \exp\left(-\frac{\Delta H_{seg}}{RT}\right) \quad (8.4)$$

The atomic fraction of adsorbents can be related to the adsorption component by equation 8.5.

Where  $\sigma$  is the area per mole of a monolayer interface.

$$\Gamma = \frac{(x^s - x)}{\sigma} \quad (8.5)$$

Multiple variations of the Langmuir-McLean model have been conceptualized to account for chemical and elastic contributions to the system, which result in the replacement of the enthalpy of segregation term ( $\Delta H_{seg}$ ) with an energy of segregation ( $\Delta E_{seg}$ )<sup>12, 39</sup>. An average value for the energy and segregation parameters discussed in the literature can be seen in Table 8.1, but it should be noted that these have been found to be dependent on grain boundary plane, bulk composition, and temperature - such trends can be seen in references<sup>(12, 39, 79, 113)</sup>. In general,

from the Arrhenius nature of equation 8.4, we can see that as the temperature increases, the atomic fraction of adsorbents at the interface decreases.

By combining equations 8.2, 8.3, and 8.4, it is possible to conclude that the grain boundary energy in a system with impurities will increase with increasing temperature<sup>12, 39</sup>. This increase continues until a critical temperature, where all of the solute will have desorbed from the boundary. At this point, the energy will decrease because of the intrinsic interfacial entropy term. This trend has been experimentally and computationally verified<sup>39, 109</sup>.

**Table 8.1.** Range of values for thermodynamic segregation calculations in Y-doped alumina

$\Delta E_{\text{seg}}$ <sup>113, 114</sup> [J/m <sup>2</sup> ]	$\Delta H_{\text{seg}}$ <sup>31</sup> [eV/cation]	$\gamma_{\text{gb}}$ <sup>31, 93</sup> [J/m <sup>2</sup> ]	$\Gamma_{\text{Y}}$ <sup>19, 31, 79, 93, 115</sup> [cations/nm <sup>2</sup> ]
0.5-0.7	~ -2.5	1.5-3	2 - 10

#### 8.4.2 Why does the GBE decrease after increasing?

Previous results have shown that the relative energies of boundaries that underwent a transformation from a metastable to equilibrium complexion significantly decreased. For the case of Y-doped alumina, there was a 46 % decrease in energy when comparing transformed, high mobility boundaries surrounding abnormal grains and metastable boundaries surrounding normal grains<sup>6</sup>. Chapter 6 presents an experiment that compared the change in energy of a high and low energy interfaces embedded in the Y-doped alumina polycrystal after being heated to 1500 °C for 8 hours. In that case, the high-energy interface was almost completely surrounded by abnormal grains and the interfacial energy decreased 19 %, while the lower energy interface was partially transformed and the mean energy decreased 27 %. Additional work has also shown that there seems to be temperature and character dependence to the rate at which grain boundary complexions transform – as indicated by character-dependent nucleation rate of abnormal grain

growth (Ch 7). Presently, the 100 ppm Y-doped alumina experiment exhibits a 20% (corrected) decrease in mean energy between the 1450 °C and 1500 °C, while the 500 ppm Y-doped alumina series exhibits a 25 % decrease in mean energy between 1450 °C and 1550 °C. The current results do not exhibit as drastic a decrease in energy as the 46% decrease when comparing normal and abnormal boundary energies in Y-doped alumina that was previously observed. However, they exhibit similar energy difference as the decrease in mean energy of the high and low energy – partially transformed - interfaces of the previous study (Ch. 6). Additional results, found in Ch. 7, show that when Y-doped alumina was heated to 1450 °C and 1500 °C, a complete transformation to an impinged abnormal grain size distribution was not observed, even when held for longer than the three and five hour grooving times that were used in the current work. Dillon et al.<sup>6</sup> compared boundaries known to have transformed to those known to have not transformed, whereas the current experiment randomly selects boundaries, so there is a mixture of both. Therefore, Dillon's results exhibiting a 46% decrease in energy are not expected until all of the boundaries transform. Finally, although a decrease in energy is observed with the change in free energy due to the grain boundary transformation, the increase of grain boundary energy due to solute de-segregation cannot be completely ignored. This may be an additional factor contributing to the less pronounced decrease in average boundary energy at the transition temperature.

### **8.4.3 100 ppm Y-doped alumina**

#### ***8.4.3.1 Grain boundary energy with increasing temperature***

The average grain boundary to surface energy ratio for the 100 ppm Y-doped alumina increased with grooving temperature until the relative energy surpassed one (corrected values). Previous results have shown that undoped alumina has an average relative grain boundary energy of about 1.1-1.2<sup>68, 116</sup>, and doped-alumina exhibits an energy less than one<sup>6</sup>. Because yttrium is

barely soluble in the alumina lattice (solubility limit of about 10 ppm), any additional yttrium is adsorbed to the boundaries, which would lower the boundary energy. However, at the maximum energy observed at 1450 °C, the average energy of the Y-doped alumina was approximately equal to the intrinsic pure alumina grain boundary energy. From this, it is possible that the yttrium is no longer decreasing the energy of the interface. Because the Y-doped boundaries are no longer energetically favorable compared to intrinsic pure alumina boundaries, it can be assumed that the Y-doped boundaries are metastable; therefore the driving force for a grain boundary complexion transition would be high. In this case, with the material's grain boundary energy similar to the maximal intrinsic grain boundary energy of the pure material, the driving force will be great enough to overcome the nucleation barrier to form a new equilibrium complexion with a lower grain boundary energy.

It should also be noted that there is a clear increase in average grain boundary energy of the 100 ppm sample at 1525 °C, where a minimum was expected. These results suggest that there may be multiple complexion transformations in the Y-doped alumina system that are dependent on temperature and composition, each transition would cause a distinct decrease in energy. Previous work by Dillon et al. noted five distinct complexions in the Y+Si co-doped alumina system<sup>29</sup>. While Si was not intentionally added to the experiment, contamination may have occurred in processing steps – this could be an explanation for a second transition. Additionally, it is possible that a microscopic second phase nucleated<sup>17, 58, 80</sup> resulting in an increase in grain boundary energy of some boundaries from which Y desorbed, while other boundaries continued to undergo the complexion transformation to decrease energy.

#### ***8.4.3.2 Reverse transition experiment***

The 100 ppm Y doped alumina sample that was heated at 1650 °C for five hours was then re-polished and grooved at 1600 °C and the grain boundary energy of the new grooves were

measured, this was repeated at 50 °C increments until 1400 °C. This reverse experiment was done to assess the likelihood that a complexion would back transform to the lower temperature equilibrium complexion, where the reverse transition would be indicated by an approximately 15 % increase in grain boundary energy. It should be noted that, as a test of reversibility, the experiment is imperfect. Because the sample was already heated to high temperature, the grain size is much larger and it is possible that microscale second phase precipitates have already formed. Though it should be noted that there were not second phases detected on the surface of the 100 ppm sample. The reduced grain boundary area and the presence of a second phase would mean that any effects associated with grain boundary supersaturation are unlikely to occur.

The current results show that, in general, the grain boundary energy decreases with decreasing temperature. However, between 1550 °C and 1500 °C, the mean energy increases by 7.6%, from (0.93) to (1.00). The magnitude of this increase in energy was not as great as the previously observed decrease in energy of the transition to a high temperature complexion. Additionally, in the results showing grain boundary energy with an increase in temperature, the transition caused an overall decrease in boundary energy that acted as a starting point for a further de-adsorption driven increase in post-transitioned boundary energy. The increase in the boundary energy at 1500 °C in the reverse transformation experiment did not seem to permanently increase the energy, and instead the 1450 °C mean energy was along the same decreasing energy trajectory as the 1550 °C measurement.

Previous work by Luo et al. has shown that the ability for a complexion transition to back transform to a low temperature complexion could take weeks to occur<sup>117</sup>. Dillon et al.<sup>29</sup> proposed that this was due to a significant kinetic barrier to the reverse transition. The current

results indicate that there may be two thermodynamic barriers to the reverse transition. First, the decreased diffusion at lower homologous temperatures would result in a significant kinetic barrier for the transformation to a low temperature equilibrium complexion. Secondly, the energy of the boundaries are already decreasing with decreasing temperature, so the energetic input that initiated the transition from a low to high temperature equilibrium grain boundary complexion at 1500 °C would not be available for the reverse transition. However, it is also possible that when temperature is increased, the transition places excess solute at the boundary in advance of or simultaneous to the precipitation of a second phase. In the case of the 100 ppm sample, there is no observable second phase, but it could be present in a microscopic scale along the boundary. For the reverse transition to a more ordered complexion, solute would need to be removed from the grain boundary, and the second phase would already be present to act as a sink for the de-adsorption. This might make the transition somewhat easier. In summary, because the energy increased at 1500 °C indicates a reverse transition, and other clues as discussed above indicate there was no reverse transition – we can not definitely conclude, with the results of this experiment, if a reverse transition from a high to low temperature complexion occurred in the Y-doped alumina sample.

#### **8.4.4 500 ppm Y-doped alumina – Energy and Y excess**

A calculation showing the stable grain boundary coverage verses grain size in the Y-doped alumina system can be seen in Figure 8.8. In this approximation, a simple cubic packing structure was assumed for the interfacial structure and the grains were assumed to be spherical where the adsorbed structures would cover each grain. This is an oversimplification of the system and ignores all grain boundary character and energy anisotropy, however is useful for an approximation of how much yttrium can be reasonable held at the grain boundaries at various

grain boundary thicknesses and grain sizes. In the case of the 100 ppm Y-doped alumina, it is possible for the assumed sub-monolayer grain boundary structure to be stable at about a 1-2  $\mu\text{m}$  grain size – as is experimentally observed. Even when the grains begin to grow, an approximate sub-monolayer or monolayer of coverage should remain somewhat stable. However, if some grain boundaries exhibited such a high energy that they underwent a complexion transition that resulted in significantly increased mobility, a grain size of about 10  $\mu\text{m}$  would require a more disordered, thicker boundary. However, for the 500 ppm yttrium, all of the Y can be accommodated at the boundaries of approximately 1  $\mu\text{m}$  grains, but once the grains begin to grow the monolayer of Y will transition to a multilayer structure or nucleate a second phase. After a mean grain size of about 3  $\mu\text{m}$  is reached, the capacity of the grain boundaries to accommodate the solute is greatly exceeded and the Y would have to either form a thick intergranular film or a second phase.

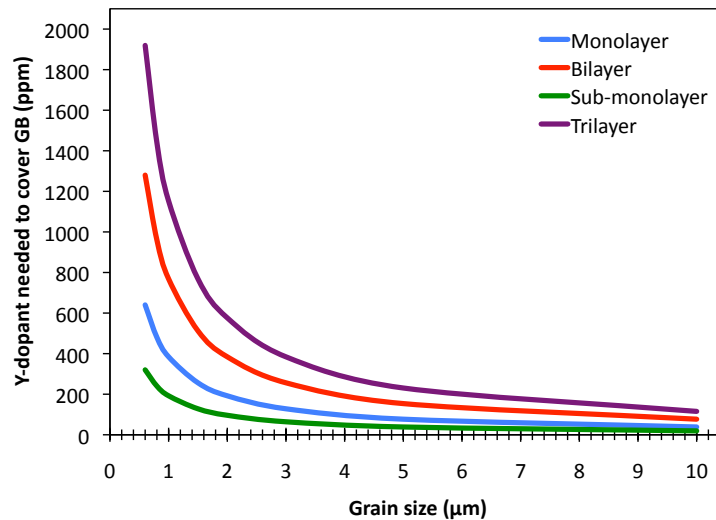


**Figure 8.8.** Approximate amount of Yttrium needed to sustain a certain grain boundary coverage at a given grain size, assuming vanishing bulk solubility.

Previous work on Y-doped alumina has both theoretically and experimentally shown an increase in boundary excess with bulk concentration until a super saturation limit is reached, at

which point a second phase precipitates and the boundary concentration is reduced<sup>19, 79</sup>. Based on the observations reported in reference (79), it is believed that the 500 ppm Y-doped alumina sample that was grooved at 1350 °C was on the edge of the dilute adsorption grain boundary region – where all of the Y is accommodated in the boundary. A relatively small increase in temperature and grain size when grooved at 1400 °C caused a transition to the supersaturated regime – where near boundary layers are also saturated with Y. This can be viewed as a complexion transition, however not one that enhances the mobility of the transformed boundaries. Because there is more Y at the grain boundary, this explains the decrease in grain boundary energy and significant increase in grooving kinetics between the 1350 °C and 1400 °C grooving temperatures. After that initial adsorption, the supersaturated boundary would undergo Langmuir-McLean desorption and second phase precipitation, causing the grain boundary energy to increase at 1450 °C.

As the grain size increases, the grain boundary area decreases and thus the grain total amount of Y that can be accommodated at the boundaries would also decrease.

Thermodynamically speaking, solute excess above the boundary saturation limit can result in either a supersaturation of the lattice, a precipitation of a second phase, or a transition to a thicker complexion. In most cases, a second phase is seen, at least on the sub-nanometer scale, in samples that exhibit complexion transformations that result in abnormal grain growth<sup>30</sup>.

However, each boundary may have a different thermodynamic nucleation barrier for both the precipitation of a second phase and a grain boundary complexion transformation. Therefore, it is proposed that the increase in boundary concentration in the 500 ppm sample decreased the barrier for phase precipitation such that it can occur at 1450 °C. The boundary seems to be transitioning from a supersaturated state to an apparently equilibrium composition that coexists

with a second phase, as was implied by previous researchers<sup>19, 79</sup> and further shown in Figure 8.9. This second phase precipitation at 1450 °C does not decrease the grain boundary energy, this is because the solute is removed from the boundary into the second phase, exacting a similar effect to the Langmuir-McLean model in equation 8.4— thus increasing the interfacial energy.

At 1500 °C, it is obvious that some of the grain boundaries in the 500 ppm Y-doped alumina sample begin to exhibit a higher than normal mobility – this is again indicated by the presence of ghost boundaries in the AFM images of figure 8.6. This enhanced mobility is most likely due to the corresponding grain boundaries undergoing a complexion transition, and has been seen throughout this research project to decrease the energy of the boundaries surrounding abnormally large grains compared to the boundaries surrounding normal sized grains. The average grain boundary energy decreases by 25% between 1450 °C and 1550 °C, additionally the second phase particles seem to coalesce at higher temperatures.

#### **8.4.5 Second phase precipitation**

Previous results by Dillon et al.<sup>30</sup> have indicated that the relative inter phase energy between pure alumina and YAG is roughly the same as the relative grain boundary energy between alumina and alumina adjacent to the alumina/YAG interface. Those results indicated that YAG is energetically neutral in alumina, so yttria doping should not induce numerous complexion transitions. The current work shows that while YAG does precipitate in Y-doped alumina, high mobility grain boundary complexions will also nucleate at the same compositions and temperatures. The difference in these results could be due to the fact that Dillon et al. analyzed the boundary energies at 1300 °C, and the current work shows that there is a temperature dependence of grain boundary energies which may also apply to inter phase boundaries. Additionally, these results show that the interrelationship between composition,

grain size, complexion transitions, and precipitation are not yet completely understood, and current literature is inconclusive on the composition and structure of the boundaries surrounding both abnormal and normal grains in this system<sup>17, 18, 59, 78–80</sup>.

Previous work has shown that Y-doped alumina will precipitate YAG, and in some cases YAP ( $\text{YAlO}_3$ ) and YAM (yttrium aluminum monoclinic) have also been formed<sup>115</sup>. In this experiment, it is clear that with increasing temperature, the 500 ppm sample displays both abnormal grain growth and the nucleation of a second phase that looks like it is wetting the boundaries. Figure 8.9 shows a region of the sample grooved at 1450 °C, where some boundaries seem to have exaggerated grooves while just a few microns away, the grooves are less exaggerated and a second phase formed along grain boundaries and triple junctions. It has been proposed that when a boundary becomes super saturated it can either nucleate a complexion or a second phase<sup>30</sup>. The existence of exaggerated grooves on the right side of Figure 8.9 indicates enhanced surface diffusion and high grain boundary energies— this may indicate grain boundary super saturation. The less exaggerated grooves in coexistence with the second phase on the left side of Figure 8.9 shows the precipitation of a second phase. This precipitation did not decrease the grain boundary energy, so we cannot say that the grain boundaries are in equilibrium with the second phase, as was stated elsewhere<sup>19, 79</sup>.

EBSD (Figure 8.10 a) and EDS (Figure 8.10 b) analysis of the second phase show that while on the macroscale it looks amorphous, the phase can be identified as crystalline YAG. The eutectic temperature for the alumina to YAG transition is at 1753 °C<sup>118</sup>, so the new phase is unlikely to be a liquid at the annealing temperature, even though these large areas of YAG form smoothly curved particles at elevated grooving temperatures. It is possible, however, that if there with sufficient Si contamination, a liquid Si-rich YAG phase could form<sup>80</sup>. Regardless of

the means of precipitation, these second phase particles do not seem to impede grain growth, as attested to by the presence of the particles within large grains in the 1550 °C – 1650 °C samples.

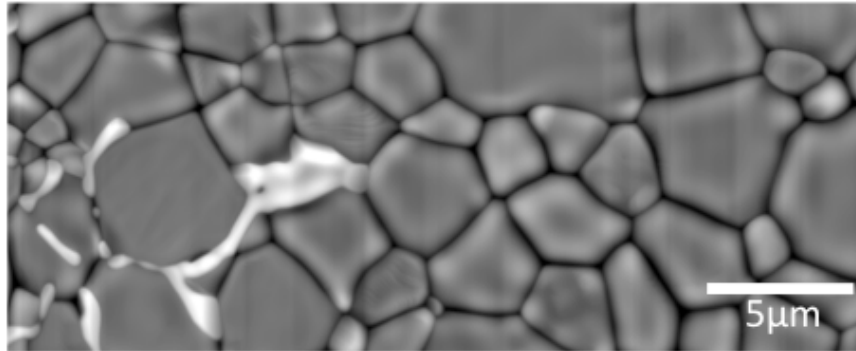


**Figure 8.9.** Representative topographic AFM image for the 500 ppm Y-doped alumina sample sintered at 1450 °C for five hours. In this image we see an area of exaggerated thermal grooving (right) and an area of second phase precipitation (left) around which the grains are not as rounded.

Šturm and co-workers previously investigated the formation of YAP and YAG in the Y-doped alumina system<sup>80</sup>. It was found that YAG precipitates occurred in samples that were also contaminated with Si. Although precautions were taken in the powder processing to make the current samples (Chapter 3), Si contamination of the sintered samples in the box furnace was unavoidable due to the molybdenum silicide heating elements. An EDS image showing the positions of Al, Y, and Si signals in the second phase precipitate is shown in Figure 8.10 b, and an EDS image of only Si signal can be seen in Figure 8.10 c. These images show that there is some Si contamination on the surface of the thermally grooved samples, and the Si is more concentrated in the YAG precipitates as opposed to the bulk grains. This verifies the conclusions drawn by Šturm and also indicates that a liquid Si-rich YAG phase could have formed. The Si contamination interaction with excess yttrium and the effect on boundary energies add an additional level of complexity to the composition dependence of the nucleation barrier for both second phase precipitation as well as complexion nucleation. Additionally, Si contamination from the heating elements causing YAG formation may explain why there was observably more

areas of second phase present at the high temperature grooved surface compared to when a sample is annealed, re-polished, and then grooved at a lower temperatures (Ch 6-7).

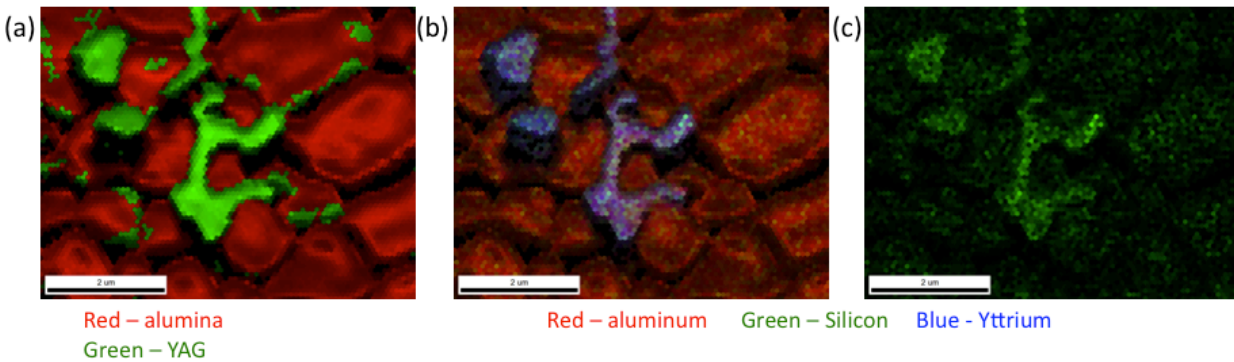


**Figure 8.10.** (a) EBSD map where points indexed as cubic YAG are in green and points indexed as alumina are in red, there is also an image quality overlay so that the grain and phase boundaries are evident. Some points that are indexed as YAG are clearly not correct. (b) EDS map where the blue represents yttrium atoms, green represents silicon, and red represents aluminum. (c) EDS map showing only Si signal – the combination of the EBSD and EDS results makes it clear that the second phase precipitates are a Si-rich YAG phase.

## 8.5 Conclusions

The grain boundary energy was measured as a function of temperature and composition in Y-doped alumina. It was found that in the 100 ppm Y-doped alumina experiment, the grain boundary energy increased with increasing temperature until 1450 °C. At that temperature, the grain boundary energy was approximately equivalent to the intrinsic alumina grain boundary energy. The difference between the high energy of the metastable grain boundaries and the low energy of the transformed grain boundaries is believed to be the driving force for the complexion transition that increased grain boundary mobility at 1500 °C. The mean energy decreased by 20 % between 1450 °C and 1500 °C. The grain boundary energy increased at 1525 °C and then decreased to approximately the same level as the 1500 °C sample at 1550 °C. After 1550 °C the mean grain boundary energy increased with increasing temperature to 1650 °C. When the fully transformed 1650 °C sample was re-grooved at lower temperatures, there was an increase at

1500° C, however it is not believed that this is a definitive indication of a back transformation for the complexion transition.

The 500 ppm sample exhibited a decrease in grain boundary energy from 1350 °C to 1400 °C which is believed to be due to a transition from a dilute to supersaturated boundary structure. The energy then increased along a similar trajectory as the 100 ppm sample until 1450 °C – at which point a second phase began to precipitate. Between 1450 °C and 1550 °C the mean energy decreased and both YAG second phase and high mobility grain boundaries were observed. This total decrease in energy was 25% - indicating a greater driving force for the complexion transition in 500 ppm Y-doped alumina as compared to the 20% decrease in the 100 ppm Y-doped alumina. After 1550 °C, the energy increased in a similar manner as the 100 ppm sample.

## 9. Summary of Conclusions

The following chapter summarized the conclusions that can be drawn from the research that was presented in this dissertation. A summary of the findings from each experiment will be presented, followed by a sentence summarizing the experiment's novel contributions to the scientific community.

In the first experiment, grain boundary character and energy distributions were measured for Ca-doped yttria, which displayed abnormal grain growth as a result of a complexion transition that involved a Ca-rich intergranular film. It was found that grain boundary character anisotropy increased with the occurrence of abnormal grain growth – this was in agreement with previous studies in alumina<sup>5</sup>. Additionally, the relative grain boundary energy of the boundaries surrounding abnormal grains as well as the boundaries surrounding normal grains that were immediately adjacent to the abnormal grains were both 33% lower in energy in comparison to the boundaries of the untransformed normal grains that were further away from the abnormal grains. These results gave insight into the propagation of an intergranular film complexion transition beyond just the boundaries surrounding abnormal grains, and through triple junctions to boundaries surrounding normal grains that are in close proximity to the abnormal grains.

The second experiment investigated the effects of yttrium and lanthanum doping on the grain boundary character distribution of alumina. It was found that La doping resulted in a random misorientation angle distribution and a strong preference for (0001) grain boundary planes. The grain boundary character distributions at each temperature were self-similar, indicating that there was no complexion transition in La-doped alumina sintered between 1500 °C and 1600 °C. Y doping resulted in a bimodal grain size distribution at 1500 °C where there

was an increasing population of  $60^\circ/[0001]$  grain boundaries with temperature and the number of abnormal grains. Additionally, the population of  $\{01\bar{1}2\}$  planes increased from the unimodal grain size sample sintered at  $1450^\circ\text{C}$  to the sample exhibiting a bimodal grain size distribution that was sintered at  $1500^\circ\text{C}$ . The microstructure at  $1600^\circ\text{C}$  had a greater population of  $\{1\bar{1}20\}$  planes and there was a minimum population of  $(0001)$  planes. The Y and La co dopants resulted in a self-similar grain boundary character distribution that exhibited local maxima of both  $(0001)$  and  $\{01\bar{1}2\}$  planes and  $60^\circ/[0001]$  grain boundaries. These results were the first to show an increase in grain boundary character anisotropy with abnormal grain growth and a further change in the preferred grain boundary plane with abnormal grain impingement. Additionally, this was the first time that a grain boundary misorientation has been shown to increase with the occurrence of abnormal grain growth.

The third experiment attempted to control complexion transitions by locally controlling the interfacial energy.  $(1\bar{1}20)$  and  $(0001)$  single crystals of sapphire were embedded in Y-doped alumina and heated to  $1500^\circ\text{C}$  for 8 hours. The  $(0001)$  interface was higher in energy than the  $(1\bar{1}20)$  interface in the sample that was spark plasma sintered at  $1300^\circ\text{C}$ . After the sample was heated to  $1500^\circ\text{C}$  for 8 hours, a bimodal grain size distribution occurred. More abnormal grains grew along the high energy  $(0001)$  interface than along the  $(1\bar{1}20)$  interface, and the energy of both interfaces decreased by 19 % and 27 % respectively. These results indicate that there is an energy dependence of complexion transitions, where high-energy interfaces require less thermal input to overcome the nucleation barrier to initiate a complexion transition while low energy interfaces need to be heated at longer times or at higher temperatures to nucleate the transition.

The fourth experiment analyzed the temperature and grain boundary character dependence of the rate of the complexion transformation in Y doped alumina and attempted to

compare it to that of a bulk phase transformation. At most annealing temperatures and times, the higher energy (0001) interface was in contact with a larger area fraction of abnormal grains, while there were fewer large grains along the  $(1\bar{1}\bar{2}0)$  interface. The rate of a complexion nucleation along each interface was greater for the higher energy (0001) interface at 1500 °C (0.69%/μm-hr) compared to the lower energy  $(1\bar{1}\bar{2}0)$  interfaces (0.16%/μm-hr). At 1600 °C the nucleation rate was approximately the same (0.3%/μm-hr) however the higher energy (0001) interface exhibited a much higher initial percent of the interface that was transformed. Finally, there was no apparent field effect with the spark plasma sintering method. These results showed that there is a character and temperature dependence on the rate of nucleating complexion transitions. A maximum number of grain boundaries are metastable at any given temperature, and that number increases with temperature. At any temperature within the range of critical nucleation temperatures, the number of boundaries that transforms increases with time such that the highest energy boundaries transform at the shortest times.

In the fifth and final experiment, the grain boundary energy was measured as a function of temperature and composition in the Y-doped alumina system. It was found that in the 100 ppm Y-doped alumina experiment, the grain boundary energy increased with increasing temperature until 1450 °C. The energy then decreased by 20 % with the occurrence of high mobility grain boundaries. After 1550 °C the lower energy grain boundaries again increased with increasing temperature. The 500 ppm sample exhibited a decrease in grain boundary energy from 1350 °C to 1400 °C, indicating a shift from dilute to supersaturated grain boundaries. The energy then increased until 1450 °C, where at 1450 °C a second phase began to precipitate. Between 1450 °C and 1550 °C the mean energy decreased and both YAG precipitation and high mobility grain boundaries were observed. The total decrease in energy was

25 %. After 1550 °C, the energy increased in a similar manner as the 100 ppm sample. These results show that the grain boundary energy increases with the precipitation of a second phase and decreases with the occurrence of a complexion transition. It also indicated that the increase in grain boundary energy due to solute desorption with temperature could provide a driving force for a grain boundary complexion transition in the Y-doped alumina system.

Overall these investigations show that the grain boundary energy anisotropy and temperature are the important parameters influencing the nucleation of the grain boundary complexion transition in Y-doped alumina. With this knowledge, it is possible to control and predict when and where a transition will occur. It is expected that similar trends can be observed in other ceramic and metallic systems. Specifically, it would be interesting to compare these results to a material that displays highly faceted abnormal grain morphology and complexion transitions involving intergranular films, such as the Ca-doped alumina system.

## 10. References:

- 1 S.J. Dillon, M. Tang, W.C. Carter, and M.P. Harmer, "Complexion: A new concept for kinetic engineering in materials science," *Acta Mater.*, **55** [18] 6208–6218 (2007).
- 2 S.J. Dillon, M.P. Harmer, and J. Luo, "Grain Boundary Complexions in Ceramics and Metals: An Overview," *Jom*, **61** [12] 38–44 (2009).
- 3 S.J. Dillon and M.P. Harmer, "Relating grain boundary complexion to grain boundary kinetics II: Silica-doped alumina," *J. Am. Ceram. Soc.*, **91** [7] 2314–2320 (2008).
- 4 S.J. Dillon and M.P. Harmer, "Relating grain-boundary complexion to grain-boundary kinetics I: Calcia-doped alumina," *J. Am. Ceram. Soc.*, **91** [7] 2304–2313 (2008).
- 5 S.J. Dillon, H. Miller, M.P. Harmer, and G.S. Rohrer, "Grain boundary plane distributions in aluminas evolving by normal and abnormal grain growth and displaying different complexions," *Int. J. Mater. Res.*, **101** [1] 50–56 (2010).
- 6 S.J. Dillon, M.P. Harmer, and G.S. Rohrer, "The Relative Energies of Normally and Abnormally Growing Grain Boundaries in Alumina Displaying Different Complexions," *J. Am. Ceram. Soc.*, **93** [6] 1796–1802 (2010).
- 7 P.R. Cantwell, M. Tang, S.J. Dillon, J. Luo, G.S. Rohrer, and M.P. Harmer, "Grain Boundary Complexions," (n.d.).
- 8 E.W. Hart, "Two-Dimensional Phase Transformation in Grain Boundaries," *Scr. Mater.*, **2** 179–182 (1968).
- 9 J.W. Cahn, "Transitions and Phase Equilibria Among Grain Boundary Structures," *J. Phys.*, **12** 199–212 (1982).
- 10 M. Tang, W.C. Carter, and R.M. Cannon, "Diffuse interface model for structural transitions of grain boundaries," *Phys. Rev. B*, **73** [2] (2006).
- 11 S.J. Dillon and M.P. Harmer, "Multiple grain boundary transitions in ceramics: A case study of alumina," *Acta Mater.*, **55** [15] 5247–5254 (2007).
- 12 W.D. Kaplan, D. Chatain, P. Wynblatt, and W.C. Carter, "A review of wetting versus adsorption, complexions, and related phenomena: the rosetta stone of wetting," *J. Mater. Sci.*, **48** 5681–5715 (2013).
- 13 J. Wong, "Sintering and varistor characteristics of ZnO-Bi<sub>2</sub>O<sub>3</sub> ceramics," *J. Appl. Phys.*, **51** [8] 4453–4459 (1980).
- 14 S.A. Bojarski, S. Ma, W. Lenthe, M.P. Harmer, and G.S. Rohrer, "Changes in the grain boundary character and energy distributions resulting from a complexion transition in Ca-doped Yttria," *Metall. Mater. Trans. a-Physical Metall. Mater. Sci.*, (2012).
- 15 J. Luo, H. Cheng, K.M. Asl, C.J. Kiely, and M.P. Harmer, "The Role of a Bilayer Interfacial Phase on Liquid Metal Embrittlement," *Science (80-. )*, **333** [6050] 1730–1733 (2011).
- 16 S. Ma, W. Shou, C.J. Kiely, and M.P. Harmer, "Grain Growth of Calcia or Silica Doped Yttria in a Reducing Atmosphere," *Submitt. publication*, (2012).
- 17 D. Bouchet, F. Dupau, and S. Lartigue-Korinek, "Structure and chemistry of grain boundaries in yttria doped aluminas," *Microsc. Microanal. Microstruct.*, **4** [6] 561–573 (1993).
- 18 M.A. Gülgün, V. Putlayev, and M. Rühle, "Effects of Yttrium Doping  $\alpha$ -Alumina: I, Microstructure and Microchemistry," *J. Am. Ceram. Soc.*, **82** [7] 1849–1856 (1999).
- 19 C.M. Wang, G.S. Cargill, H.M. Chan, and M.P. Harmer, "Structural features of Y-saturated and supersaturated grain boundaries in alumina," *Acta Mater.*, **48** [10] 2579–2591 (2000).
- 20 Thomas Gemming, Stefan Nufer, Wolfgang Kurtz, and M.R. Rühle, "Structure and Chemistry of Symmetrical Tilt Grain Boundaries in  $\alpha$ -Al<sub>2</sub>O<sub>3</sub>: II, Bicrystals with Y at the Interface," *J. Am. Ceram. Soc.*, **86** [4] 590–594 (2003).
- 21 S. a. Bojarski, J. Knighting, S.L. Ma, W. Lenthe, M.P. Harmer, and G.S. Rohrer, "The Relationship between Grain Boundary Energy, Grain Boundary Complexion Transitions, and Grain Size in Ca-Doped Yttria," *Mater. Sci. Forum*, **753** 87–92 (2013).
- 22 M. Tang, W.C. Carter, and R.M. Cannon, "Grain boundary transitions in binary alloys," *Phys. Rev. Lett.*, **97** [7] (2006).
- 23 J.P. Buban, K. Matsunaga, J. Chen, N. Shibata, W.Y. Ching, T. Yamamoto, and Y. Ikuhara, "Grain Boundary Strengthening in Alumina by Rare Earth Impurities," *Science (80-. )*, **311** [5758] 212–215 (2006).

- 24 J. Cho, M.P. Harmer, H.M. Chan, J.M. Rickman, and A.M. Thompson, "Effect of Yttrium and Lanthanum  
25 on the Tensile Creep Behavior of Aluminum Oxide," *J. Am. Ceram. Soc.*, **80** [4] 1013–1017 (1997).
- 26 H. Yoshida, Y. Ikuhara, and T. Sakuma, "High-temperature creep resistance in rare-earth-doped, fine-  
27 grained Al<sub>2</sub>O<sub>3</sub>," *J. Mater. Res.*, **13** [9] 2597–2601 (1998).
- 28 X. Shi and J. Luo, "Developing grain boundary diagrams as a materials science tool: A case study of nickel-  
29 doped molybdenum," *Phys. Rev. B*, **84** [1] 14105–14118 (2011).
- 30 G.S.R. Tomoko Sano, "Experimental Evidence for the Development of Bimodal Grain Size Distributions by  
31 the Nucleation-Limited Coarsening Mechanism," (n.d.).
- 32 G.S. Rohrer, "INFLUENCE OF INTERFACE ANISOTROPY ON GRAIN GROWTH AND  
33 COARSENING," *Annu. Rev. Mater. Res.*, **35** [1] 99–126 (2005).
- 34 S.J. Dillon and M.P. Harmer, "Demystifying the role of sintering additives with 'complexion,'" *J. Eur.  
35 Ceram. Soc.*, **28** [7] 1485–1493 (2008).
- 36 S.J. Dillon, M.P. Harmer, and G.S. Rohrer, "Influence of interface energies on solute partitioning  
37 mechanisms in doped aluminas," *Acta Mater.*, **58** [15] 5097–5108 (2010).
- 38 S. Galmarini, U. Aschauer, A. Tewari, Y. Aman, C. Van Gestel, and P. Bowen, "Atomistic modeling of  
39 dopant segregation in  $\alpha$ -alumina ceramics: Coverage dependent energy of segregation and nominal dopant  
40 solubility," *J. Eur. Ceram. Soc.*, **31** [15] 2839–2852 (2011).
- 41 D.M. Saylor, "The Character Dependence of Interfacial Energies in Magnesia"; Carnegie Mellon University,  
42 Pittsburgh, PA, 2001.
- 43 G.S. Rohrer, "Grain boundary energy anisotropy: a review," *J. Mater. Sci.*, **46** [18] 5881–5895 (2011).
- 44 D.M. Saylor, B.S. El Dasher, A.D. Rollett, and G.S. Rohrer, "Distribution of grain boundaries in aluminum  
45 as a function of five macroscopic parameters," *Acta Mater.*, **52** [12] 3649–3655 (2004).
- 46 J. Li, S.J. Dillon, and G.S. Rohrer, "Relative Grain Boundary Area and Energy Distributions in Nickel,"  
47 *Acta Mater.*, **57** 4304–4311 (2009).
- 48 C. Herring, *The Physics of Powder Metallurgy*. Mc Graw Hill, New York, 1951.
- 49 D.M. Saylor and G.S. Rohrer, "Measuring the influence of grain-boundary misorientation on thermal groove  
50 geometry in ceramic polycrystals," *J. Am. Ceram. Soc.*, **82** [6] 1529–1536 (1999).
- 51 W.W. Mullins, "Theory of Thermal Grooving," *J. Appl. Phys.*, **28** [3] 333–339 (1957).
- 52 P. Wynblatt and D. Chatain, "Anisotropy of segregation at grain boundaries and surfaces," *Metall. Mater.  
53 Trans. A*, **37** [9] 2595–2620 (2006).
- 54 D. McLean, *Grain boundaries in metals*. Clarendon Press, 1957.
- 55 A. Rollett, *Personal Correspondance*, (2012).
- 56 D.M. Saylor and G.S. Rohrer, "Determining Crystal Habits from Observations of Planar Sections," *J. Am.  
57 Ceram. Soc.*, **85** [11] 2799–2804 (2002).
- 58 G.S. Rohrer, D.M. Saylor, B. El Dasher, B.L. Adams, A.D. Rollett, and P. Wynblatt, "The distribution of  
59 internal interfaces in polycrystals," *Zeitschrift Fur Met.*, **95** [4] 197–214 (2004).
- 60 B. Lin, *Data for GBCD plot*, (2013).
- 61 Y.-N. Xu, Z.-G. Gu, and W.Y. Ching, "Electronic, structural, and optical properties of crystalline yttria,"  
62 *Phys. Rev. B*, **56** 14993–15000 (1997).
- 63 L.B. Borovkova, E.S. Lukin, and D.N. Poluboyarinov, "Sintering and recrystallization of yttrium oxide,"  
64 *Refract. Ind. Ceram.*, **13** [9] 595–600 (1972).
- 65 S. Ma and M.P. Harmer, "Near-Intrinsic Grain-Boundary Mobility in Dense Yttria," *J. Am. Ceram. Soc.*, **94**  
66 [3] 651–655 (2011).
- 67 Y. Tsukuda, "Densification, Thermal-diffusion, and Na Vapor Resistance of Y<sub>2</sub>O<sub>3</sub> Ceramics," *Am. Ceram.  
68 Soc. Bull.*, **62** [4] 510–512 (1983).
- 69 N. Saito, M.-I. Matsuda, and T. Ikegami, "Fabrication of Transparent Yttria Ceramics at Low Temperature  
70 Using Carbonate-Derived Powder," *J. Am. Ceram. Soc.*, **81** [8] 2021–2028 (1988).
- 71 C. Greskovich and J.P. Chernoch, "Improved polycrystalline ceramic lasers," *J. Appl. Phys.*, **45** (1974).
- 72 P. Hogan, T. Stefanik, C. Willingham, and R. Gentilman, *Transparent Yttria for IR Windows And Domes—  
73 Past and Present, 10th DoD Electromagn. Wind. Symp.*, (2004).
- 74 D.H. Riu, S.W. Lee, Y.K. Jeong, and S.C. Choi, "Microstructural Control of Y<sub>2</sub>O<sub>3</sub> coating on Quartz Glass  
75 for the Reduced Thermal Mismatch Stress," *Key Eng. Mater.*, **264-268** 601–604 (2004).
- 76 J. Iwasawa, R. Nishimizu, M. Tokita, and M. Kiyohara, "Plasma-Resistant Dense Yttrium Oxide Film  
77 Prepared by Aersol Deposition Process," *J. Am. Ceram. Soc.*, **90** [8] 2327–2332 (2007).

- 54 M. Aheem, S.-H. Lee, T. Mercer, and V. Vorsa, Plasma Etch Resistant, Highly Oriented Yttria Films, Coated Substrates and Related Methods; 2012.
- 55 E.R. Dobrovinskaya, L.A. Lytvynov, and V. Pishchik, *Sapphire: Material, Manufacturing, Applications*. Springer Science+Business Media, LLC, New York, NY, 2009.
- 56 G.S. Rohrer, *Structure and Bonding in Crystalline Materials*. Cambridge University Press, Cambridge, UK, 2001.
- 57 C.N.T. U.F. Kocks H.-R. Wenk, *Texture and Anisotropy: Preferred orientations in Polycrystals and their Effect on Materials Properties*. Cambridge University Press, Cambridge, UK, 1998.
- 58 S. Lartigue-Korinek, C. Carry, and L. Priester, "Multiscale aspects of the influence of yttrium on microstructure, sintering and creep of alumina," *J. Eur. Ceram. Soc.*, **22** [9–10] 1525–1541 (2002).
- 59 I. MacLaren, R.M. Cannon, M.A. Gülgün, R. Voytovych, N. Popescu-Pogrión, C. Scheu, U. Täßner, and M. Rühle, "Abnormal Grain Growth in Alumina: Synergistic Effects of Yttria and Silica," *J. Am. Ceram. Soc.*, **86** [4] 650–659 (2003).
- 60 V. Randel, *Microtexture Determination and its applications*, 2nd ed. Maney Publishing, London, 2003.
- 61 NT-MDT, *AFM NT-MDT*, **7/24/2011** (1997).
- 62 M. Stuer, Z. Zhao, U. Aschauer, and P. Bowen, "Transparent polycrystalline alumina using spark plasma sintering: Effect of Mg, Y and La doping," *J. Eur. Ceram. Soc.*, **30** [6] 1335–1343 (2010).
- 63 M. Suárez, A. Fernández, J.L. Menéndez, R. Torrecillas, H.U. Kessel, J. Hennicke, R. Kirchner, and T. Kessel, *Sintering Applications*. CC BY 3.0, 2013.
- 64 U. Anselmi-Tamburinia, S. Gennarib, J.E. Garaya, and Z.A. Munir, "Fundamental investigations on the spark plasma sintering/synthesis process II. Modeling of current and temperature distributions," *Mater. Sci. Eng. A*, **394** 139–148 (2005).
- 65 Z.A. Munir, U. Anselmi-Tamburini, and M. Ohyanagi, "The effect of electric field and pressure on the synthesis and consolidation of materials: A review of the spark plasma sintering method," *J. Mater. Sci.*, **41** 763–777 (2006).
- 66 O. Source, *Gwyddion*, **2011** (2011).
- 67 G.S. Rohrer, *Index of /~gr20/stereology*, **2011** (2013).
- 68 S.J. Dillon and G.S. Rohrer, "Characterization of the Grain-Boundary Character and Energy Distributions of Yttria Using Automated Serial Sectioning and EBSD in the FIB," *J. Am. Ceram. Soc.*, **92** [7] 1580–1585 (2009).
- 69 F. Papillon, G.S. Rohrer, and P. Wynblatt, "Effect of Segregating Impurities on the Grain-Boundary Character Distribution of Magnesium Oxide," *J. Am. Ceram. Soc.*, **92** [12] 3044–3051 (2009).
- 70 G.S. Rohrer, J. Li, S. Lee, A.D. Rollett, M. Groeber, and M.D. Uchic, "Deriving grain boundary character distributions and relative grain boundary energies from three-dimensional EBSD data," *Mater. Sci. Technol.*, **26** [6] 661–669 (2010).
- 71 B.L. Adams, S. Ta'Asan, D. Kinderlehrer, I. Livshits, D.E. Mason, C.-T. Wu, W.W. Mullins, G.S. Rohrer, *et al.*, "Extracting Grain Boundary and Surface Energy from Measurement of Triple Junction Geometry," *Interface Sci.*, **7** [3-4] 321–337 (1999).
- 72 S.A. Bojarski, M. Stuer, Z. Zhao, P. Bowen, and G.S. Rohrer, "Influence of Y and La Additions on Grain Growth and the Grain Boundary Character Distribution of Alumina," *J. Am. Ceram. Soc.*, (n.d.).
- 73 K. Matsunaga, H. Nishimura, H. Muto, T. Yamamoto, and Y. Ikuhara, "Direct measurements of grain boundary sliding in yttrium-doped alumina bicrystals," *Appl. Phys. Lett.*, **82** [8] 1179–1181 (2003).
- 74 A.M. Thompson, K.K. Soni, H.M. Chan, M.P. Harmer, D.B. Williams, J.M. Chabala, and R. Levi-Setti, "Dopant Distributions in Rare-Earth-Doped Alumina," *J. Am. Ceram. Soc.*, **80** [2] 373–376 (1997).
- 75 J. Chen, Y.-N. Xu, P. Rulis, L. Ouyang, and W.-Y. Ching, "Ab initio theoretical tensile test on Y-doped  $\Sigma=3$  grain boundary in  $\alpha$ -Al<sub>2</sub>O<sub>3</sub>," *Acta Mater.*, **53** [2] 403–410 (2005).
- 76 J. Chen, L. Ouyang, and W.Y. Ching, "Molecular dynamics simulation of Y-doped  $\Sigma 37$  grain boundary in alumina," *Acta Mater.*, **53** [15] 4111–4120 (2005).
- 77 R. Voytovych, M.A. Gulgun, R.M. Cannon, and M.A. Rühle, "The effect of yttrium on densification and grain growth in  $\alpha$ -alumina," *Acta Mater.*, **50** 3453–3463 (2002).
- 78 T. Gemming, S. Nufer, W. Kurtz, and M. Ru, "Grain Boundaries in  $\alpha$ -Al<sub>2</sub>O<sub>3</sub>: II, Bicrystals with Y at the Interface," **94** 590–594 (2003).
- 79 M.A. Gülgün, R. Voytovych, I. MacLaren, M. Rühle, and R.M. Cannon, "Cation Segregation in an Oxide Ceramic with Low Solubility: Yttrium Doped  $\alpha$ -Alumina," *Interface Sci.*, **10** 99–110 (2002).

- 80 S. Šturm, M. a. Gülgün, G. Richter, F.M. Morales, R.M. Cannon, and M. Rühle, “The role of Si impurities  
in the transient dopant segregation and precipitation in yttrium-doped alumina,” *Int. J. Mater. Res. (formerly*  
81 *Zeitschrift fuer Met.*, **101** [1] 95–101 (2010).
- 82 J. Cho, C.M. Wang, H.M. Chan, J.M. Rickman, and M.P. Harmer, “A study of grain-boundary structure in  
rare-earth doped aluminas using an EBSD technique,” *J. Mater. Sci.*, **37** [1] 59–64 (2002).
- 83 J. Fang, M.A. Thompson, M.P. Harmer, and H.M. Chan, “Effect of Yttrium and Lanthanum on the Final-  
Stage Sintering Behavior of Ultrahigh-Purity Alumina,” **12** [1997] 2005–2012 (2005).
- 84 M. Kitayama and A.M. Glaeser, “The Wulff Shape of Alumina: III, Undoped Alumina,” *J. Am. Ceram.*  
*Soc.*, **85** [3] 611–622 (2004).
- 85 J.-H. Choi, D.-Y. Kim, B.J. Hockey, S.M. Wiederhorn, C.A. Handwerker, J.E. Blendell, W.C. Carter, and  
A.R. Roosen, “Equilibrium Shape of Internal Cavities in Sapphire,” *J. Am. Ceram. Soc.*, **80** [1] 62–68  
(1997).
- 86 J. W. Cahn and C. A. Handwerker, “Equilibrium geometries of anisotropic surfaces and interfaces,” *Mater.*  
*Sci. Eng. A*, **162** [1-2] 83–95 (1993).
- 87 J. Cho, H.M. Chan, M.P. Harmer, and J.M. Rickman, “Influence of Yttrium Doping on Grain Misorientation  
in Aluminum Oxide,” *J. Am. Ceram. Soc.*, **81** [11] 3001–3004 (1998).
- 88 M. Stuer, P. Bowen, M. Cantoni, C. Pecharroman, and Z. Zhao, “Nanopore Characterization and Optical  
Modeling of Transparent Polycrystalline Alumina,” *Adv. Funct. Mater.*, **22** [11] 2303–2309 (2012).
- 89 EDAX-TSL, *EDAX-TSL OIM 6.1 EBSD*, (2011).
- 90 P. Vonlanthen and B. Grobety, “CSL grain boundary distribution in alumina and zirconia ceramics,” *Ceram.*  
*Int.*, **34** [6] 1459–1472 (2008).
- 91 J. Gruber, D.C. George, A.P. Kuprat, G.S. Rohrer, and A.D. Rollett, “Effect of anisotropic grain boundary  
properties on grain boundary plane distributions during grain growth,” *Scr. Mater.*, **53** [3] 351–355 (2005).
- 92 H.M. Miller and G.S. Rohrer, “Evolution of the Grain Boundary Character Distribution in Strontium  
Titanate during Grain Growth”; pp. 335–342 in *Appl. Texture Anal.* John Wiley & Sons, Inc., 2008.
- 93 J. Castaing, J. Cadoz, and S.H. Kirby, “Deformation of Al<sub>2</sub>O<sub>3</sub> Dingle Crystals between 25°C and 1800°C :  
Basal and Prismatic Slip,” *Le J. Phys. Colloq.*, **42** [C3] C3–43–C3–47 (1981).
- 94 S. Galmarini, U. Aschauer, P. Bowen, and S.C. Parker, “Atomistic Simulation of Y-Doped  $\alpha$ -Alumina  
Interfaces,” *J. Am. Ceram. Soc.*, **91** [11] 3643–3651 (2008).
- 95 H. Grimmer, R. Bonnet, S. Lartigue, and L. Priester, “Theoretical and Experimental Descriptions of Grain  
Boundaries in Rhombohedral Alpha-Al<sub>2</sub>O<sub>3</sub>,” *Philos. Mag. a-Physics Condens. Matter Struct. Defects Mech.*  
*Prop.*, **61** [3] 493–509 (1990).
- 96 H. Grimmer, “Coincidence Orientations of Grains in Rhombohedral Materials,” *Acta Crystallogr. Sect. A*,  
**45** 505–523 (1989).
- 97 H. Nishimura, K. Matsunaga, T. Saito, T. Yamamoto, and Y. Ikuhara, “Atomic Structures and Energies of  
 $\Sigma 7$  Symmetrical Tilt Grain Boundaries in Alumina Bicrystals,” *J. Am. Ceram. Soc.*, **86** [4] 574–580 (2003).
- 98 J.F. Shackelford and W.D. Scott, “Relative Energies of (1100) Tilt Boundaries in Aluminum Oxide,” *J. Am.*  
*Ceram. Soc.*, **51** [12] 688–& (1968).
- 99 T. Hoche, P.R. Kenway, Hans-JoachimKleebe, and M. Rühle, “High-Resolution Transmission Electron  
Microscopy Studies of a near  $\Sigma 11$  Grain Boundary in  $\alpha$ -alumina,” *J. Am. Ceram. Soc.*, **77** [2] 339–348  
(1994).
- 100 P.R. Kenway, “Calculated Structures and Energies of Grain Boundaries in  $\alpha$ -Al<sub>2</sub>O<sub>3</sub>,” *J. Am. Ceram. Soc.*,  
**77** [2] 349–355 (1994).
- 101 I. Milas, B. Hinnemann, and E.A. Carter, “Structure of and ion segregation to an alumina grain boundary:  
Implications for growth and creep,” *J. Mater. Res.*, **23** [5] 1494–1508 (2008).
- 102 D.M. Saylor, A. Morawiec, and G.S. Rohrer, “Distribution of grain boundaries in magnesia as a function of  
five macroscopic parameters,” *Acta Mater.*, **51** [13] 3663–3674 (2003).
- 103 D.M. Saylor, A. Morawiec, and G.S. Rohrer, “The relative free energies of grain boundaries in magnesia as  
a function of five macroscopic parameters,” *Acta Mater.*, **51** [13] 3675–3686 (2003).
- 104 A. Putnis, *Introduction to Mineral Sciences*. Cambridge University Press, Cambridge, United Kingdom,  
1992.
- 105 M.N. Rahaman, *Ceramic Processing and Sintering*. CRC Press, 2003.
- R. Raj, M. Cologna, and J.S.C. Francis, “Influence of Externally Imposed and Internally Generated  
Electrical Fields on Grain Growth, Diffusional Creep, Sintering and Related Phenomena in Ceramics,” *J.*  
*Am. Ceram. Soc.*, **94** [7] 1941–1965 (2011).

- 106 L.E. Murr, *Interfacial phenomena in metals and alloys*. Addison-Wesley Pub. Co., Advanced Book  
Program, 1975.
- 107 D. Prokoshkina, V.A. Esin, G. Wilde, and S.V. Divinski, "Grain boundary width, energy and self-diffusion  
in nickel: Effect of material purity," *Acta Mater.*, **61** [14] 5188–5197 (2013).
- 108 R. Sumi, N. Toda, H. Fujii, and S. Tsurekawa, "IMPACT OF A MAGNETIC FIELD ON GRAIN  
BOUNDARY ENERGY IN 99.9% IRON AND IRON-TIN ALLOY," *Rev. Adv. Mater. Sci.*, **21** 35–43  
(2009).
- 109 D. Gupta, "Diffusion, Solute Segregations and Interfacial Energies in Some Material: An Overview,"  
*Interface Sci.*, **11** [1] 7–20 (2003).
- 110 J.W. Gibbs, *The collected works of J. Willard Gibbs, Volume 2*. Longmans, Green and Co., 1902.
- 111 E.D. Hondros, M.P. Seah, S. Hoffmann, and P. Lecek, *Physical Metallurgy, Volume 1*. North-Holland Phys.  
Pub., 1996.
- 112 J. Schölhammer, B. Baretzky, W. Gust, E. Mittemeijer, and B. Straumal, "Grain Boundary Grooving as an  
Indicator of Grain Boundary Phase Transformations," *Interface Sci.*, **9** [1-2] 43–53 (2001).
- 113 S. Fabris and C. Elsässer, "First-principles analysis of cation segregation at grain boundaries in  $\alpha$ -Al<sub>2</sub>O<sub>3</sub>,"  
*Acta Mater.*, **51** [1] 71–86 (2003).
- 114 M. Exner and M.W. Finnis, "Atomistic Simulation of Grain Boundaries in Alumina," *Mater. Sci. Forum*,  
**207-209** 225–228 (1996).
- 115 M.A. Gülgün, S. Šturm, R.M. Cannon, and M. Rühle, "Transient dopant segregation and precipitation in  
yttrium-doped alumina," *Int. J. Mater. Res.*, **99** [12] 1324–1329 (2008).
- 116 C.A. Handwerker, J.M. Dynys, R.M. Cannon, and R.L. Coble, "Dihedral Angles in Magnesia and Alumina -  
Distributions from Surface Thermal Grooves," *J. Am. Ceram. Soc.*, **73** [5] 1371–1377 (1990).
- 117 J. Luo, Y.-M. Chiang, and R.M. Cannon, "Nanometer-thick surficial films in oxides as a case of  
prewetting," *Langmuir*, **21** [16] 7358–65 (2005).
- 118 O. Fabrichnaya, H.J. Seifert, T. Ludwig, F. Aldinger, and A. Navrotsky, "The assessment of thermodynamic  
parameters in the Al<sub>2</sub>O<sub>3</sub>-Y<sub>2</sub>O<sub>3</sub> system and phase relations in the Y-Al-O system," *Scand. J. Metall.*, **30** [3]  
175–183 (2001).